Design and Performance Improvement of AC Machines Sharing a Common Stator

by

Lusu Guo

A Dissertation Submitted to the Graduate

Faculty of Rensselaer Polytechnic Institute

in Partial Fulfillment of the

Requirements for the Degree of

DOCTOR OF PHILOSOPHY

Major Subject: Electrical Engineering

Approved by the
Examining Committee:

____

Leila Parsa
Dissertation Adviser

____

Joe H. Chow, Member

____

Sheppard J. Salon, Member

____

B. Wayne Bequette, Member

Rensselaer Polytechnic Institute
Troy, New York

April 2016
(For Graduation May 2016)

CONTENTS

LIST OF TABLES

LIST OF FIGURES

ACKNOWLEDGMENT

I would like to express my deepest and sincerest gratitude to all the people who gave me a lot of help during my PhD study.

First of all, I would like to deeply and mostly thank my thesis advisor, Professor Leila Parsa for her expert guidance, support, encouragement and inspiration she has given to me throughout the courses of my Ph. D. research. During my study in Rensselaer Polytechnic Institute, Professor Leila Parsa has been always supportive and helpful to me. There is no doubt that her professional knowledge and enthusiasm accelerated my research work from incomplete to success. She has been an excellent stimulator and motivator not only in study and research but in my life. I have been fortunate to have Dr. Leila Parsa as my advisor and I consider it a great honor working with her.

I also would like to extend my thanks to my committee members, Prof. Joe H. Chow, Prof. Sheppard J. Salon and Prof. B. Wayne Bequette for their invaluable suggestions and comments, which made my dissertation a better work.

I want to say thanks to my fellow graduate students, Suman Dwari, Rohan Dayal, Arun Gandhi, Siavash Sadeghi, Ali Mohammadpour and Kumar Modepalli for their enlightening discussions and suggestions throughout the course of this work. The friendship and the overall pleasant atmosphere have made my stay at Rensselaer Polytechnic Institute enjoyable.

My dearest gratitude goes to Feina Cao, my beloved wife for her love, patience, loyalty, sacrifices and comforting accompany during the whole research life.

Finally, I would like to dedicate this dissertation to my parents, Keping Wang and Wenyi Guo, whose unconditional love guided me at every step of my life.

ABSTRACT

With the increasing demand on electric motors in various industrial applications, especially electric powered vehicles (electric cars, more electric aircrafts and future electric ships and submarines), both synchronous reluctance machines (SynRMs) and interior permanent magnet (IPM) machines are recognized as good candidates for high performance variable speed applications. Developing a single stator design which can be used for both SynRM and IPM motors is a good way to reduce manufacturing and maintenance cost. SynRM can be used as a low cost solution for many electric driving applications and IPM machines can be used in power density crucial circumstances or work as generators to meet the increasing demand for electrical power on board. In this research, SynRM and IPM machines are designed sharing a common stator structure. The prototype motors are designed with the aid of finite element analysis (FEA). Machine performances with different stator slot and rotor pole numbers are compared by FEA. An 18-slot, 4-pole structure is selected based on the comparison for this prototype design.

Sometimes, torque pulsation is the major drawback of permanent magnet synchronous machines. There are several sources of torque pulsations, such as back-EMF distortion, inductance variation and cogging torque due to presence of permanent magnets. To reduce torque pulsations in permanent magnet machines, all the efforts can be classified into two categories: one is from the design stage, the structure of permanent magnet machines can be optimized with the aid of finite element analysis. The other category of reducing torque pulsation is after the permanent magnet machine has been manufactured or the machine structure cannot be changed because of other reasons. The currents fed into the permanent magnet machine can be controlled to follow a certain profile which will make the machine generate a smoother torque waveform. Torque pulsation reduction methods in both categories will be discussed in this dissertation. In the design stage, an optimization method based on orthogonal experimental design will be introduced. Besides, a universal current profiling technique is proposed to minimize the torque pulsation along with the stator copper losses in modular interior permanent magnet motors. Instead of sinusoidal current waveforms, this algorithm will calculate the

proper currents which can minimize the torque pulsation. Finite element analysis and Matlab programing will be used to develop this optimal current profiling algorithm.

Permanent magnet machines are becoming more attractive in some modern traction applications, such as traction motors and generators for an electrified vehicle. The operating speed or the load condition in these applications may be changing all the time. Compared to electric machines used to operate at a constant speed and constant load, better control performance is required. In this dissertation, a novel model reference adaptive control (MRAC) used on five-phase interior permanent magnet motor drives is presented. The primary controller is designed based on artificial neural network (ANN) to simulate the nonlinear characteristics of the system without knowledge of accurate motor model or parameters. The proposed motor drive decouples the torque and flux components of five-phase IPM motors by applying a multiple reference frame transformation. Therefore, the motor can be easily driven below the rated speed with the maximum torque per ampere (MTPA) operation or above the rated speed with the flux weakening operation. The ANN based primary controller consists of a radial basis function (RBF) network which is trained on-line to adapt system uncertainties. The complete IPM motor drive is simulated in Matlab/Simulink environment and implemented experimentally utilizing dSPACE DS1104 DSP board on a five-phase prototype IPM motor. The proposed model reference adaptive control method has been applied on the commons stator SynRM and IPM machine as well.

1. INTRODUCTION

An electric machine uses electrical energy to produce mechanical energy through the interaction between magnetic fields and current carrying conductors, or in the reverse way, uses mechanical energy to produce electrical energy. Almost all electricity consumed today is generated by electrical machines. There are very few electricity generating processes where electric machines are not playing a role, and they are limited to small-scale house appliance electricity generating devices, such as batteries and fuel cells. On the other side, electric machines also play a considerable role in converting electrical energy into mechanical energy. According to U.S. Department of Energy, more than 62% of the electrical energy produced in the U.S. is consumed by electric motors [1]. Rotating electric motors are probably the most reliable and accurate means for controlling a wide variety of industrial processes. The overall energy conversion efficiencies of electric motors are high and with the fast development of power electronics devices and control techniques, the speed and torque of electric motors can be controlled accurately, which will bring electric motors into extended industrial processes.

With the increasing demand of energy globally, a significant amount of greenhouse gases has been emitted into the atmosphere by burning fossil fuels (coal, oil, natural gas, etc). Automobiles became the largest source of greenhouse gases in the U.S. for the first time in 2012, taking place of coal-burning power plants according to the U.S. Environmental Protection Agency [2], [3]. Automobile and coal-burning power plants together are responsible for more than half of the U.S. greenhouse emissions. One possible solution for this climate crisis is introducing cleaner sources for electrical energy generation, such as nuclear power plants. Furthermore, renewable energy sources such as wind, solar, etc. are becoming important alternatives to fossil fuels in generating electric power. On the other hand, electricity is replacing the position or reducing the consumption of fossil fuel in many means of transportation, such as more electric aircrafts (MEA), energy-efficient all electric ships (EE-AES), hybrid electric vehicles (HEV) and plug-in hybrid vehicles (PHEV). Development of next generation more electricity powered transportation depends on the research of modern electric machines. As a result, an explosive demand of all types of electric machines especially for traction applications is expected in the near future. The significance of designing new and high performance electric machines and their drives becomes more and more emphasized.

1.1 Permanent magnet synchronous machine

1.1.1 Development of permanent magnet machine

Permanent magnet machines use permanent magnet materials to generate the necessary air-gap magnetic field, which is important in energy conversion. Although not practical, the first electric machine ever built was a permanent magnet machine. Built by the British scientist Michael Faraday in 1821, it was the first device demonstrating the conversion of electrical energy into mechanical energy by electromagnetic means. Initially, the applications of permanent magnet were limited because the permanent magnet materials such as steel magnets have very low energy densities. The first practical permanent magnet machine was not produced until Alnico magnets were developed by Bell Laboratories in 1930's. The flux density became comparable to current carrying conductors and practical electrical motors built with permanent magnets rating up to several horsepower became commercially available [4].

Although the flux density of Alnico class permanent magnets is high, the use of Alnico permanent magnet machine was limited mainly because of its low coercive force. The permanent magnet material is very easy to be demagnetized by motor stator currents. Both Alnico class and Ferrite permanent magnets have limitations and were prevented from wide industrial use. The revolutionary development of permanent magnet materials was the found of rare-earth magnets in the 1960's. Among the present permanent magnets, this class has the best magnetic performance and is very suitable for electric machine applications. In the early days, the most common commercial rare-earth permanent magnet was Samarium-Cobalt, which has high flux density, high coercive force and high temperature stability. The primary limitation of Samarium-Cobalt magnets was the high price, as Cobalt is a strategic material, and the relative reserve of Samarium in the earth is very limited. Electric machines made from this class of PMs were only used in aerospace and other applications where cost was not an essential factor.

In 1980's, Neodymium-Iron-Boron (NdFeB) based rare-earth permanent magnet was found. This class permanent magnet shares high magnetic performance with the very expensive Samarium-Cobalt magnets but the price is much lower. There were no expensive elements used. During 1990's, with the development of NdFeB permanent magnet manufacturing techniques, the technical characteristics kept improving. Better temperature and corrosion stability allowed widespread use of NdFeB magnets in all kinds of electric machine production and provided higher power density than normal electrical machines excited by current carrying conductors. The research and development on modern permanent magnet materials is not slowing down but attracting more interests.

1.1.2 Structure of permanent magnet synchronous machine

Permanent magnet synchronous machines are normally composed of rotor, stator, machine frame and necessary accessories. The most common structure of permanent magnet machines is the conventional outer stator inner rotor configuration. The magnetic flux is going from the rotor across the air-gap radially into the stator core. As a result, they are also called radial-flux permanent magnet synchronous machines. The stator is the same as that in an induction motor. Laminations made of soft magnetic material are stacked together to reduce eddy losses. Figure 1.1 shows four most common rotor structures for radial-flux permanent magnet machines [5].

(a) **Surface mounted PMs** As the magnetic relative permeability of rare-earth magnet materials is close to unity, there is no magnetic saliency in the rotor. The d axis inductance is almost the same as q axis inductance. The main advantage of this type of PM machine is its simple structure and it is widely used for permanent magnet machine design [6]-[12]. The manufacturing cost is relatively low because the magnets can easily be attached in the rotor core. Furthermore, it is easy to design the rotor to produce sinusoidal magnetic flux distributions in the stator windings. However, the major drawback of surface mounted PM machines is because of the magnet attachment. During operation, especially at high speed, the centrifugal forces may cause the magnets to detach from the rotor, preventing the use of such configuration in high speed applications.

(b) **Inset PMs** As there are high magnetic permeability materials between two permanent magnets, the rotor has a salient structure. Reluctance torque resulting from unequal d axis and q axis inductances may present besides the magnetic torque. The power density and dynamic performance may be improved compared to surface mounted PM motors.

(c) **Interior PMs** Interior permanent magnet machines usually have high rotor saliency, which means significant reluctance torque may be present in the total torque produced [13]-[19]. The reluctance torque and the rigid rotor structure are helpful in extending the flux weakening capability when the machine is driven to high speed [20]-[23]. The manufacturing cost is usually higher than the previous rotor structures.

(d) **Tangentially magnetized PMs** The main advantage of this type permanent magnet machine is that the magnetic flux in each pole is provided by two adjacent magnets [24]-[28]. The magnetic flux per pole will be higher than the first three rotor structures, which is helpful especially when there are more than 4 poles in the rotor.

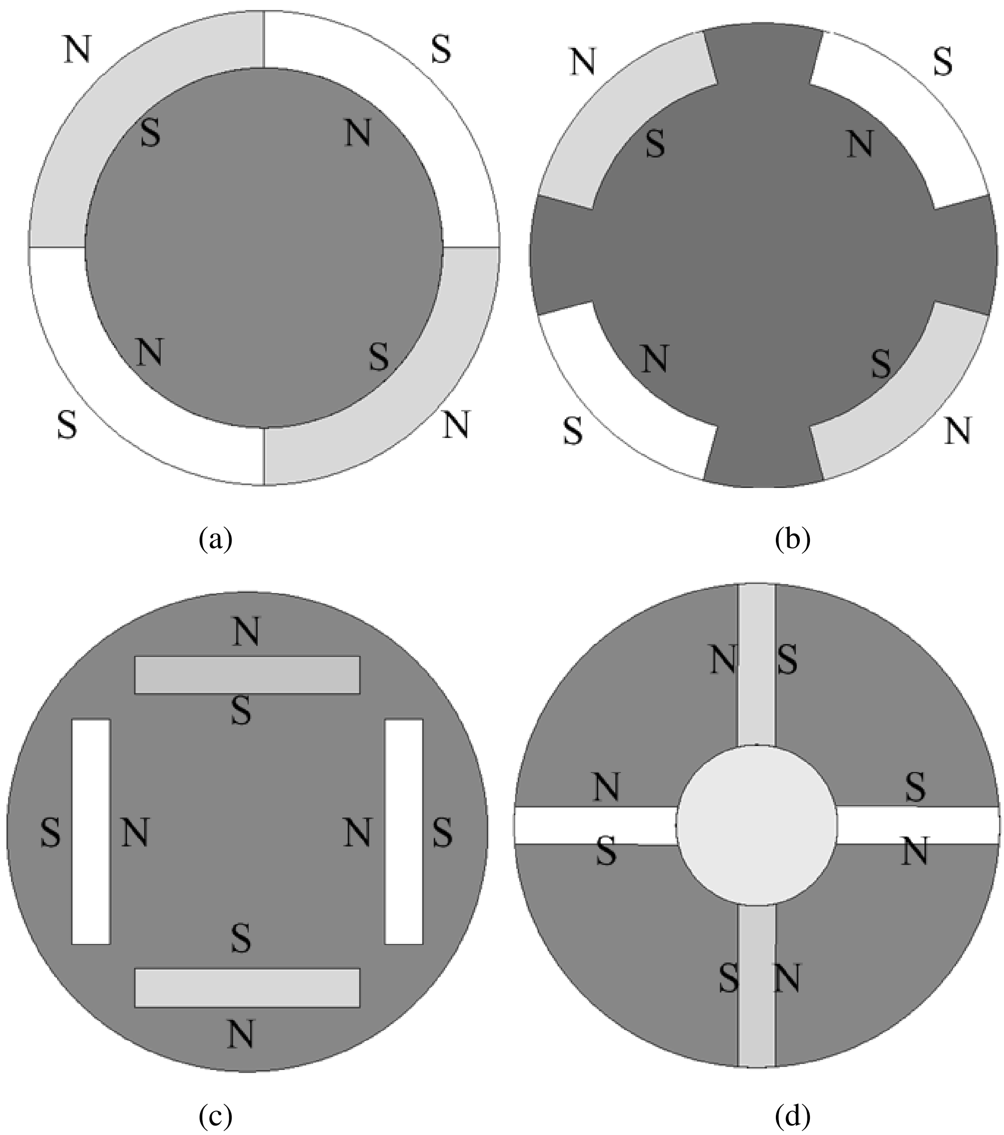

Figure 1.1: Rotor structure of radial flux permanent magnet machines. (a) Surface mounted PMs. (b) Inset PMs. (c) Interior PMs. (d) Tangentially magnetized PMs.

Besides the normal inner rotor radial-flux permanent magnet synchronous machine, there are other designs available with different structure and specifications.

(1) Axial-flux permanent magnet machine

This machine features a relatively larger diameter and much shorter axial length compared to normal inner rotor radial-flux permanent magnet machines. The magnetic flux is going through the air-gap following the axial direction and turns back through the stator core [29]-[32]. Figure 1.2 shows the structure of an axial-flux permanent magnet machine. One of the motivations of designing axial-flux permanent magnet machines is providing a high power density solution for several special applications with limited space for motor installation, such as electric vehicle on-wheel motors [33]-[37].

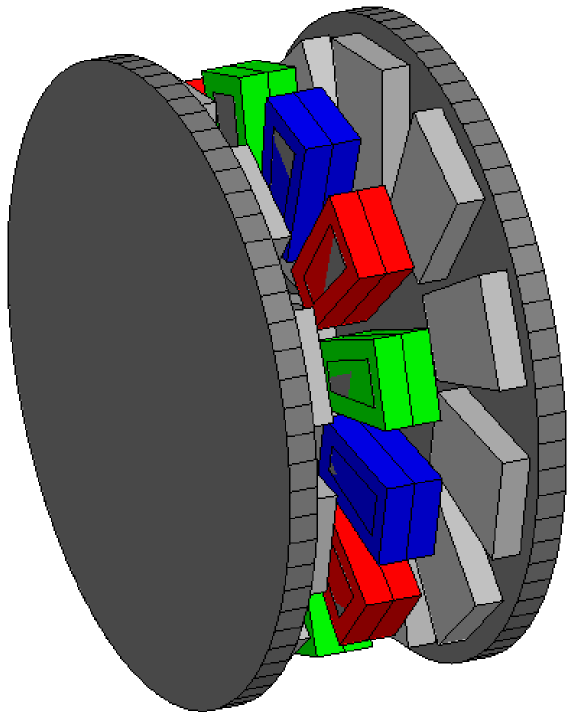

Figure 1.2: 3D view of an axial-flux permanent magnet machine.

(2) Modular permanent magnet machine

The modular permanent magnet machine is designed by segmenting the stator into several identical modules. Figure 1.3 shows the cross section structure of a modular permanent magnet machine. The rotor has an interior PM configuration. The motor consists of six identical stator modules with two modules for each phase. The modular PM machines feature high robustness and inherent fault tolerant capability. These characteristics are essentially required in some safety critical applications.

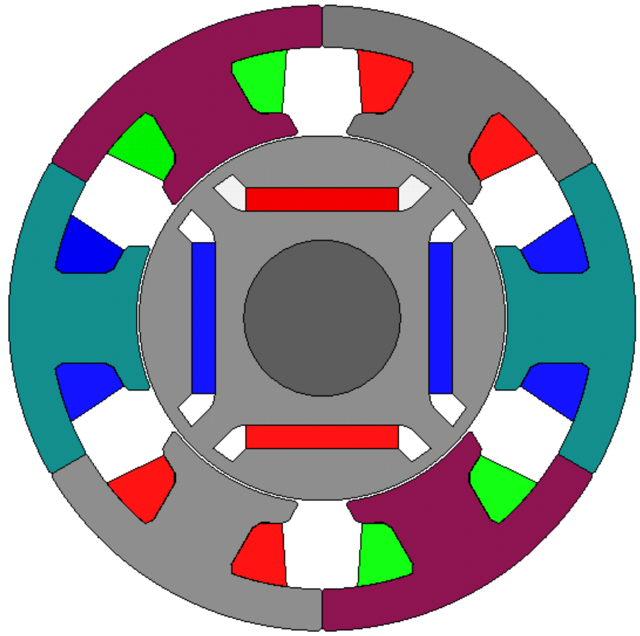

Figure 1.3: Cross section of a modular interior permanent magnet machine.

(3) Line-start permanent magnet machine

A line-start permanent magnet machine is designed with a squirrel cage in the rotor, as in induction motors. The squirrel cage is also used to start the permanent magnet machine without any inverter [38]-[41]. The line-start permanent magnet machine combines the advantages of both PM synchronous machine and induction machine. Without the inverter, the total cost is greatly reduced because inverters are the major cost of modern motor drive system. The performance of line-start permanent magnet machine is better than conventional induction machines thanks to the development of rare-earth permanent magnet materials. Figure 1.4 shows the rotor structure of line-start permanent magnet synchronous machine.

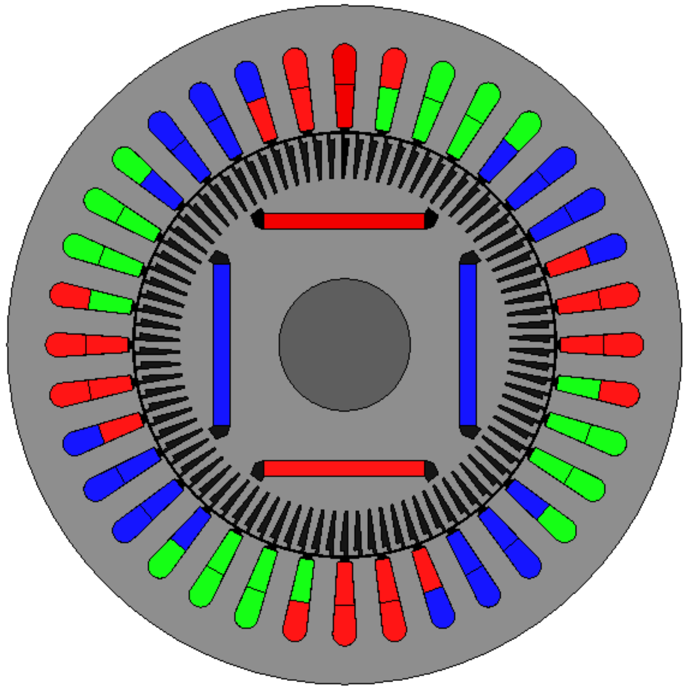

Figure 1.4: Cross section of line-start permanent magnet.

1.2 Synchronous reluctance machine

Synchronous reluctance machines (SynRM) can be considered as a simple type of brushless AC machines. They feature a standard three phase stator similar to that in a conventional induction motor with spatial sinusoidal wave rotating magnetic field. The rotor structure may vary a lot from single flux barrier transversely-laminated rotor [42], [43] to multiple flux barrier rotor [44]-[47] or axially-laminated rotor [48]-[50]. Unlike synchronous AC machines and induction machines, rotor of a synchronous reluctance machine is only composed of steel laminations without any exciting windings or permanent magnet materials. The rotor should present a variable magnetic reluctance along the air-gap. As a result, it will try to achieve the position with the minimum reluctance, following the principle of minimum potential energy. That is to say, when there are AC currents flowing in the stator windings, electromagnetic torque will be produced except when the rotor axis is aligned with the stator's electric axis. With the above mentioned characteristics, synchronous reluctance machine has a relatively simple, low-cost configuration.

Before the 1980's, research on SynRMs was primarily related to the line-start machine. Compared to an induction machine, the requirement of a line-start squirrel cage resulted in the relatively poor performance of synchronous reluctance machines. With the development of power electronics devices and control technology of AC machines, there has been a renewed interest in synchronous reluctance machines. Advances in modern current-controlled PWM inverters as well as modern control schemes play a key role in the design of new synchronous reluctance machines [51]-[55]. This makes SynRM's performance competitive to an induction machine. Due to its inherent simplicity and other merits, more and more SynRM could be found in the market.

Several typical designs of SynRM will be introduced in the following section.

(1) Single flux barrier rotor

The easiest way to make a rotor with magnetic saliency to produce reluctance torque is by punching a single flux barrier in each pole. Figure 1.5 shows an example of such SynRM. For a long time, it is effective to use a single flux barrier rotor and borrow a stator from conventional induction machine to design a SynRM. However, less attention is paid on this type of SynRM for the simple reason that it could hardly provide sufficient saliency ratio and may bring high electromagnetic torque pulsations.

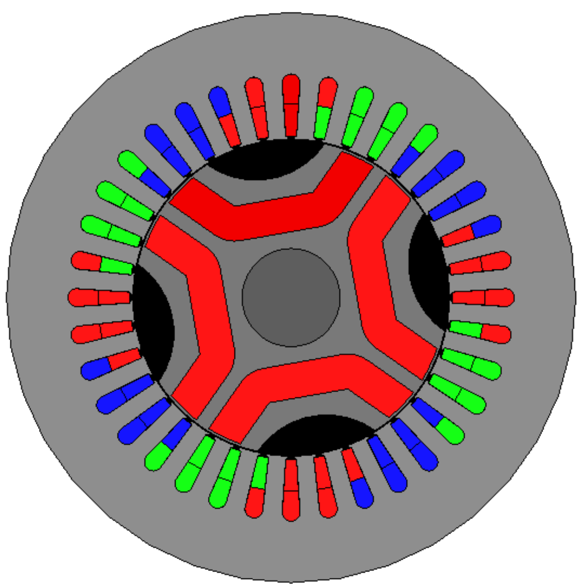

Figure 1.5: Cross section of SynRM with single flux barrier in the rotor.

(2) Multiple flux barrier rotor

Figure 1.6 shows an example of SynRM with multiple flux barriers in the rotor. Compared to simple single flux barrier rotor design, multiple flux barrier rotor structure is much more capable of generating higher saliency ratio, and the torque pulsation may be reduced by proper geometry optimization of the flux barriers. Small amount of permanent magnets can be easily inserted into one or several of the flux barriers to improve the performance. It is the mostly popular structure in SynRM design.

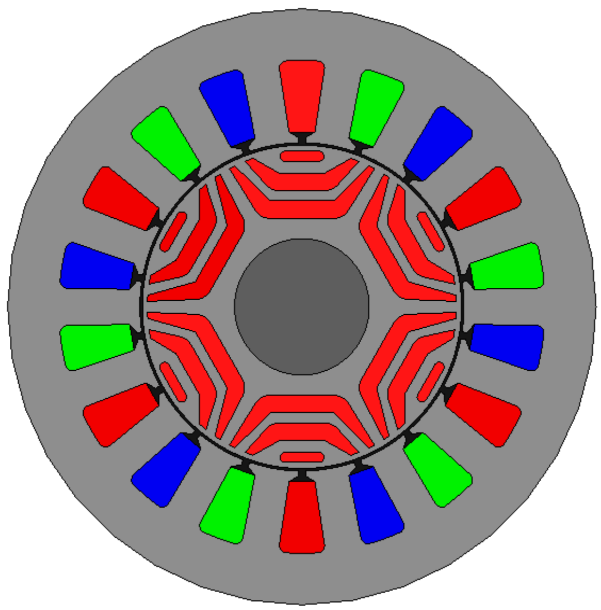

Figure 1.6: Cross section of SynRM with multiple flux barriers in the rotor.

(3) Axially-laminated rotor

Figure 1.7 shows the cross section structure of a SynRM with axially-laminated rotor. They normally feature high saliency ratio, which will produce competitive total torque over other kinds of rotors. But SynRM with axially-laminated rotor is more difficult to manufacture, compared with multiple flux barrier rotor, which can be manufactured by punched steel laminations. Another disadvantage of axially-laminated rotor which prevented it from wider industrial applications is that it is difficult to skew the rotor, which is a very effective way to reduce torque pulsations.

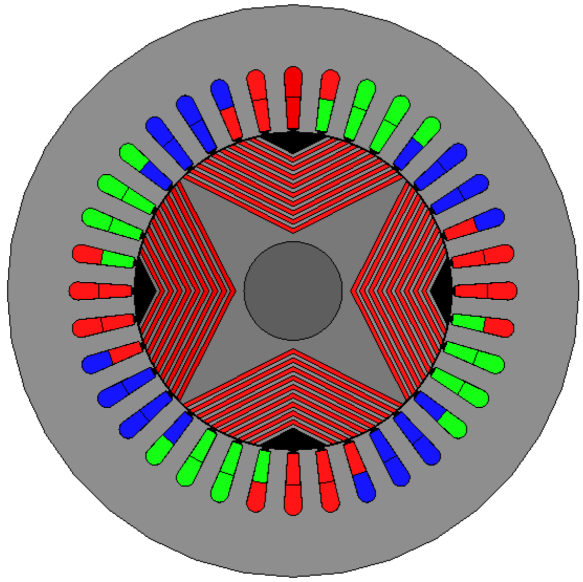

Figure 1.7: Cross section of SynRM with axially-laminated rotor.

1.3 High performance control of synchronous permanent magnet machines

1.3.1 Variable voltage variable frequency (VVVF) control

In the adjustable speed AC machines drives, the speed can be controlled by adjusting the frequency of electrical currents. At the same time, the voltage amplitude also needs to be adjusted as the frequency changes [56]. VVVF control is a low-cost solution for controlling the machine speed without any position or speed sensor. Below the base speed, the ratio between voltage and frequency is maintained a constant value if neglecting the resistive voltage drop. Above the base speed, as the terminal voltages cannot be further increased, the air gap flux will decrease as the speed goes up. VVVF AC machine control is an open loop control system. Compared to other high-performance motor drive systems, it can be realized easily with a very low cost. However, the dynamic performance is poor especially when the objective speed is low. The starting torque cannot be controlled to be a high value. It is usually used in some fan load applications.

1.3.2 Vector control

Vector control is also called field-oriented control, which adjusts the speed of AC machines by controlling the currents in the rotating reference frame. It is the most widely used closed-loop control of permanent magnet synchronous machines [57]-[61]. For a permanent magnet synchronous machine, the stator side quantities should be first transformed into a rotating reference frame which rotates at the same speed as the rotor. This transformation from a-b-c reference frame to *d-q* reference frame is called Park's transformation. The permanent magnet machine is a complicated nonlinear system, which has multiple variables highly coupled with each other. It is difficult to regulate either the torque or the flux directly by controlling the terminal voltages or currents in the stator reference frame. By transforming the stator side quantities into the rotating coordinates, the stator currents can be transformed into two decoupled vectors, one of which is only controlling the flux and the other one decides the electromagnetic torque produced. Therefore, the permanent magnet synchronous machine can be controlled like a DC machine. Fast and independent flux and torque control can be realized. After several years of development, many problems in vector control have been solved, making it the most common control method in high performance AC motor servo drive systems.

The basic idea behind vector control of permanent magnet synchronous machine is controlling the phase and amplitude of the stator currents, but it is realized in the rotating reference frame where the rotating space vector changes to static space vector. d and q axis components will be constant values if harmonics are not considered. With certain torque or flux equations, the corresponding motor quantities can be controlled in real time. Different vector control methods with different control objectives have been proposed by researchers, such as zero d-axis current control, maximum torque per ampere (MTPA) control, unity power factor control and etc.

1.3.3 Direct torque control

The direct torque control method was first introduced by C. French in 1995 [62]. After that, more research work has been done to develop this new control method for permanent magnet synchronous machines [63]-[67]. Direct torque control calculates the torque and magnetic flux from the measured three phase stator voltages and currents. It was first designed to drive three phase induction motors and then some theoretical analysis and experiments were carried out on permanent magnet synchronous machines. Although there are still some technical difficulties, current research works have shown that direct torque control is being improved and can be widely used.

The basic idea behind direct torque control of permanent magnet synchronous machine is controlling the stator magnetic flux and the electromagnetic torque simultaneously, usually with hysteresis controllers. The stator current and voltage are measured and used for estimating the stator magnetic flux. The electromagnetic torque is also estimated using the measured current and estimated flux. Both the magnetic flux and torque are compared with the reference values, the error signals are used to generate the switching states for the voltage source inverters. The advantages of direct torque control include fast dynamic torque and flux control because they are controlled directly by the controllers. In traditional vector control system, torque is adjusted by controlling the currents in *d-q* axes. Another major advantage of direct torque control is that it does not need *d-q* axes coordinate transformation. However, direct torque control has disadvantages of high torque and magnetic flux ripple because of the limited voltage vectors and variable switching frequency. The low speed performance of direct torque control is also poor because the effect of stator resistance on the control system is more significant at low speed.

1.3.4 Intelligent control

The electric machine is a complicated highly nonlinear system with many variables. Compared to DC motors, the control of three-phase AC machines is more complex and difficult to reach competitive dynamic performance. Even though the vector control allows us to control three phase AC machines like a DC motor, the nonlinearities are still in the system and may cause various problems, such as torque pulsations resulting from harmonics, mechanical vibrations caused by nonlinear power converters and etc. Furthermore, some of the machine parameters are dependent on the operation conditions, which also need to be compensated. In normal vector control, the speed or current loop uses PI or PID controllers, which are designed to control linear systems and can only work under a narrow range of operating conditions. More accurate system models or more advanced controllers are needed to improve the dynamic performance of the entire motor drive system. Intelligent control is said to be a solution for future motor control design with improved performance, which mainly includes fuzzy-logic and neural network based control [68]-[73].

1.4 Dissertation outline

In chapter 2 of this dissertation, an interior permanent magnet machine and a synchronous reluctance machine are designed sharing the same stator. Developing a single stator design which can be used for both SynRM and IPM machines is a good way to reduce the manufacturing and maintenance cost. IPM machines usually have better performance, and SynRMs are more robust as a result of the quite simple structure. The design procedure is provided in this chapter.

Both chapter 3 and chapter 4 of this dissertation discussed methods of reducing possible torque pulsations in IPM machines. Torque pulsation minimization methods can be simply classified into two categories: One is on the machine design stage, searching for the optimized machine structure which will bring less torque pulsation. The other one is after the machine has been manufactured or the structure cannot be changed due to some other concerns. The currents fed into the machine can be regulated to follow certain profiles which will make the machine generate a smoother torque waveform. In chapter 3, the torque pulsation minimization method in the design stage is introduced and in chapter 4, a universal current profiling technique is proposed to reduce the torque ripple by adjusting the phase currents. Both methods are simulated and verified with the aid of finite element analysis and Matlab.

To improve the mechanical dynamic performance of permanent magnet synchronous machine, a model reference adaptive control method is proposed in chapter 5. The proposed MRAC method is based on the use of a neural network to compensate for the nonlinearity in the system. It is also simulated in Matlab/Simulink environment and the control results such as dynamic performances are confirmed. A five-phase permanent magnet motor is tested in the lab to verify the proposed model reference adaptive control method, and the dynamic performance is also compared with conventional PI controllers to further demonstrate its advantage.

The last chapter of this dissertation summarizes the accomplishment of this dissertation and introduces some on-going work about this research.

2. DESIGN OF INTERIOR PERMANENT MAGNET MOTOR AND SYNCHRONOUS RELUCTANCE MOTOR SHARING A COMMON STATOR

2.1 Introduction

With the increasing demand on the electric motors in various industrial applications, especially electric powered vehicles (electric cars, more electric aircrafts and future electric ships and submarines), both SynRM and IPM motors have gained much more attention for several reasons. They are good candidates for high performance variable speed applications. The cost of SynRM is as low as induction motors and IPM motors have a much higher power density. There is no rotor copper loss involved in either of these motors, which will reduce the entire losses and improve the power efficiency. They normally have better flux weakening capabilities for traction applications or other variable speed use. Both SynRM and IPM motors are synchronous type motors or generators which can easily share the same controllers. Developing a single stator design which can be used for both SynRM and IPM motors is a good way to reduce the manufacturing and maintenance cost. SynRM can be used as a low cost solution for a number of electric driving applications, especially when such motors are not spinning all the time at operation. There is no additional electromagnetic force when there are no currents flowing in the SynRM stator windings. IPM machines can be used in power density crucial circumstances or work as generators to satisfy the increasing demand for electrical power on board. This section deals with the design of two prototype motors, one of which is SynRM and the other one is IPM motor. Both the prototype motors share the same stator structure to provide an efficient solution for various electric driving needs.

2.2 Machine design procedure

2.2.1 The rotor diameter and total effective length

The design starts with the IPM machine airgap diameter, which is approximately the rotor diameter. The IPM machine prototype is rated as 2kW at 1800 rpm and the rated torque T is 10.6Nm. The initial design of machine size is following the D_i^2L rule, where D_i is the diameter of rotor and L is the length of the machine. The term D_i^2L indicates the volume of the machine rotor: V_R. Paper [74] summarized the published permanent magnet machine characteristics, which shows the "T/V_R" ratio is selected to be a value between 14000N/m^2 and 37000 N/m^2. For this common stator SynRM and IPM machine design, the rotor diameter is designed to be 65mm and the machine effective length is selected to be 100mm. The calculated "T/V_R" ratio is 32000 N/m^2 for IPM machine, which is a relatively high power density design.

$$D_i = 65mm \tag{2.1}$$

$$L = 100mm \tag{2.2}$$

2.2.2 Stator slot and rotor pole number design

The split ratio is defined as the ratio of stator bore diameter to stator outer diameter. For permanent magnet motors, there is an optimum split ratio which maximizes the output torque [75], as shown in Figure 2.1. The *x* axis is the flux density (*B*) ratio of the airgap flux density (B_g) and the maximum flux density (B_{max}). The maximum flux density is limited below 1.8T due to material saturation and the airgap flux density is limited below 0.9T. It has been shown that a split ratio of 0.5 is a reasonable design. Therefore, the stator diameter D_s is selected to be 130mm as an initial design.

$$D_s = 130mm \tag{2.3}$$

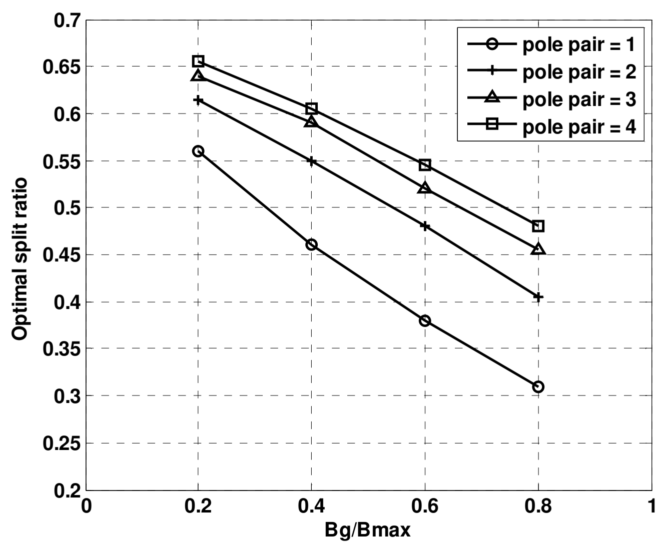

Figure 2.1: Optimal split ratio for PM machines [75].

The combination of stator slot number and rotor pole number is an important design factor. With the help of ANSYS/Maxwell simulation package, several combinations are simulated and analyzed.

(1) 6-slot, 4-pole design

6-slot stator is easily manufactured and is a good candidate for the next generation modular permanent magnet machine, which combines power electronics devices in each module. Figure 2.2 shows the models of a 6-slot, 4-pole SynRM and an IPM motor. Figure 2.3 shows the simulated torque waveform by FEA. It can be seen that the torque ripple of 6-slot, 4-pole motor is normally large which prevents its use in some low speed applications. There is another disadvantage of 6-slot, 4-pole structure preventing it from being used for common stator design. The SynRM performance is not as good as IPM motor.

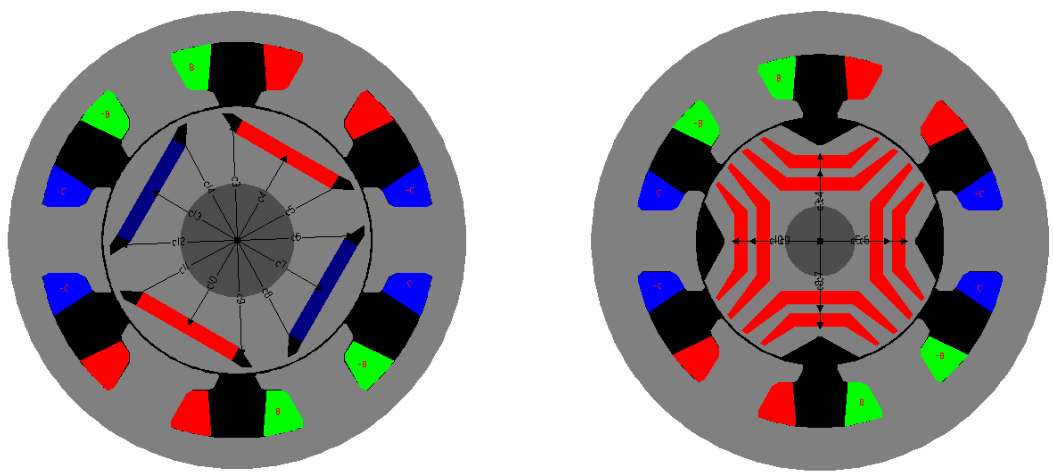

(a) (b)

Figure 2.2: 6-slot, 4pole IPM motor and SynRM model in Maxwell software, (a) IPM motor model; (b) SynRM model.

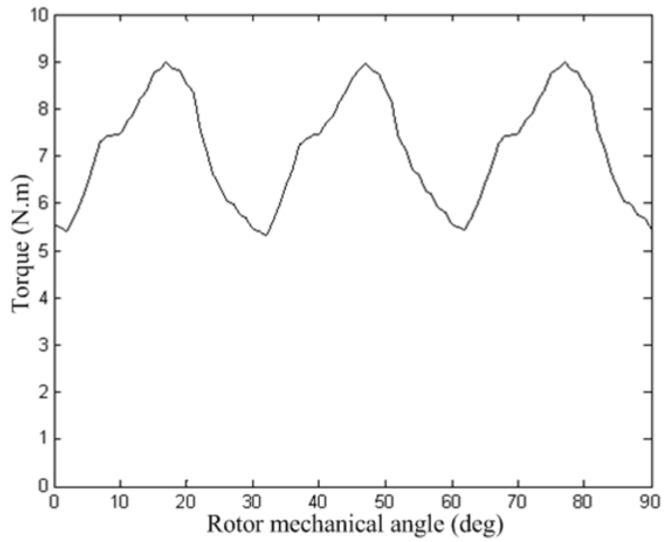

(a)

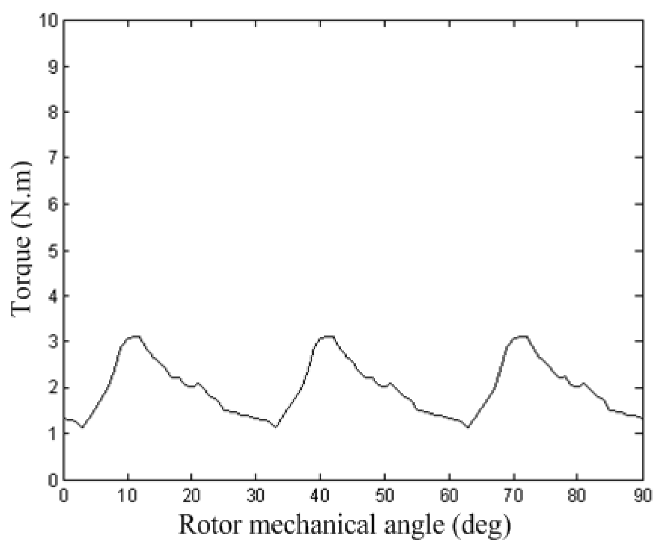

(b)

Figure 2.3: Simulated electromagnetic torque waveform, (a) Torque waveform of IPM motor; (b) torque waveform of SynRM.

(2) 9-slot, 4-pole design

In this section, 9-slot, 4-pole SynRM and IPM motors are designed and modeled in Maxwell, as shown in Figure 2.4. The performance of these motor are compared in Figure 2.5. The SynRM is not a good design as the average torque is not high enough to be comparable to the IPM motor. At the same time, the torque ripple is very high even though the rotor structure has been optimized.

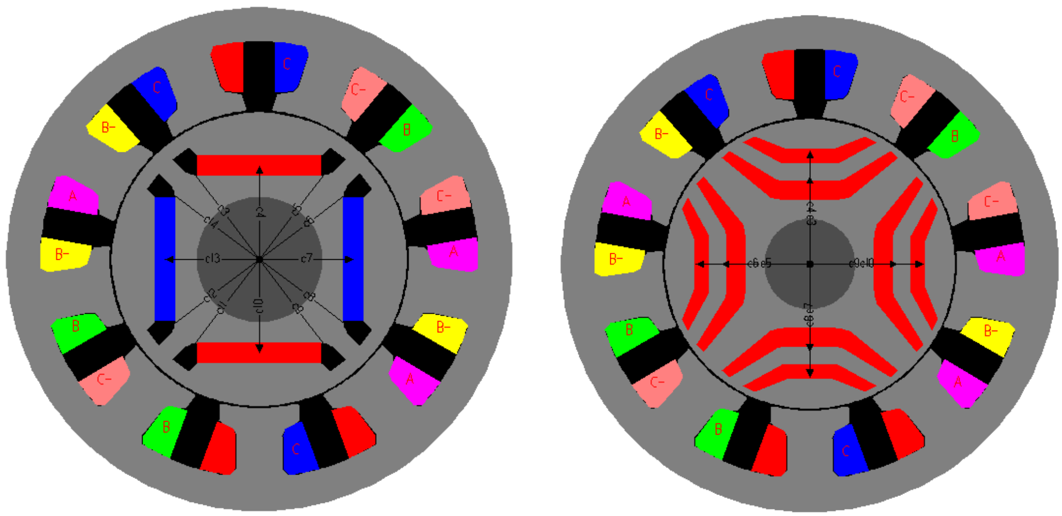

(a) (b)

Figure 2.4: 9-slot, 4pole IPM motor and SynRM model in Maxwell software, (a) IPM motor model; (b) SynRM model.

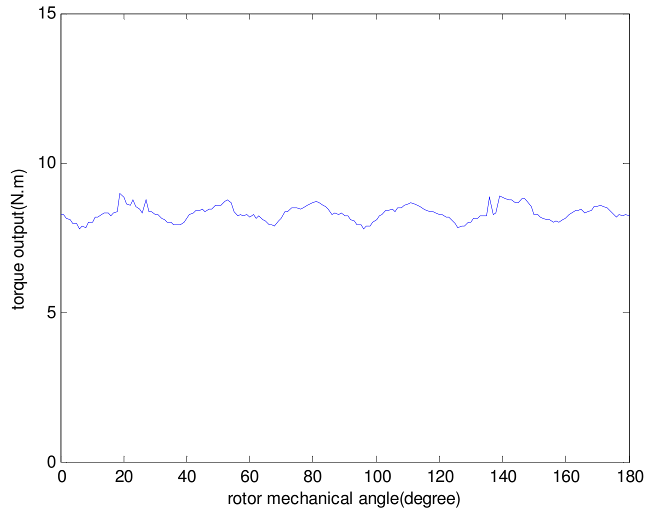

(a)

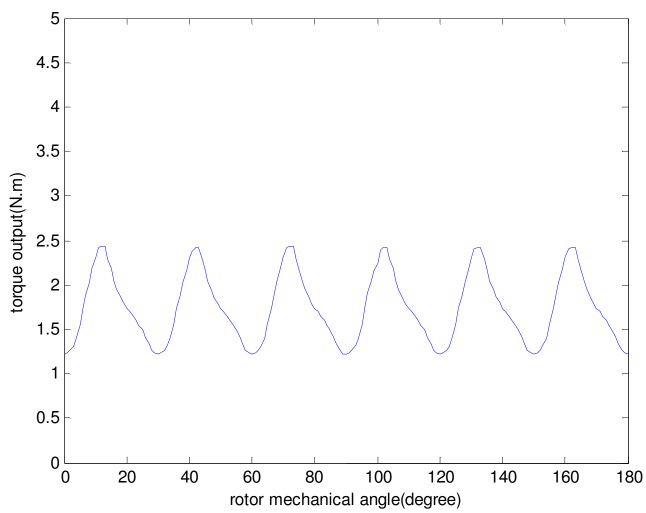

(b)

Figure 2.5: Simulated electromagnetic torque waveform, (a) Torque waveform of IPM motor; (b) torque waveform of SynRM.

(3) 12-slot, 4-pole design

The 12-slot common stator is analyzed through FEA. Figure 2.6 shows the Maxwell models for a SynRM and an IPM motor of this structure. From Figure 2.7 , it can be seen that both motors feature a high average output torque, but the torque ripple is high. The reason for this comes from both the high cogging effect and the high back-EMF harmonics as a result of the stator winding distribution. Figure 2.8 shows the high cogging torque of 12-slot, 4-pole IPM motor.

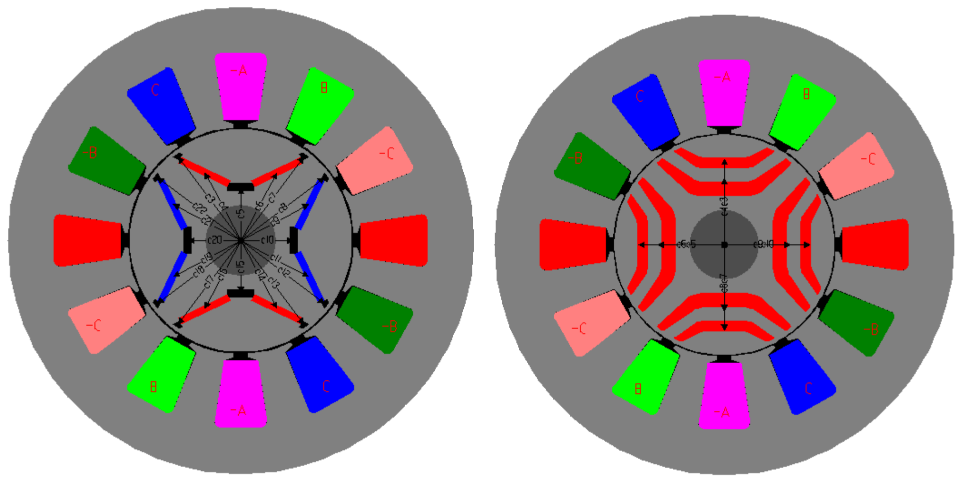

(a) (b)

Figure 2.6: 12-slot, 4pole IPM motor and SynRM model in Maxwell software, (a) IPM motor model; (b) SynRM model.

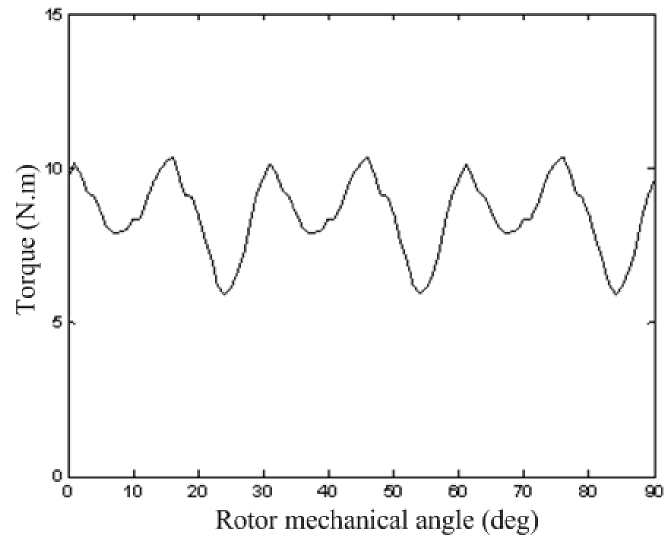

(a)

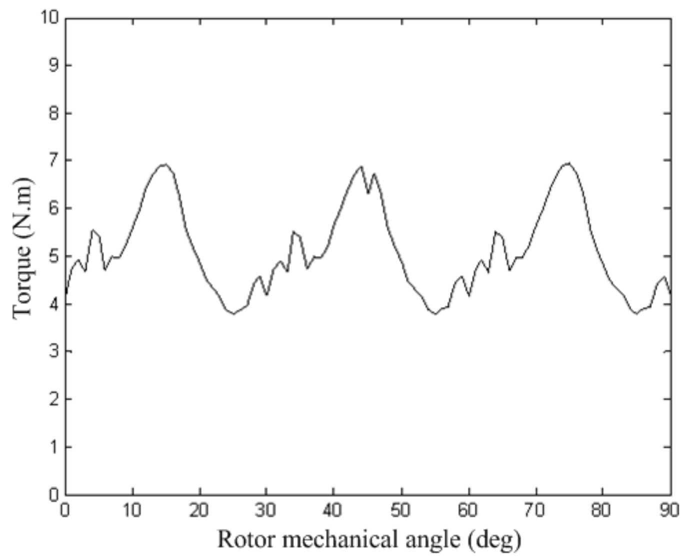

(b)

Figure 2.7: Simulated electromagnetic torque waveform, (a) Torque waveform of IPM motor; (b) torque waveform of SynRM.

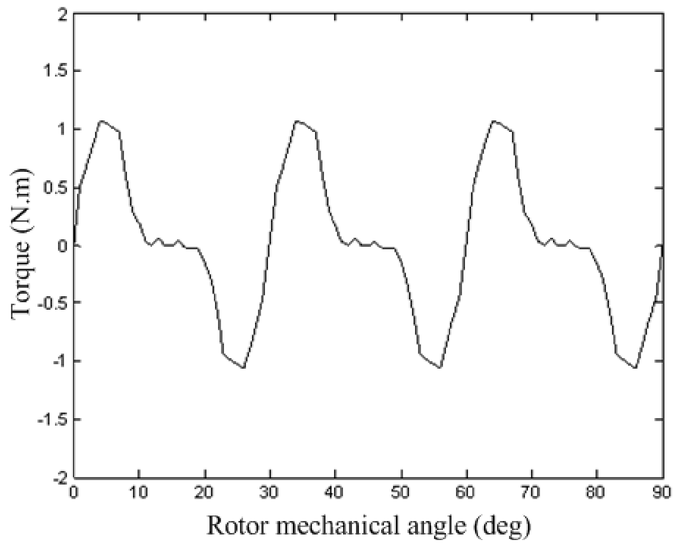

Figure 2.8: Cogging torque simulation of the 12-slot, 4-pole IPM motor.

(4) 15-slot, 4-pole design

The stator windings in the 15-slot stator can be arranged in double layers. Figure 2.9 shows the Maxwell model of a 15-slot, 4-pole SynRM and an IPM motor. The advantage of 15-slot stator is that the cogging effect is minimum and the back-EMF waveform is sinusoidal with minimum harmonic components. As a result, the produced torque ripple is low. The simulation results validate this conclusion, as shown in Figure 2.10. The disadvantage of 15-slot stator structure is high vibration and noise during operation due to the asymmetrical stator winding distribution.

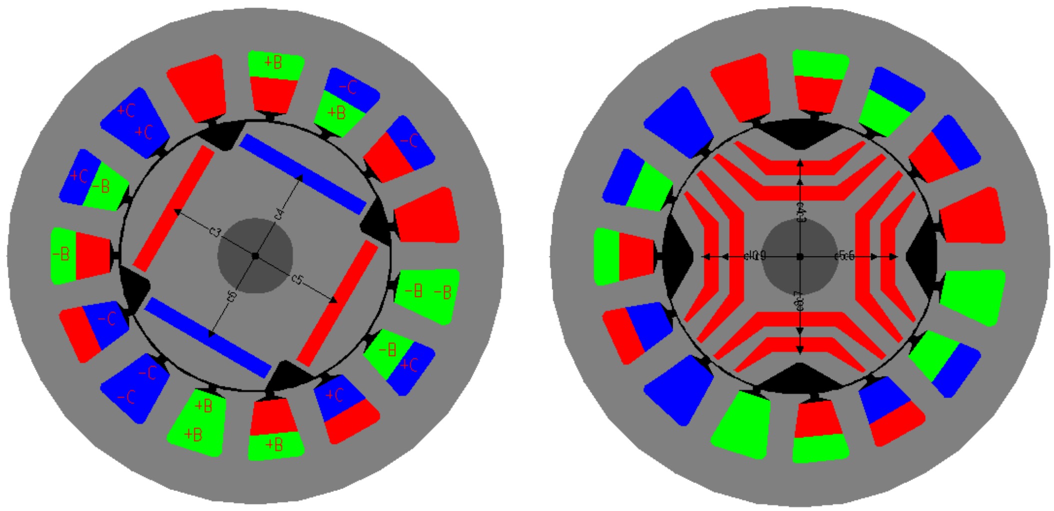

(a) (b)

Figure 2.9: 15-slot, 4pole IPM motor and SynRM model in Maxwell software, (a) IPM motor model; (b) SynRM model.

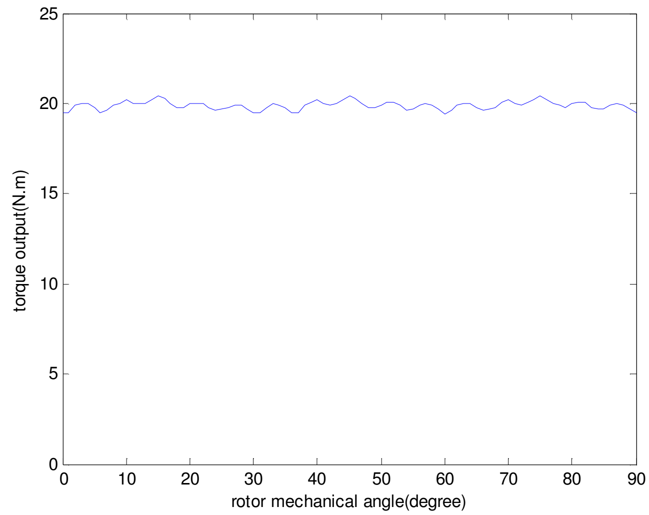

(a)

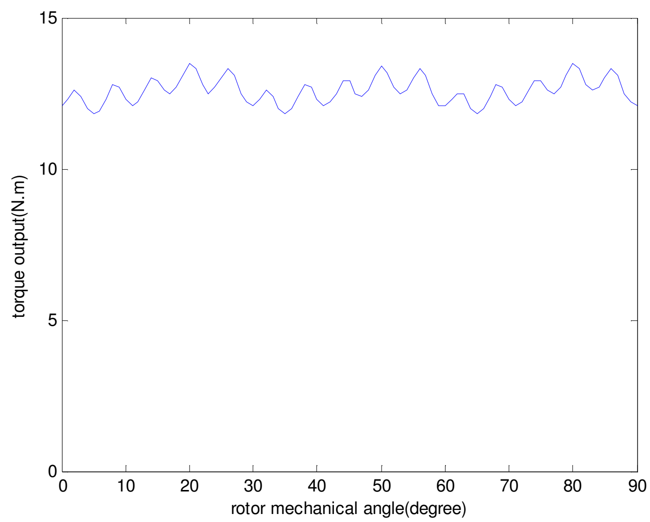

(b)

Figure 2.10: Simulated electromagnetic torque waveform, (a) Torque waveform of IPM motor; (b) torque waveform of SynRM.

(5) 18-slot, 4-pole design

A 2-layer 18-slot stator structure is used with full-pitch winding distribution. The winding factor can be maximized to make full use of the back-EMF constants and generate as high torque as possible. As this is the selected structure for the prototyping, performance comparison will be conducted in the following sections. Figure 2.11 shows the basic structure of the stator designed. Table 2.1 includes the design specifications of the stator.

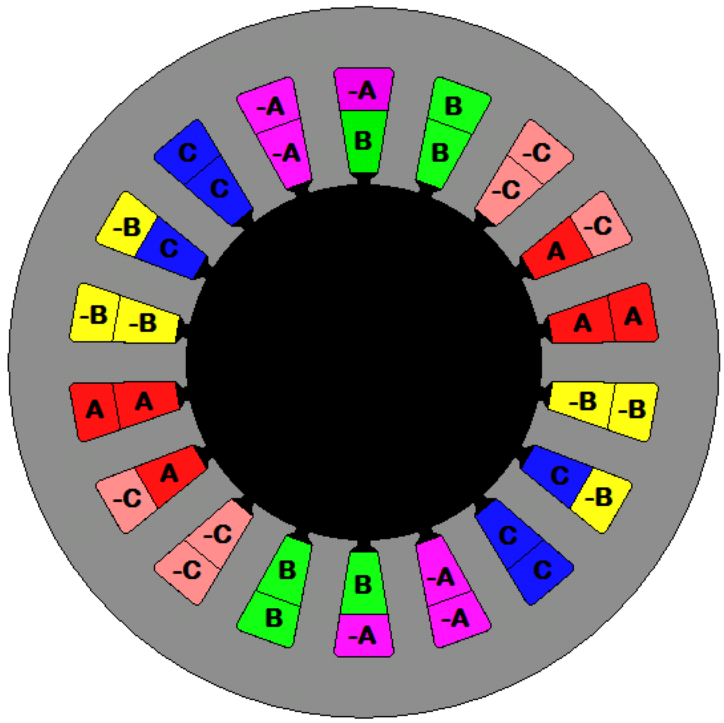

Figure 2.11: Cross section of the 18-slot stator.

Table 2.1: Common stator parameters.

Stator External Diameter	130 mm
Stator Internal Diameter	65 mm
Number of Slots	18 slots
Stack Length	100 mm

(6) 36-slot, 4-pole design

A 36-slot stator structure is regularly used in three-phase induction motors, and is also a good candidate for a common stator for both SynRM and IPM motors. Figure 2.12 shows the Maxwell models for a SynRM and an IPM motor. It can be seen from Figure 2.13 that Both SynRM and IPM motors have good performance. The torque ripple can be minimized by optimizing the rotor permanent magnet or flux barrier configurations. The problem in this design is the relatively complex stator, which is not easily manufactured for small size motors.

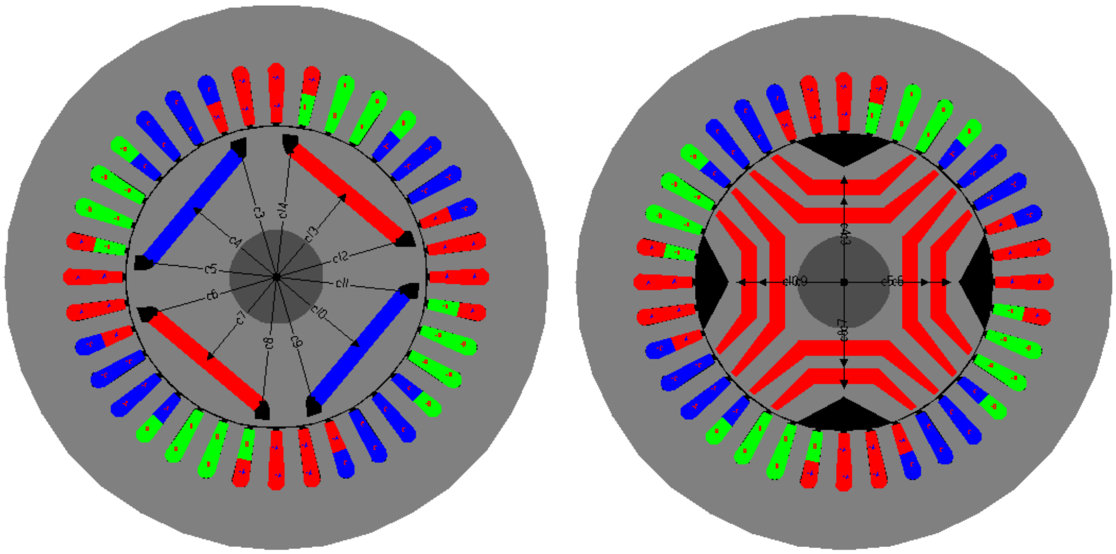

(a) (b)

Figure 2.12: 36-slot, 4pole IPM motor and SynRM model in Maxwell software, (a) IPM motor model; (b) SynRM model.

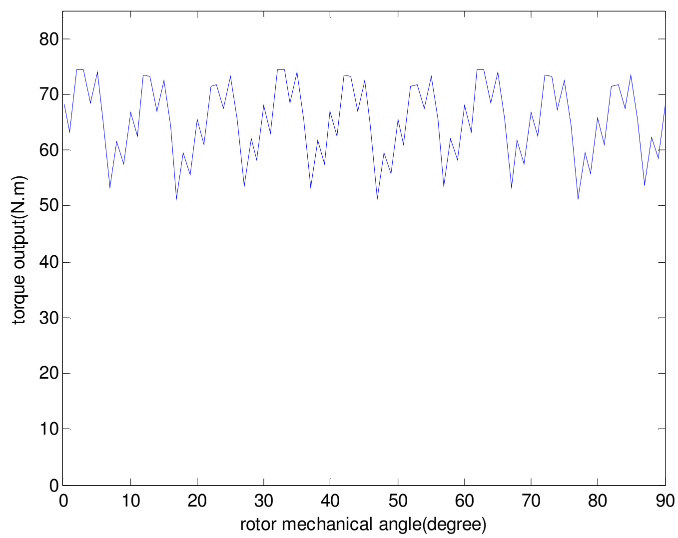

(a)

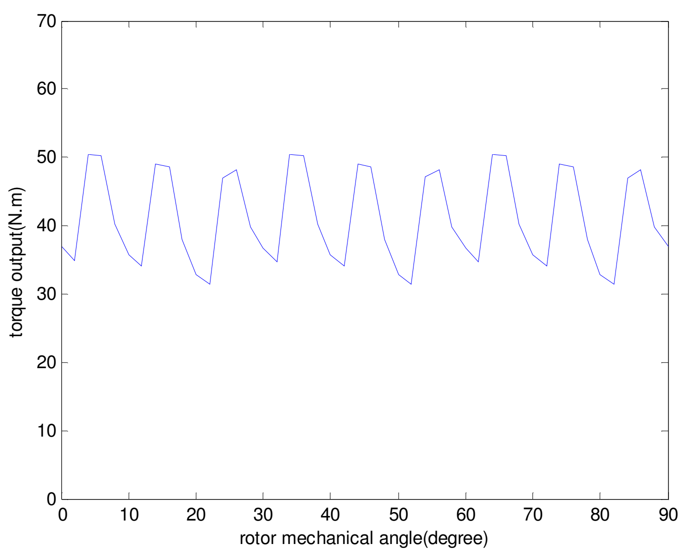

(b)

Figure 2.13: Simulated electromagnetic torque waveform, (a) Torque waveform of IPM motor; (b) torque waveform of SynRM.

(7) 9-slot, 8-pole design

9-slot, 8-pole structure is a good design for permanent magnet machines. In this part of research, a SynRM is also designed and analyzed to compare with 9-slot, 8-pole IPM motor. In this design, the rotor structure of the SynRM is the same as that of the IPM motor, as shown in Figure 2.14. This structure is good for permanent magnet motor with high average torque and low torque ripple, as shown in Figure 2.15 (a). However, as shown in Figure 2.15 (b), SynRM designed based on this structure has relatively lower reluctance torque, making it less competitive.

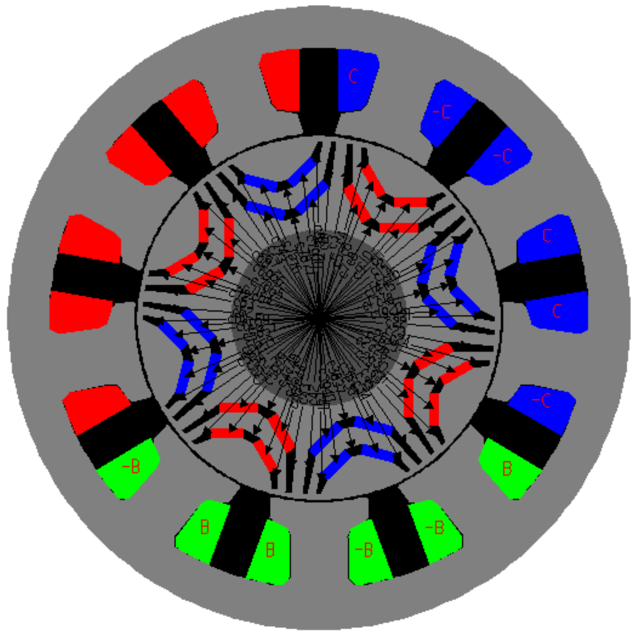

Figure 2.14: Common structure for both SynRM and IPM motor. (SynRM rotor is without magnets.)

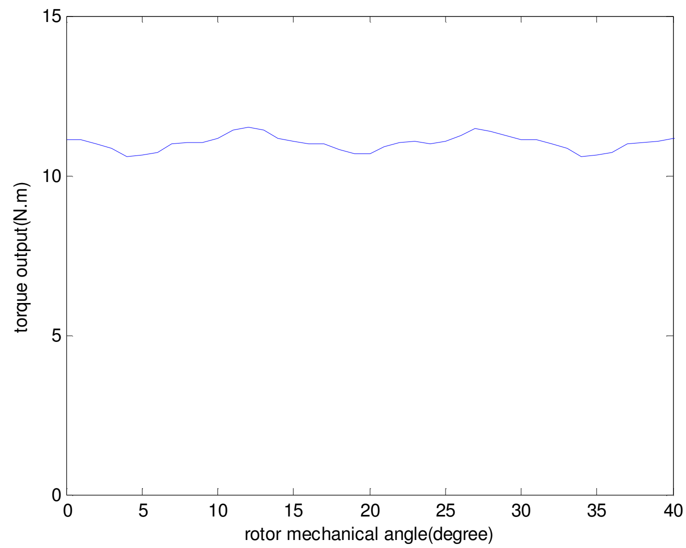

(a)

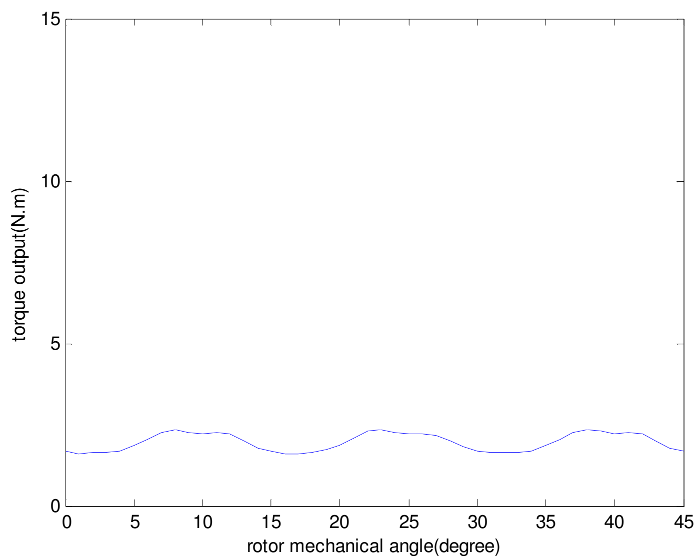

(b)

Figure 2.15: Simulated electromagnetic torque waveform, (a) Torque waveform of IPM motor; (b) torque waveform of SynRM.

(8) 18-slot, 8-pole design

In order to generate enough saliency in 8-pole rotors, a larger rotor shaft is used in this 18-slot, 8-pole design. The models in Maxwell are shown in Figure 2.16. The IPM motor can be designed easily to generate enough torque with low torque ripple, as shown in Figure 2.17 (a). The reluctance torque generated by the SynRM rotor is less than half of that in the IPM motor. The torque waveform is shown in Figure 2.17 (b). This design will be suitable for some applications where the rotor moment of inertia is a key concern, as this design features a relatively large rotor shaft, which means the inertia of rotor is much lower if making the shaft hollow.

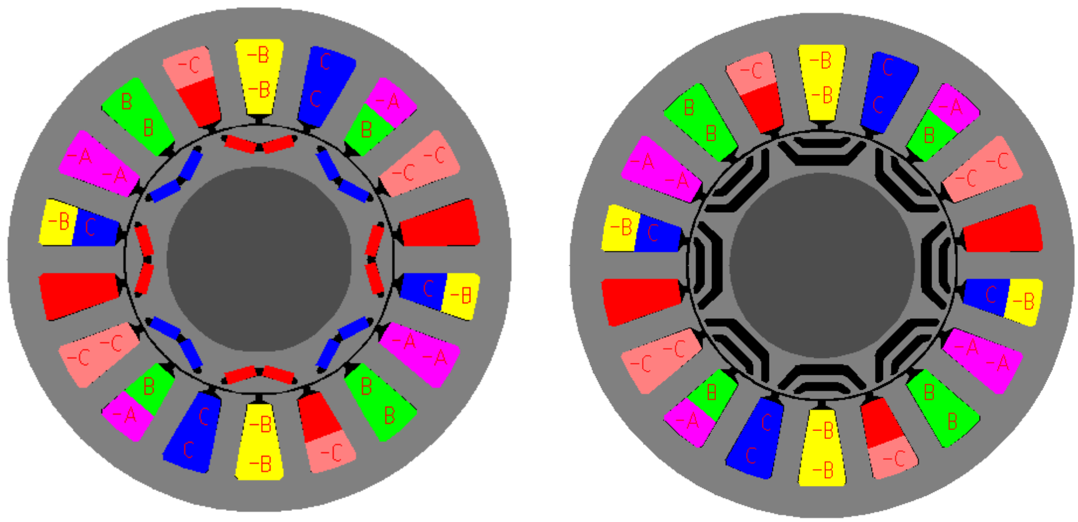

(a) (b)

Figure 2.16: 18-slot, 8pole IPM motor and SynRM model, (a) IPM motor model; (b) SynRM model.

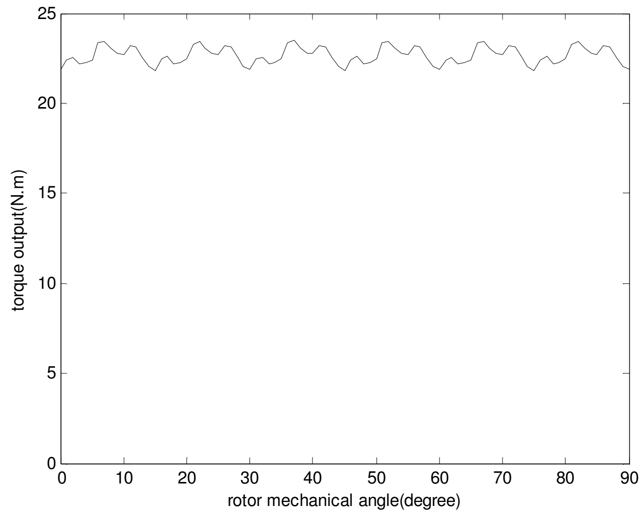

(a)

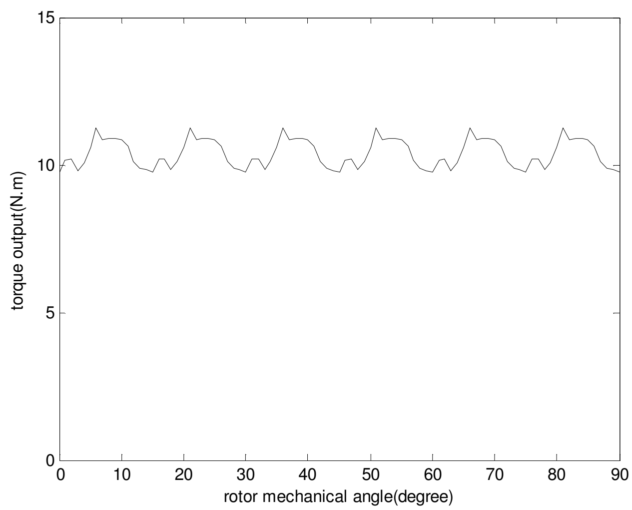

(b)

Figure 2.17: Simulated electromagnetic torque waveform, (a) Torque waveform of IPM motor; (b) torque waveform of SynRM.

The special requirement for this study is that a common design should be selected to make both SynRM and IPM motor have relatively high average torque and low torque ripple to be competitive. After investigating all the stator slot/rotor pole combinations, the 18-slot 4 pole design has been selected for prototyping. Table 2.2 lists the summary of advantages and disadvantages of the stator slot/rotor pole combinations investigated.

Table 2.2: Summary of advantages and disadvantages of the slot/pole structure considered for prototyping of common stator SynRM and IPM machine.

No. of slot	No. of pole	Advantage	Disadvantage
6	4	Modular design	High torque ripple; low reluctance torque
9	4	Modular design	High torque ripple; low reluctance torque
12	4	High average torque	High cogging torque; high harmonics
15	4	Low torque ripple; Low harmonics	Asymmetrical winding distribution
18	4	High reluctance torque; full pitch winding	
36	4	Suitable for both SynRM and IPM	Difficult to manufacture for small size prototypes
9	8	Good IPM performance, low torque ripple	Low reluctance torque
18	8	Low torque ripple; low rotor inertia	Low reluctance torque

2.2.3 Stator winding design

Slot shape is chosen and optimized to make full use of teeth area for magnetic flux to pass through and maximum slot area for copper wires as well. The slot shape is also optimized to provide both enough stator teeth width for electromagnetic flux and enough space for current carrying copper wires. The conductor selected is AWG-25 wire. The phase conductor is made of 16 wires in a bundle. Therefore, the phase rated current is 20 Amps. Table 2.3 summarizes the design data for the winding design, and Figure 2.18 shows the filling effect in a single slot.

Table 2.3: Stator winding parameters.

Conductor	AWG-25
Number of parallel conductors per phase	16
Max currents per phase	20A
Number of turns	10
Number of coils per phase (in series)	6

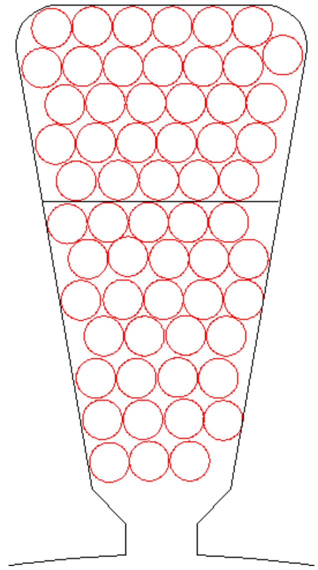

Figure 2.18: Stator winding filling in a single slot.

The winding coil connections are following a symmetrical distribution. Figure 2.19 shows the definition of each coil and Figure 2.20 illustrates the connection of each coil.

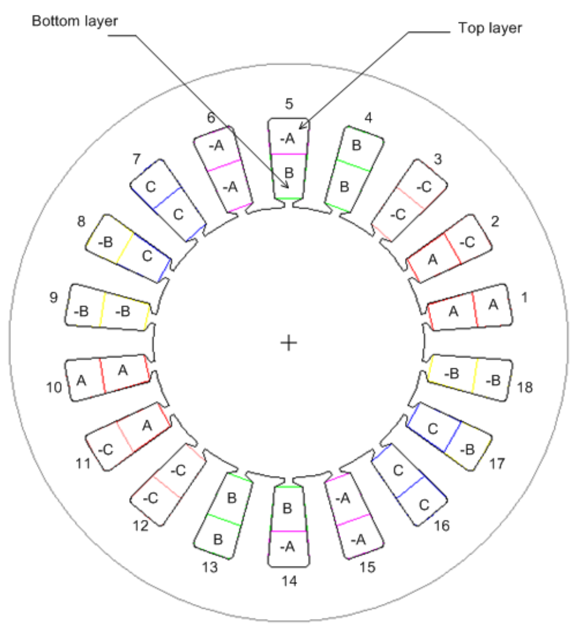

Figure 2.19: Slot number definition.

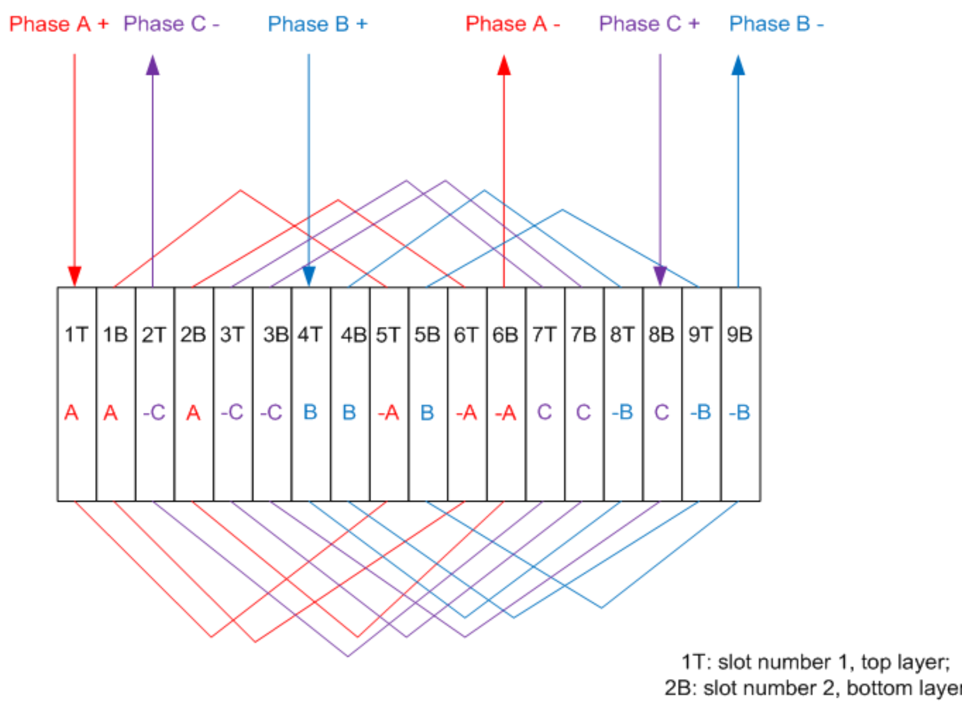

Figure 2.20: Winding coil design (half of the entire windings: 9slots).

2.2.4 SynRM rotor design

A 4-pole double layer transversely laminated rotor structure is selected. The rotor structure is shown in Figure 2.21. Table 2.4 shows the rotor design specifications. The SynRM simulated performance will be included in the next section.

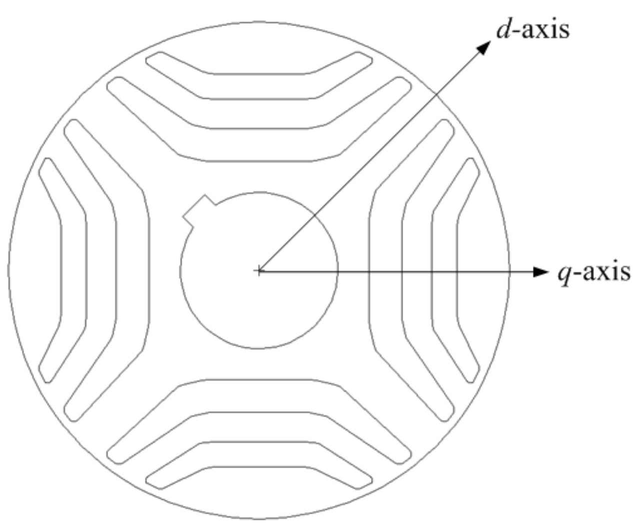

Figure 2.21: SynRM rotor design.

Table 2.4: Parameters of SynRM rotor design.

rotor external diameter	64.2 mm
shaft diameter	20.2 mm
Airgap length	0.4 mm
Max torque current angle (with respect to d-axis)	45^o
Simulation speed	1800rpm

2.2.5 IPM machine rotor design

The IPM motor also uses a 4-pole rotor structure. Eight identical pieces of permanent magnet blocks are inserted into the rotor symmetrically. The rotor structure is shown in Figure 2.22. Table 2.5 shows the design data for the IPM machine rotor. The manufactured IPM machine rotor and SynRM rotor are shown in Figure 2.23.

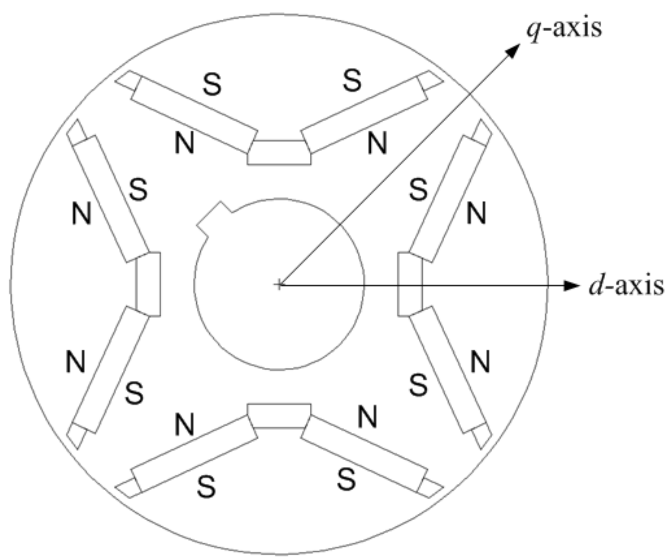

Figure 2.22: IPM machine rotor design.

Table 2.5: Parameters of IPM rotor design.

rotor external diameter	63.8 mm
shaft diameter	20.2 mm
Airgap length	0.6 mm
Max torque current angle (with respect to d-axis)	122^o
Simulation speed	1800rpm

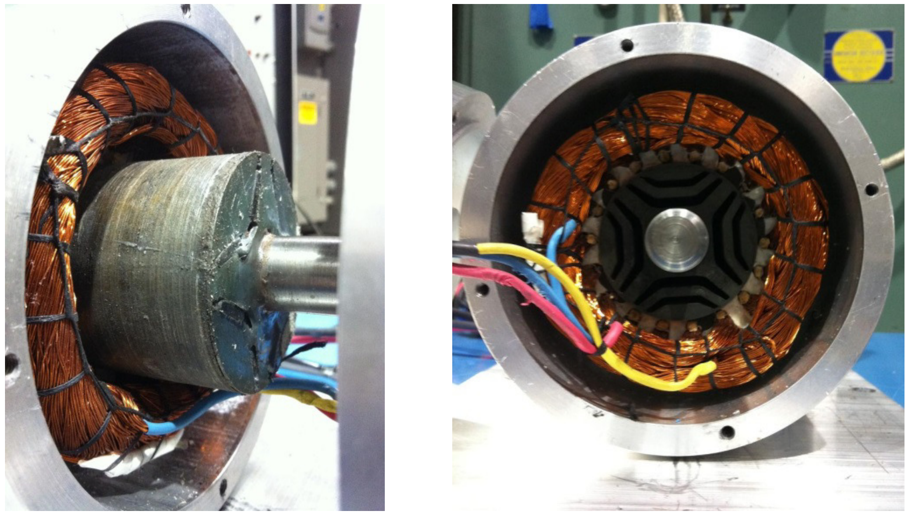

(a)IPMSM **(b) SynRM**

Figure 2.23: Prototype IPMSM and SynRM.

2.3 FEA simulation results

2.3.1 IPM machine back-EMF

The back-EMF information is critical for IPM machines. In the design stage, analysis of the back-EMF information is necessary. Figure 2.24 shows the simulated IPM machine back-EMF at 1800rpm.

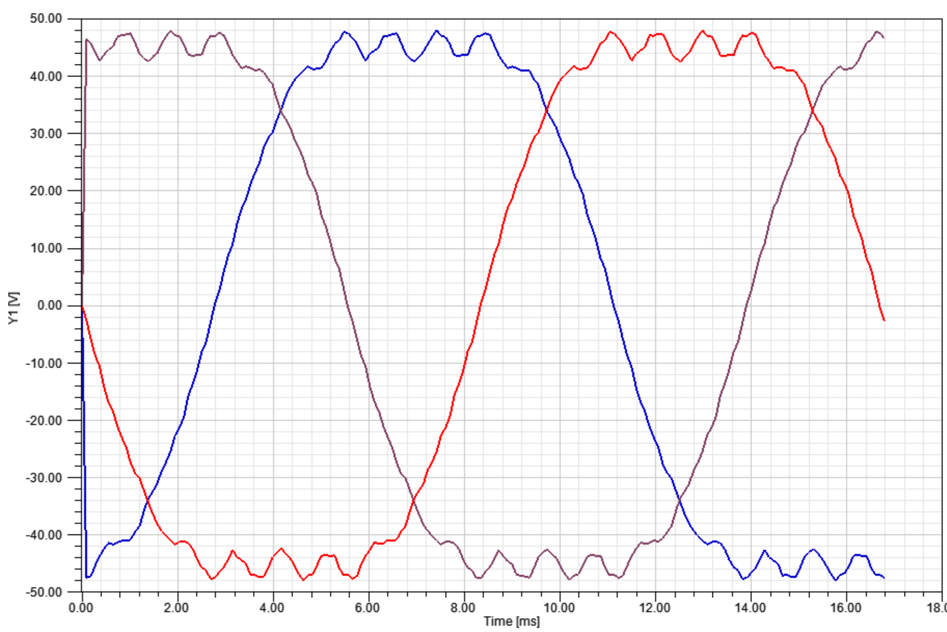

Figure 2.24: IPM machine three-phase back-EMF at 1800rpm.

2.3.2 The torque performance comparison

The torque performance of the IPM machine and SynRM is analyzed with the finite element simulation software package. Figure 2.25 and Figure 2.26 show the torque waveforms of both IPM machine and SynRM, respectively. The current injected is 20 A (peak) symmetrical three-phase currents. Table 2.6 shows the specification and simulation result comparison of SynRM and IPM motors.

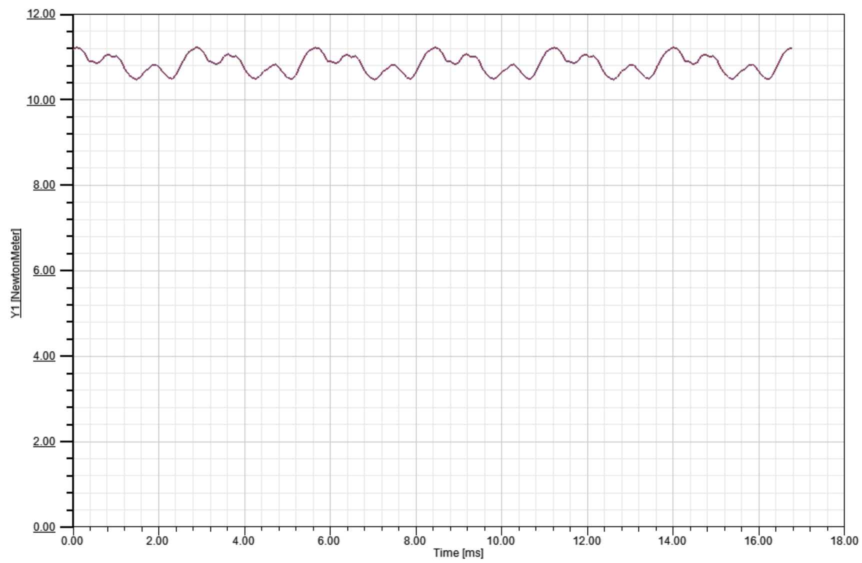

Figure 2.25: IPM machine torque performance.

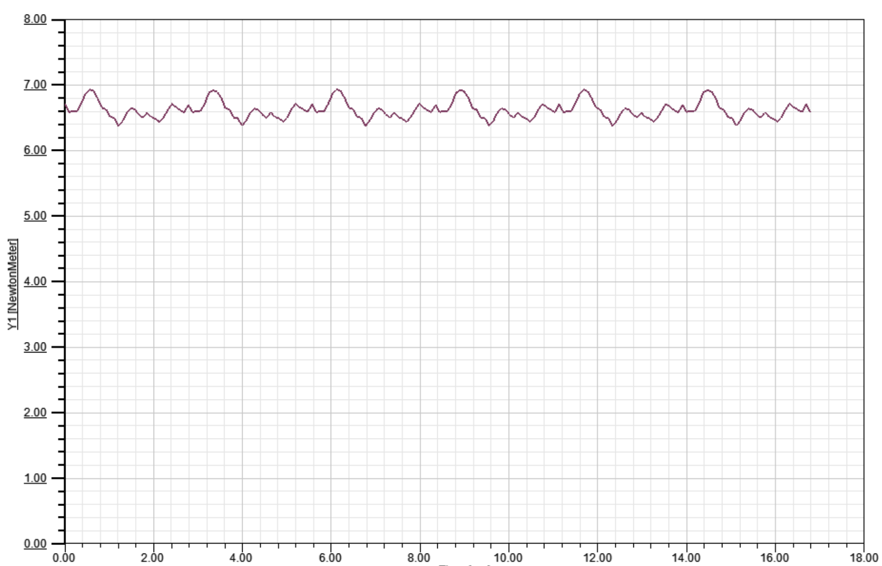

Figure 2.26: SynRM torque performance.

Table 2.6: Comparison of SynRM and IPM motor specifications and simulation results.

	IPM	SynRM
Rotor external diameter	63.8mm	64.2mm
Air gap length	0.6mm	0.4mm
Simulated speed	1800rpm	1800rpm
Max current per phase	20A	20A
Number of turns	12	12
Simulated torque	10.8Nm	6.6Nm

2.4 Machine housing and mechanical support design

2.4.1 Machine overall clearance

The front shaft is 20.2mm in diameter, with a 4.75mm square keyway. The key is designed to go with the front shaft, which will be mounted to the test bed. As shown in Figure 2.27, the total height of the shaft center should be less than 90mm, which is designed to be 85mm. The rear shaft design is depending on the encoder.

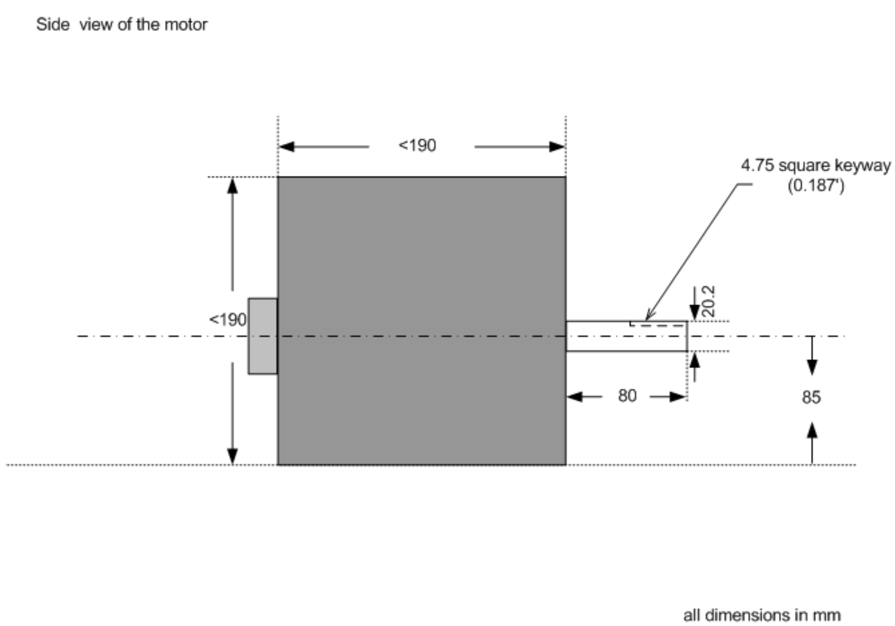

Figure 2.27: Motor side view.

2.4.2 Connection to the test bed

6-bolt connector is used to install the motor to the test bed. The positions of the bolts and the pre-prepared holes in the machine front cover are shown in Figure 2.28.

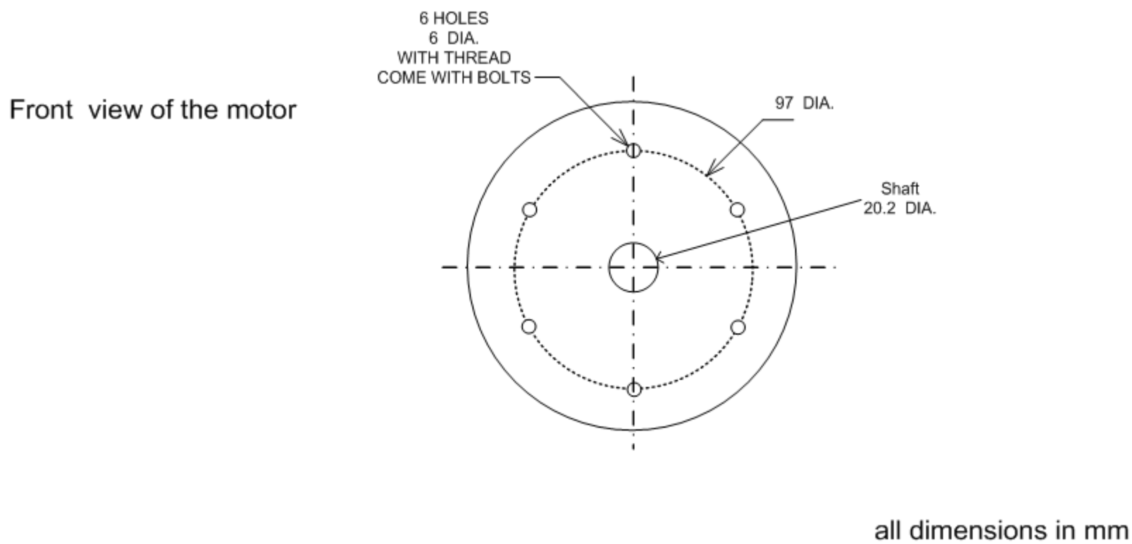

Figure 2.28: Motor front view.

2.5 Experimental Results

2.5.1 Experimental setup

Figure 2.29 shows the configuration of the experimental setup and Figure 2.30 shows the complete block diagram of the motor drive system. The motors under test are prototype common stator IPM motor and SynRM. A three-phase IGBT-based VSI is connected to the DC bus to drive the motor. The interface board contains A/D, D/A units and hysteresis current controllers. An optical incremental encoder is installed on the motor shaft to provide rotor position information. The stator currents are measured by high frequency Hall-effect transducers and fed through the A/D converters into the dSPACE DS1104 Controller board. The current sensing frequency is 20 kHz. The hysteresis current controller is implemented with LM339 comparator. The three phase current commands i_a^*, i_b^* and i_c^* are first generated in the dSPACE DS1104 Controller according to different control algorithms. Then, they are compared with the measured currents to generate the control signals of the PWM inverter. The motor shaft is connected to an induction machine which works as a programmable mechanical load. The induction machine is connected to the power grid using a bidirectional AC-DC-AC converter. Unlike conventional test beds, the generated electric energy is not wasted by heat but fed back into the grid, making this experimental test bed an environmentally-friendly lab setup. Figure 2.31 shows the photo of the designed experimental setup.

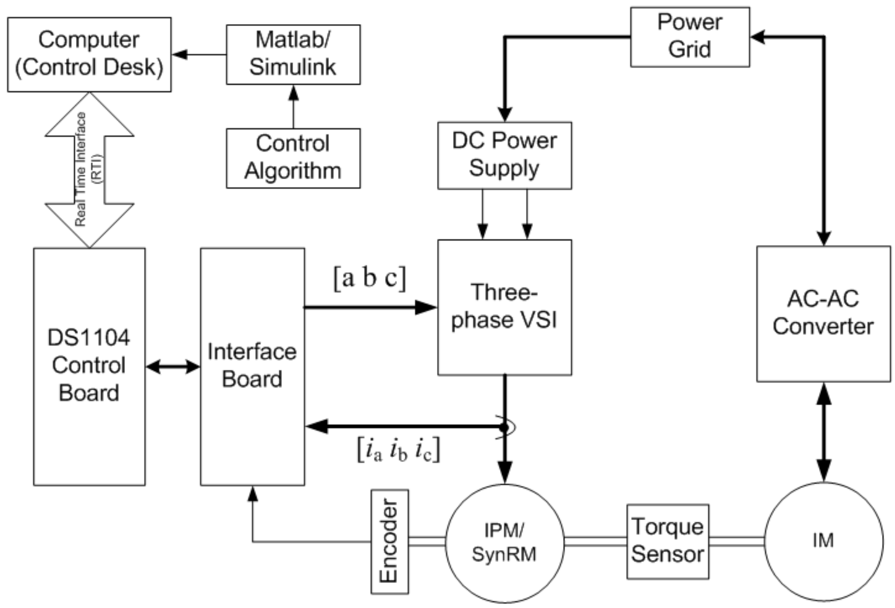

Figure 2.29: Experimental drive system configuration.

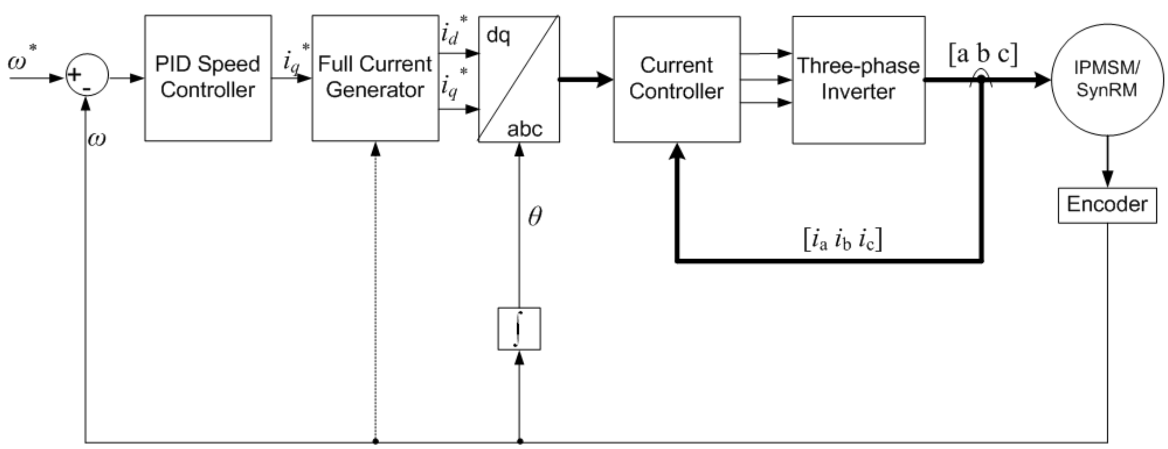

Figure 2.30: Complete block diagram of the motor drive system.

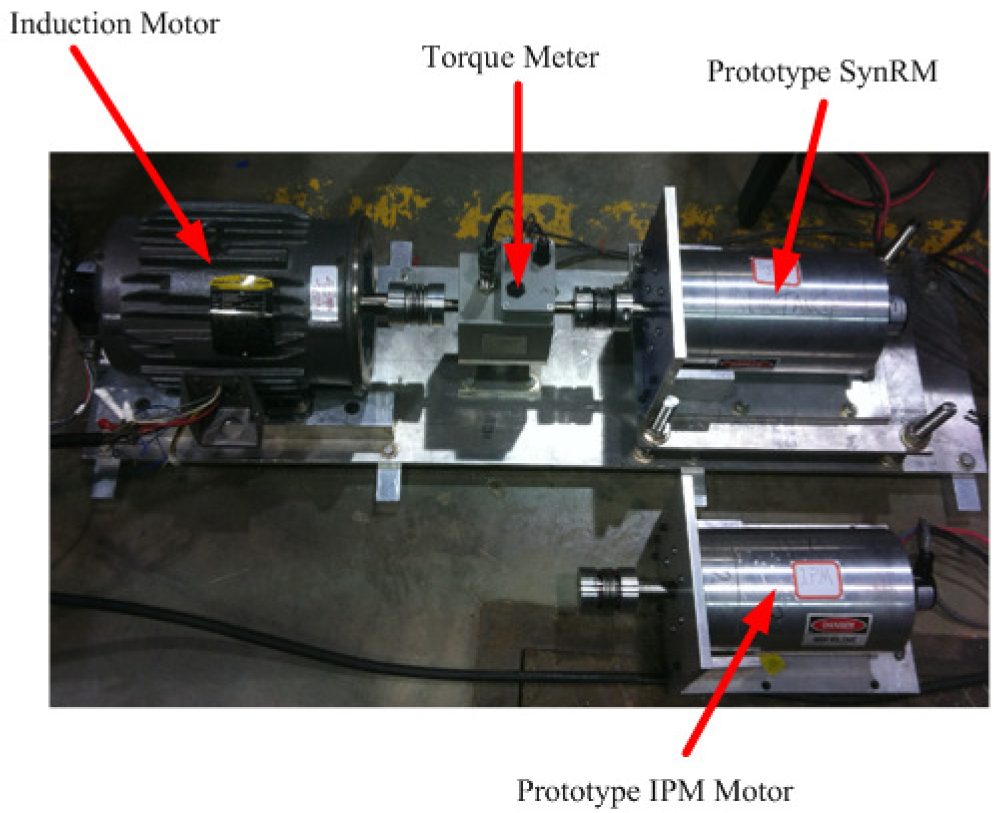

Figure 2.31: Photo of the experimental setup.

2.5.2 Parameter analysis of the prototypes IPM motor and SynRM

(a) DC resistance

As two prototypes motors share the same stator structure, the DC resistance will be the same. The neutral line is not designed to be available in either of the prototype motors. The terminal resistance between A and B: R_{AB} is physically measured at room temperature. The equivalent resistance per phase

$$r_s = 0.27 \quad \Omega \tag{2.4}$$

(b) Permanent magnet flux constant λ_m and Back-EMF verification

No load test is implemented to measure the permanent magnet flux constant λ_m. The induction motor is driving the prototype IPM machine at different speeds. The terminal back-EMF data between phase A and B are recorded as in Table 2.7. The permanent magnet flux constant is calculated to be:

$$\lambda_m = 0.13 \quad Wb \tag{2.5}$$

Table 2.7: No load back-EMF test data of the prototype IPM motor.

Speed (rpm)	Back-EMF (V_{AB}-peak /V)
300	15
450	22
600	29
750	36
900	43
1050	50
1200	57
1350	64
1500	71
1650	78
1800	85

At the speed of 1800rpm, the line to line back-EMF waveform is recorded as in Figure 2.32. It is compared with the line to line back-EMF from FEA simulation, which is illustrated in Figure 2.33. The back-EMF waveform matches with each other after calibrating the permanent magnet residual flux density in the FEA simulation. Figure 2.34 compares the frequency components of the simulated back-EMF data and the measured back-EMF data.

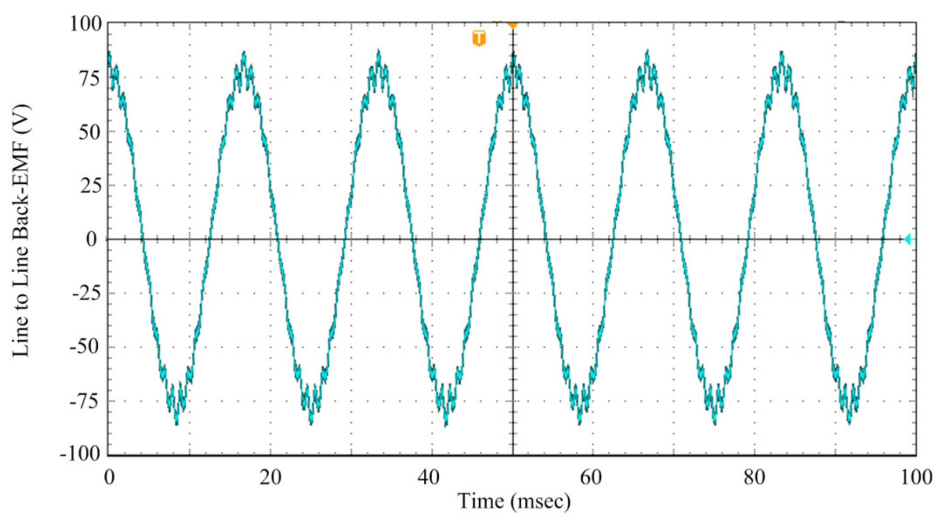

Figure 2.32: Measured line to line back-EMF of the IPM machine at 1800rpm.

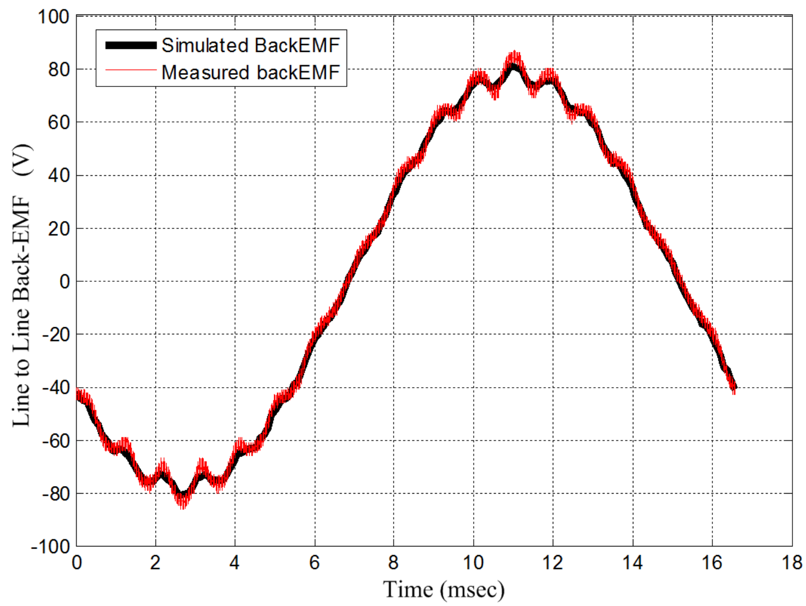

Figure 2.33: Simulated line to line back-EMF of the IPM machine by FEA at 1800rpm.

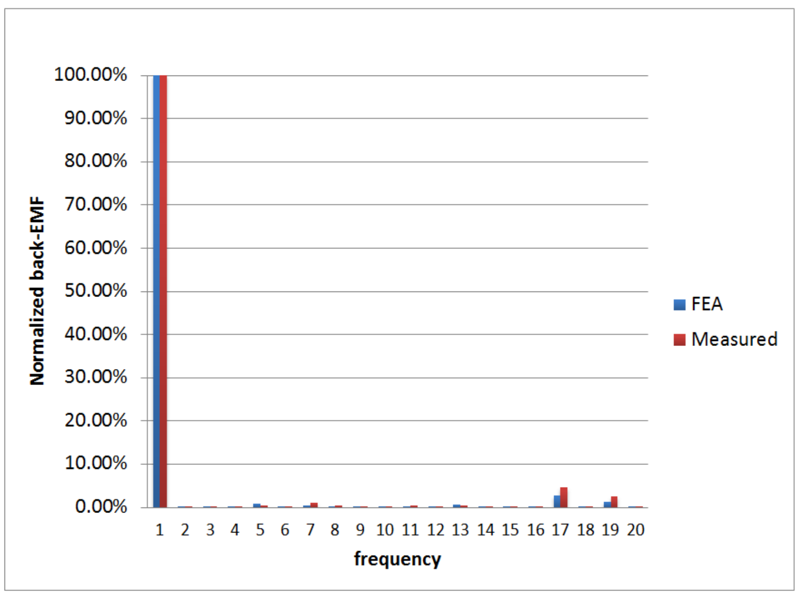

Figure 2.34: Comparison of frequency components of simulated line to line back-EMF of the IPM machine and measured back-EMF at 1800rpm.

(c) Inductance Saturation

The permanent magnet flux λ_m varies with temperature. λ_m is a constant value if room temperature is assumed and the machine is properly cooled. However, inductances L_d and L_q will change values with different current excitations due to saturation in electrical steel. It is an important factor in designing the machine and its corresponding drive system. Even though the two prototype motors share the same stator, the inductances may differ from each other due to different rotor structure. Accurate knowledge of IPM machine inductance parameters is important in controlling the machine efficiently, both in MTPA control and flux weakening control. The situation is similar in SynRM, where the reluctance torque due to inductance difference (saliency) is the only source of effective torque. With the aid of FEA, the magnetic saturation effects of L_d and L_q are in the prototype SynRM and IPMSM are shown in Figure 2.35 and Figure 2.36, respectively. Currents of up to 2.5 pu are provided to emphasize the magnetic saturation effects.

In Figure 2.35, it can be seen that in SynRM, *d*-axis inductance L_d saturates much faster than L_q, resulting a decreased saliency L_d - L_q value as the current goes up. It is easy to prove that the maximum torque control of SynRM is to control i_d to be equal to i_q [76]. With fixed current rating, higher torque will be produced if the saliency ratio is higher. In the prototype SynRM, the magnetic saturation will affect the overall loading ability.

Figure 2.36 shows that in IPMSM, due to the designed structure and existence of permanent magnets, saturation effect of *d*-axis inductance L_d is negligible both in flux weakening range and flux intensifying range, but the effect of saturation for L_q is much greater than that for L_d. MTPA control of the prototype IPMSM will be taken as an example to illustrate the importance of considering inductance saturation effect. Figure 2.37 shows the experimental results of current vs. torque curves under MTPA control. For the solid curve, the IPMSM is driven by using constant L_q parameter obtained at 1 pu current (as shown in Figure 2.36). If considering the saturation effect of L_q, L_q curve in Figure 2.36 has been fitted by a 3rd order polynomial. The *d*-axis reference current id is calculated using corresponding L_q. The dotted curve in Figure 2.37 shows the results considering the saturation effect of L_q. It can be seen that the generated torque for certain current is higher if L_q saturation is considered. The reason why these two curves merge at full load is that the real L_q at full load is selected to work as the L_q constant.

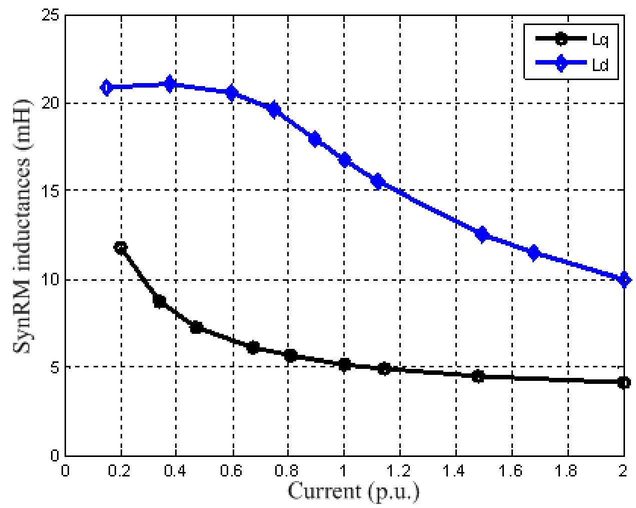

Figure 2.35: SynRM inductance saturation effect: x-axis is i_d for L_d curve and i_q for L_q curve.

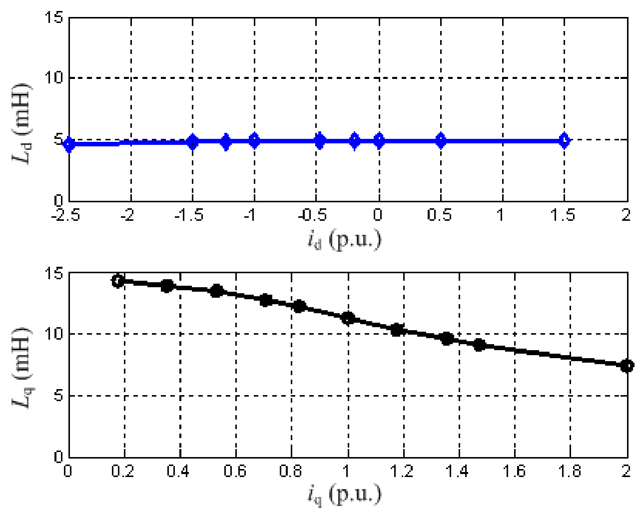

Figure 2.36: IPMSM inductance saturation effect.

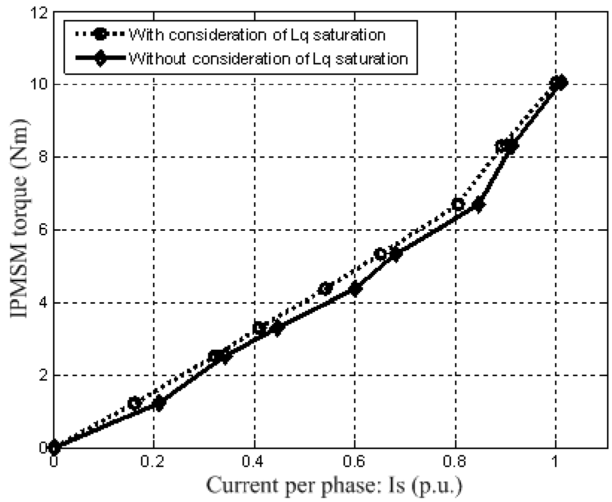

Figure 2.37: Comparison of MTPA control of prototype IPMSM considering L_q saturation and without considering L_q saturation.

2.5.3 Full load tests of the prototype IPM motor and SynRM

Full load tests are conducted for both IPM motor and SynRM. To generate the maximum torque at the minimum phase current, *d*-axis current is controlled to be the same as *q*-axis current in SynRM. The Maximum torque per ampere (MTPA) point in the IPM machine is found with the help of finite element analysis. The current vector should be 122^o ahead of *d*-axis. Without further notice, the prototype motors are controlled following this method. Figure 2.38 and Figure 2.39 show the SynRM phase current and the instantaneous torque waveform, respectively. The SynRM is operating at 600rpm to maintain a relatively low DC-bus voltage. The average torque generated is 6.5Nm at full load. In Figure 2.40 and Figure 2.41, the phase current and instantaneous torque waveforms of the prototype IPM motor are shown, respectively. The average torque is 10.0Nm. Figure 2.42 shows the measured torque of the prototype IPM machine when it is controlled with only magnetic torque (i_d^*=0). The average torque is 7.2Nm.

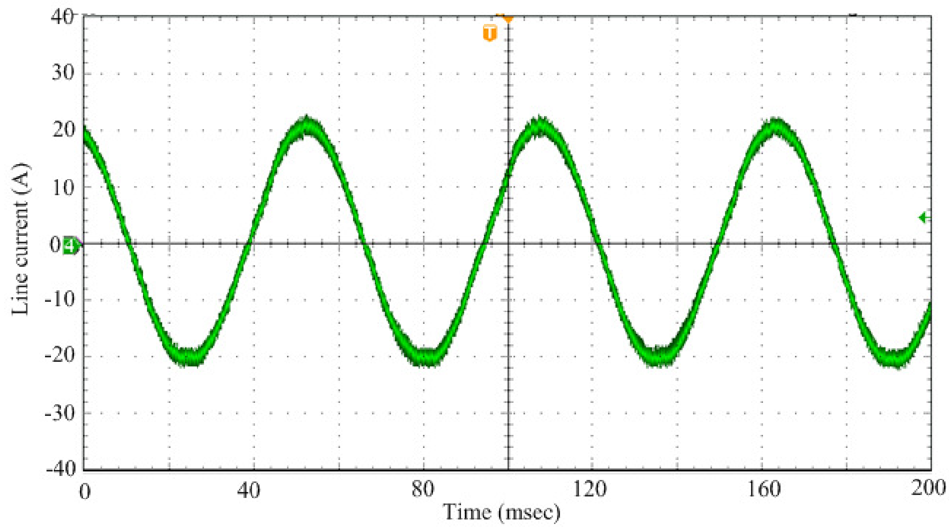

Figure 2.38: Measured Phase A current of SynRM at full load (6.5 Nm).

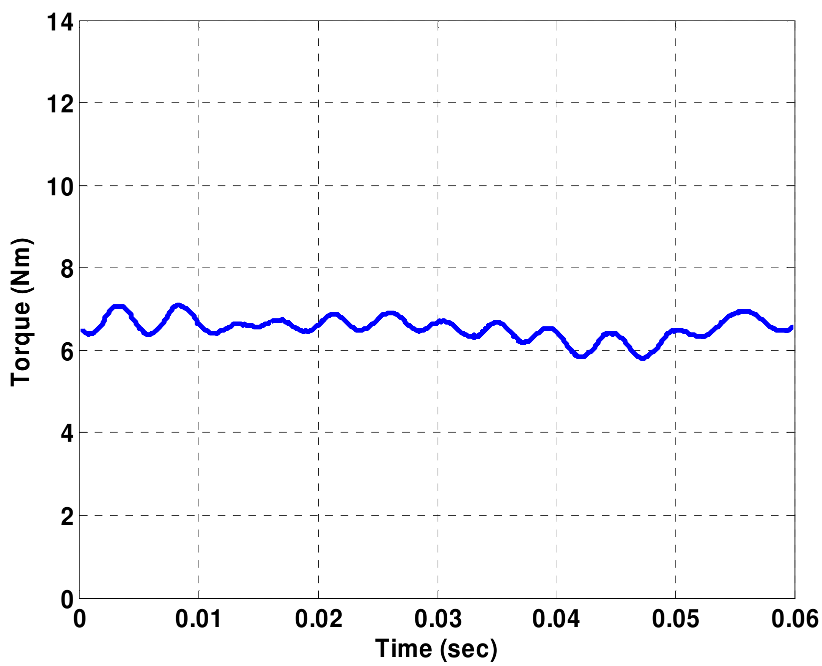

Figure 2.39: Measured Torque of SynRM at full load and 600rpm.

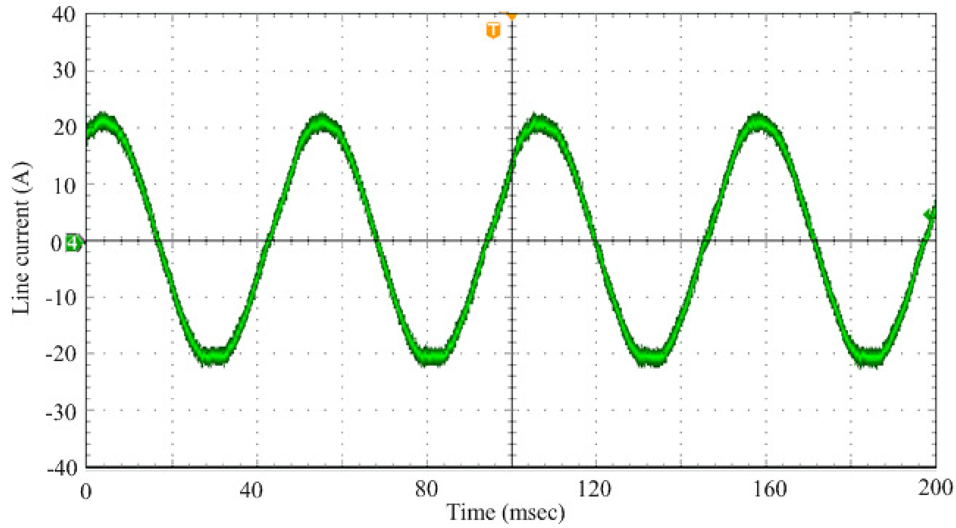

Figure 2.40: Measured Phase A current of IPM motor at full load (10.0 Nm).

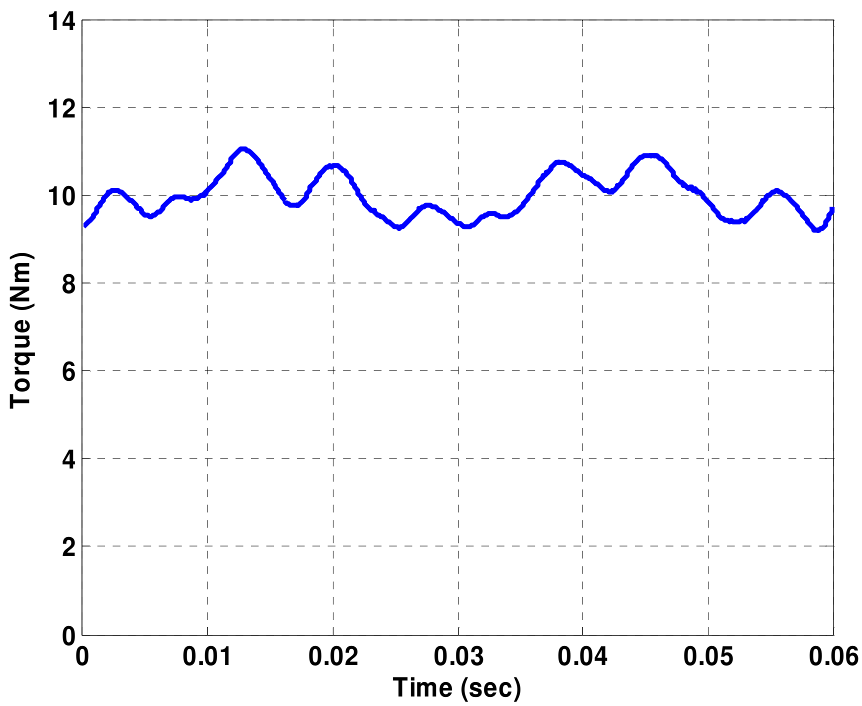

Figure 2.41: Measured Torque of IPM motor at full load and 600rpm.

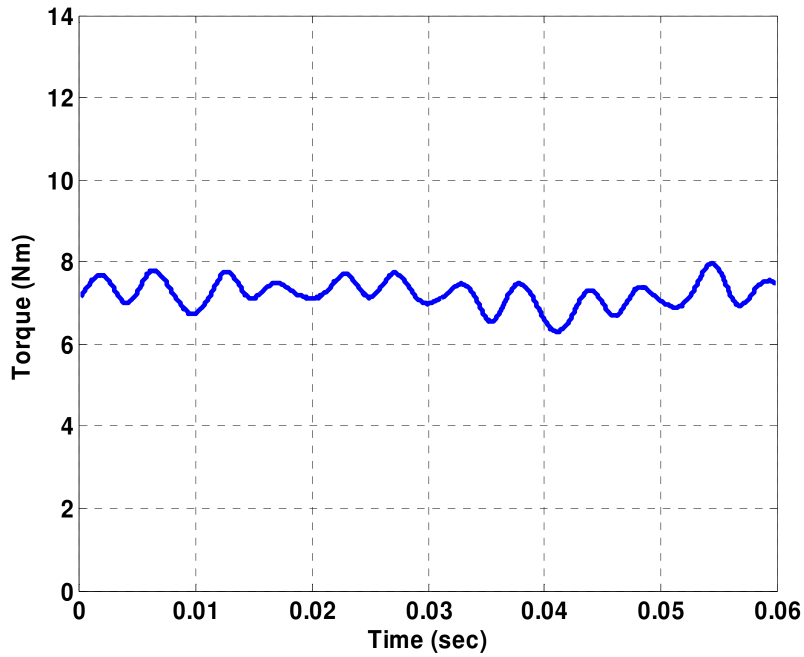

Figure 2.42: Measured Torque of IPM motor without reluctance torque (i_d=0) and with phase current 20A (peak).

2.6 Conclusion

In this chapter, a synchronous reluctance machine and an interior permanent magnet machine sharing a common stator are designed. The machine size, stator slot number, rotor pole number, rotor structure and etc. are discussed to maximize the performance of the prototype machines. Finite element analysis in ANSYS/Maxwell and experimental results are provided to compare the performance of the prototype machines.

3. GEOMETRY OPTIMIZATION OF IPM MACHINES USING ORTHOGONAL EXPERIMENTAL DESIGN METHOD AND ARTIFICIAL NEURAL NETWORK

3.1 Introduction

Interior permanent magnet (IPM) machines are widely used in various industrial applications. They have high torque density as a result of taking advantage of both magnetic torque produced by permanent magnets and reluctance torque due to unequal reluctances of the *d* and *q* axes. IPM machines also enjoy an extended flux-weakening region because of their reluctance torque and ruggedness of the rotor.

Although there are many merits of IPM machines, high torque pulsation is their major drawback [77]-[79], manifesting in excessive noises and mechanical vibrations. There are mainly three sources of torque pulsations. One is the non-ideal magnetic field distribution in the air gap, resulting in harmonic components in each phase flux linkage. This will induce a phase back-EMF with harmonics [80]. When the IPM machine is supplied with sinusoidal currents, torque with significant pulsations is produced. Another source of torque pulsation arises from reluctance variation in the magnetic circuit when the rotor is rotating. This will generate a varying inductance difference L_d-L_q, and pulsating reluctance torque thereafter. Besides, cogging effect is also an origin of torque pulsation in IPM machines.

Fundamentally, there are two methods of reducing torque ripple in IPM motors. One is from the motor design consideration. By designing IPM motors in a proper way, torque pulsation can be minimized. Listed below is some previous research work: Various winding distributions were studied to reduce torque pulsations [80]-[82]. Rotor geometry optimization is also an important aspect in designing an IPM machine. A. Kioumarsi [83] reported a suppressed torque pulsation in IPM machine by drilling small holes in the rotor. Z. Q. Zhu [84] analyzed the effect of rotor pole-arc to pole-pitch ratio

---

This chapter previously appeared as: L. Guo and L. Parsa, "Geometry optimization of IPM machines using orthogonal experimental design method and artificial neural network," *J. of Electromagn. Waves and Appl.*, vol. 25, pp. 901-912, Apr. 2012.

on IPM machine's cogging torque. The other method of reducing torque ripple is to supply some customized currents into the IPM motor instead of sinusoidal currents. Chapter 4 of this dissertation will discuss this method in detail.

Due to the highly nonlinear magnetic behavior, it is impossible to conduct an accurate analytical calculation to estimate the machine performance. Numerical techniques, e.g., FEA are widely used in the design of IPM machines. In refining the rotor geometry, one intuitive and commonly used method is the "One Factor At a Time" (OFAT) method. Although not mentioned, Z. Q. Zhu [84] and Peyman Niazi [85] were optimizing rotor geometry utilizing the OFAT method. IPM machine rotor optimization methods based on genetic algorithms were also reported [86], [87].

In this work, OED method is proposed to provide more flexibility and robustness in optimizing rotor geometry which will ultimately lead to a potential reduction in torque pulsation with the aid of an artificial neural network (ANN).

3.2 The IPM machine under study

A 3-phase, 9-slot, 6-pole IPM machine shown in Figure 3.1 is considered in this study. Figure 3.2 shows part of the rotor with the geometry parameters which are to be optimized. The permanent magnets used are NdFeB. The parameters of the IPM machine are included in Table 3.1.

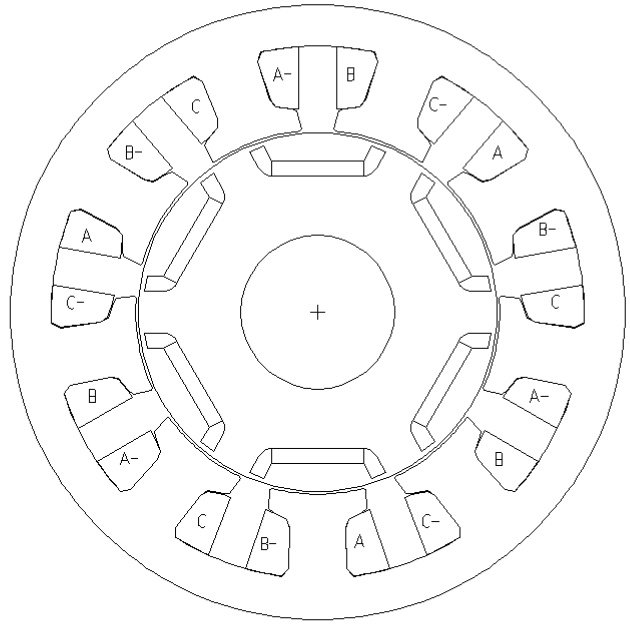

Figure 3.1: Cross section of the IPM machine under study.

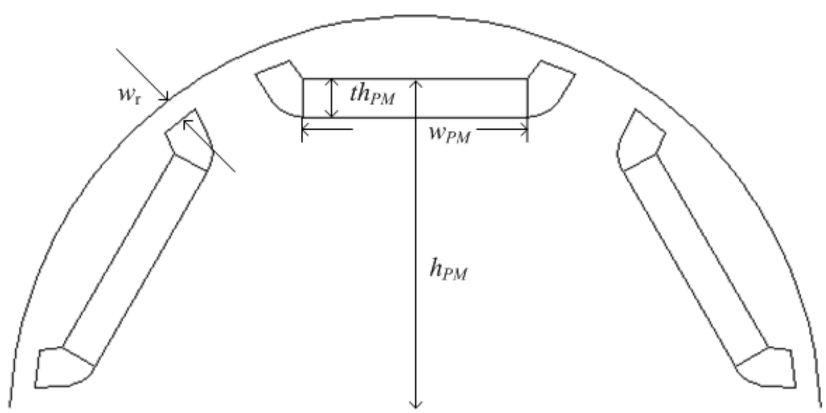

Figure 3.2: Rotor design parameters of the IPM machine.

Table 3.1: Parameters of the IPM machine.

Rated Speed	1800 rpm
Supply Frequency	60 Hz
Stator Outer Diameter	120 mm
Stator Inner Diameter	71.2 mm
Airgap Length	0.5 mm
Stack Length	100 mm
PM Mag. Retentivity	1.1 Tesla

Ansoft Maxwell 2D software package is capable of computing magnetic field distribution once necessary boundary conditions are specified. Previous research efforts have proven that FEA programs provide very accurate results, though sometimes it requires significant computation time.

OFAT design method is widely used in rotor design optimizations. Only one of the design parameters is swept at a time, where other parameters are held unchanged. The aim of the design process is to find the optimum parameter set with which the IPM machine has the best performance. There is no general method through which an optimal design will be reached for a specific requirement, except varying the parameter step by step.

The OFAT design method is valid only when all the design parameters are fully decoupled. In the case of an IPM machine design, which is a highly nonlinear electromechanical system, the machine performance is affected by all the parameters and the interactions between them. OFAT design method does not consider this effect. In order to obtain a global optimal design, a procedure which considers all the parameters simultaneously needs to be developed.

3.3 Orthogonal experimental design

In many research fields, the orthogonal experimental design method is widely used in determining the optimal parameter values. Computer simulation based on FEA works as “experiments” here. When it comes to evaluating the effects of several parameters on system output (in this work, IPM machine torque pulsation), a comprehensive experimental design method is often adopted. It means conducting a comprehensive series of experiments which cover the entire feasible domain of all design parameters. This design method is ineffective because the number of experiments will be evidently too large to implement when there are several design parameters.

Instead of conducting a comprehensive experimental design, which is neither necessary nor efficient, OED method can be used as a systematic method in performing computer simulations and efficiently provides sufficient system information for further use. One of the most distinct advantages of the OED optimization method is the significant reduction in the number of experiments. A simple and intuitive comparison of comprehensive experimental design and OED is shown in Figure 3.3. This experimental design is for a system which possesses three parameters: A, B, and C. For each parameter, there are three different values to choose from. In Figure 3.3, three design parameters are mapped into three-dimensional Cartesian coordinates, each of which has three values. Each experiment is represented as a solid dot here. It can be seen from Figure 3.3 (a) that 27 experiments are needed when using comprehensive experimental design, whereas, the number of experiments is only 9, when OED optimization method is adopted, as shown in Figure 3.3 (b). There is much greater difference in the total numbers of experiments if there are more design parameters or there are more values for each parameter to choose from.

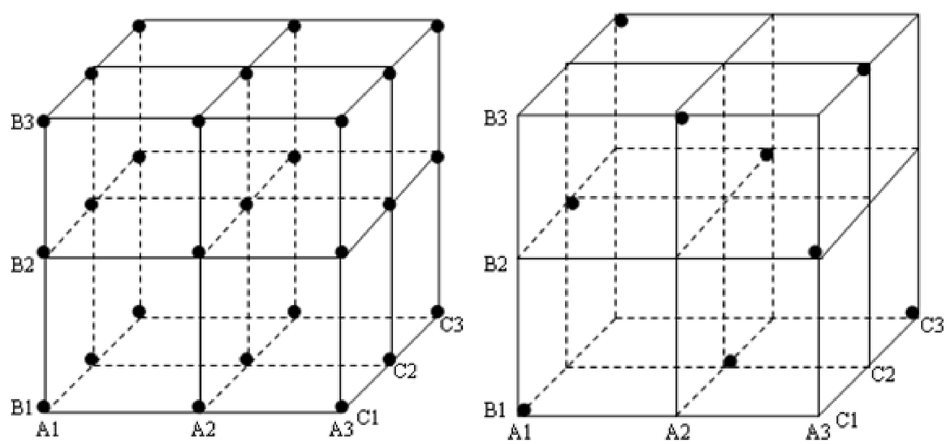

Figure 3.3: Comparison of (a) "comprehensive experimental design" and (b) "orthogonal experimental design".

OED method takes advantage of a matrix, known as orthogonal array. Each row of the matrix represents the parameter values in each combination and the number of rows reveals the number of experiments that are expected in a specific design. Each column of the orthogonal array represents a parameter, and the number of columns is the same as the number of design parameters. Orthogonal arrays are often presented as shown in Figure 3.4. In Table 3.2, an L_9 (3^3) orthogonal array which can be used in experimental design of the aforementioned three-parameter system is introduced as an example. In the orthogonal array, "1, 2, 3" indicate the values of each parameter. The arrangement for each parameter is also shown in this table. It can be seen that each column has an equal number of "1"s, "2"s, and "3"s. The array is orthogonal only if in any two columns (e.g. column A and column B), the nine pairs, (A1,B1), (A1,B2), (A1,B3), (A2,B1), (A2,B2), (A2,B3), (A3,B1), (A3,B1), (A3,B1), appear the same number of times. Generally, an orthogonal array used for an experimental design is not unique and several different arrangements might be possible. The total number of experiments (N) is determined by the following equation:

$$N = m^2 \tag{3.1}$$

where, m is the maximum number of values of each parameter. In the case illustrated in Table 3.2, a total number of 9 experiments are expected.

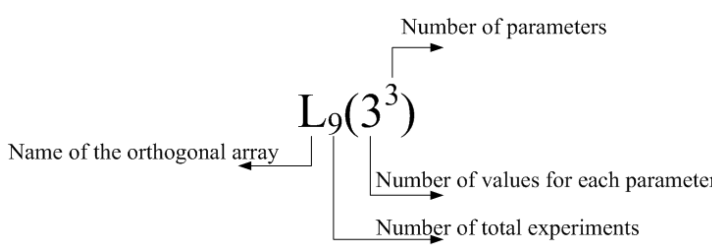

Figure 3.4: Common description of "orthogonal array".

Table 3.2: Orthogonal Array of $L_9(3^3)$.

Experiments	Controlling Factors			System Response
	A	B	C	y
1	A1	B1	C1	y1
2	A1	B2	C2	y2
3	A1	B3	C3	y3
4	A2	B1	C2	y4
5	A2	B2	C3	y5
6	A2	B3	C1	y6
7	A3	B1	C3	y7
8	A3	B2	C1	y8
9	A3	B3	C2	y9

Once all design parameters have been decided, the OED method is simple and straightforward. General steps to conduct orthogonal experimental design are outlined below:

(1) Decide the number of design parameters to be taken into account in a specific experimental design.

(2) Decide how many values each parameter will carry.

(3) Generate the orthogonal array based on the knowledge of design parameters.

(4) Implement FEA computer simulations to obtain system outputs.

(5) Model the system using ANN and find the optimal design.

The OED method is applied to the IPM machine under study. As shown in Figure 3.2, four major rotor parameters are defined. w_r is the magnetic rib width in the rotor. w_{PM} and th_{PM} are the width and thickness of permanent magnets. h_{PM} is the distance from the rotor center to top of each permanent magnet. The aim of this design is to find the optimal rotor geometry with which the IPM machine has the minimum torque pulsation. As a result, torque pulsation level is selected as the system output. The design domains for all the four parameters are listed in Table 3.3. Considering five values for each parameter, an $L_{25}(5^4)$ orthogonal array is designed and finite element analysis is carried out, as shown in Table 3.4.

Table 3.3: Values of rotor design parameters.

Design Parameters	Values of design parameters				
w_r (mm)	3	2.5	2	1.5	1
w_{PM}(mm)	17.8	18.6	19.4	20.2	21
th_{PM}(mm)	2.4	2.7	3	3.3	3.6
h_{PM}(mm)	27.2	27.8	28.4	29	29.6

Table 3.4: Orthogonal array and simulation results.

Experiments	w_r	h_{PM}	th_{PM}	w_{PM}	Pulsation (%)
1	3	27.2	2.4	17.8	42.49%
2	3	27.8	2.7	18.6	40.84%
3	3	28.4	3	19.4	35.95%
4	3	29	3.3	20.2	26.50%
5	3	29.6	3.6	21	15.90%
6	2.5	27.2	3	21	14.45%
7	2.5	27.8	3.3	17.8	41.28%
8	2.5	28.4	3.6	18.6	41.11%
9	2.5	29	2.4	19.4	45.29%
10	2.5	29.6	2.7	20.2	36.70%
11	2	27.2	3.6	20.2	17.92%
12	2	27.8	2.4	21	26.06%
13	2	28.4	2.7	17.8	58.18%
14	2	29	3	18.6	57.15%
15	2	29.6	3.3	19.4	46.03%
16	1.5	27.2	2.7	19.4	28.75%
17	1.5	27.8	3	20.2	30.52%
18	1.5	28.4	3.3	21	32.80%
19	1.5	29	3.6	17.8	61.50%
20	1.5	29.6	2.4	18.6	64.82%
21	1	27.2	3.3	18.6	37.51%
22	1	27.8	3.6	19.4	34.97%
23	1	28.4	2.4	20.2	48.29%
24	1	29	2.7	21	42.17%
25	1	29.6	3	17.8	75.76%

3.4 Design optimization using artificial neural network

Computer simulations based on OED method provide sufficient information with much fewer data points, but the optimal rotor design cannot be found directly from these data points. This is because only a few sparse points in the entire design domain are available and there is a big chance that the optimal point is not included. In addition to this, there are only a few discrete data points from FEA. To find the global optimal rotor design, values of each parameter need to be swept continuously. A mathematical model which can predict torque pulsations for different rotor geometry parameters is required. Because of the highly nonlinear characteristics of magnetic materials, it is not easy to fit the sparse data points using simple mathematical equations. In this study, an artificial neural network model is designed to support the optimization process, by performing complex functions which cannot be easily described by explicit mathematical equations.

Based on the datasets obtained by the computer simulations with various rotor parameters, a feedforward back propagation network has been designed and trained to give better performance for the IPM machine optimization. Neural Network Toolbox in Matlab is used to provide the 3-layer ANN model and training algorithms. The configuration of the ANN model is shown in Figure 3.5. It consists of four inputs representing four selected rotor geometry parameters, two hidden layers which have 15 neurons respectively, and the output layer. Neurons in one layer are connected with all other neurons with different weights, which are to be calculated by iterations in the training process.

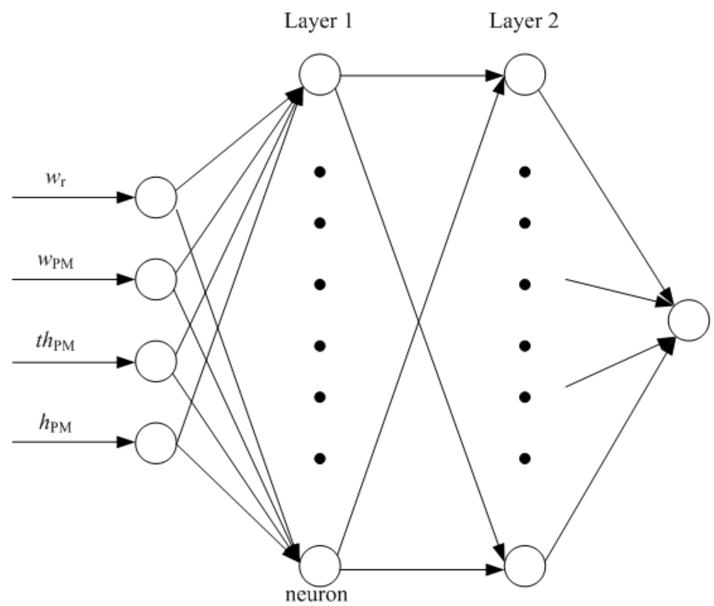

Figure 3.5: Configuration of the 3-layer Common description of "orthogonal array".

The 25 datasets from FEA are used to train the ANN model. OED covers as much information as possible with limited datasets, which helps the training process and provides more accurate estimation. After the ANN model is properly trained, an implicit function representing the IPM machine torque pulsation with the rotor parameters is created, as shown in (3.2).

$$Ripple = f(w_r, w_{PM}, th_{PM}, h_{PM}) \tag{3.2}$$

A continuous search for the optimal parameter set can be easily implemented. The optimal rotor parameters are: magnetic rib width w_r = 3.2mm, permanent magnet width w_{PM} = 21.5mm, permanent magnet thickness th_{PM} = 3.5mm, and h_{PM} = 29.6mm. This design is evaluated by FEA, showing the torque pulsation to be 10.7%, which is much lower that the values in Table 3.4.

3.5 Conclusion

In this chapter, a systematic geometry design method for IPM machines is proposed to reduce torque pulsation. FEA based computer simulation is capable of providing sufficient accuracy in the analysis of IPM machines, but it is time consuming and inefficient. OED method is proposed to reduce the number of FEA datasets without losing much information. In the optimization process, an ANN model is designed and trained using the FEA datasets to find the optimal results. The resultant torque pulsation level is comparatively low compared to that before optimization.

4. CURRENT PROFILING TECHNIQUE OF MINIMIZING TORQUE RIPPLE IN PERMANNET MAGNET MOTORS

4.1 Introduction

IPM motors with modular stators further improves the performance and reduces the manufacturing cost [77], [78]. The modular stator is designed by segmenting the stator into several identical modules. The modular IPM motors feature high robustness and inherent fault tolerant capability. These characteristics are essentially required in some safety critical applications.

However, high torque ripple is the major drawback of most IPM motors. As is discussed in chapter 3, there are several sources of torque ripple for IPM motors. They are simply summarized here again: distorted back-EMF waveform, varying d and q axes inductances and cogging effect. In order to minimize the torque ripple, a universal current profiling technique is proposed, which can take any source into consideration and successfully minimize the torque ripple.

Section 2 of this chapter presents the mathematical models of the modular IPM motors. Their performance is compared by FEA. In section 3, several sources of torque ripple are studied, such as the harmonic components of back-EMF, inductance variations and cogging effects. The universal current profiling technique which can minimize the torque ripple is derived in section 4. Finally, the proposed technique is applied to the IPM motor and FEA shows that the torque ripple is significantly reduced.

4.2 Analysis of modular IPM motor

Two 3-phase, 6-slot, 4-pole modular IPM motors are considered in this study, as shown in Figure 4.1 and Figure 4.2. Motor I has a single permanent magnet for one pole, and Motor II has two separate magnets in "V" shape for one pole. The motor consists of

---

This chapter previously appeared as: L. Guo and L. Parsa, "Torque ripple reduction of the modular Interior Permanent Magnet machines using optimum current profiling technique," *IEEE Int. Electric Machines and Drives Conf.,* pp. 1094-1099, May 2009.

six identical stator modules with two modules for each phase. The parameters of the modular motors are shown in Table 4.1.

The performance of these motors is compared using FEA, with the results shown in Table 4.2. It can be seen that Motor II makes better use of the permanent magnet material. It produces similar output torque as Motor I with only 75% of the magnets used.

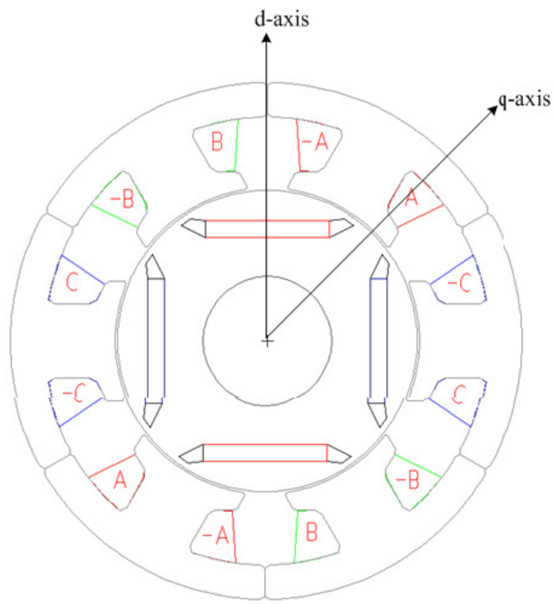

Figure 4.1: Cross section of Motor I.

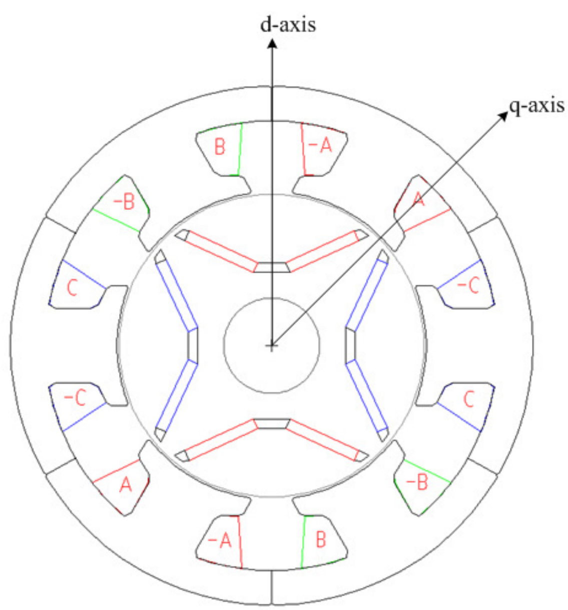

Figure 4.2: Cross section of Motor II.

Table 4.1: Parameters of the motor under study.

Rated Current	10.6 A
Rated Speed	1800 rpm
Supply Frequency	60 Hz
Stator Outer Diameter	120 mm
Stator Inner Diameter	71.2 mm
Number of Turns Per Phase	40
Airgap Length	0.5 mm
Stack Length	100 mm
PM Mag. Retentivity	1.1 Tesla

Table 4.2: Performance comparison of Motor I and Motor II.

	Motor I	Motor II
Phase Currents	10.6A	10.6A
Output Torque	8Nm	8Nm
Use of Magnets	11600mm^3	8650mm^3

The *d* and *q* axes are shown in Figure 4.1 and Figure 4.2. The buried permanent magnets inside the rotor produce necessary saliency in the IPM motor. The *d*-axis flux passes through both the magnets and magnet pocket area in each pole, which act as a large flux barrier. The q-axis flux only passes through steel laminations in the rotor. Therefore, the *d*-axis inductance is smaller than the *q*-axis inductance, and this will produce reluctance torque if correct current vector is applied.

In the *d*-*q* reference frame, the torque equations are expressed as [88]:

$$T = \frac{3}{2} P_n \lambda_m i_q + \frac{3}{2} P_n (L_d - L_q) i_d i_q \tag{4.1}$$

The total torque consists of two parts. The first term in the right hand side of (4.1) is the magnetic torque and the second term is the reluctance torque.

At time zero (t = 0), the magnetic axis of phase-A is aligned with the rotor *d*-axis and the back-EMF is aligned with the *q*-axis. The phase angle of phase-A current φ is also the electrical angle between the stator rotating MMF and the rotor *d*-axis. Figure 4.3 shows the vector diagram of IPM motors in steady state operation, where γ is the torque angle.

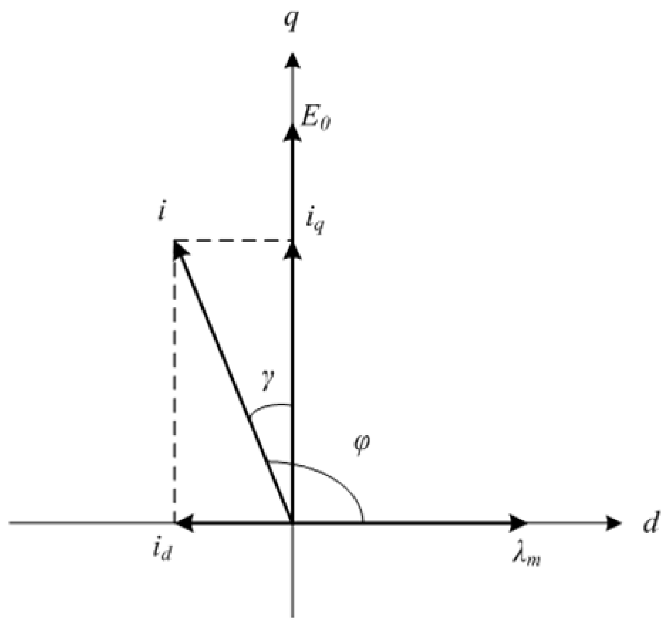

Figure 4.3: Vector diagram of steady state operation.

4.3 Analysis of the torque ripple sources

4.3.1 The distorted permanent magnet flux linkage

Normally it is assumed that the back-EMF waveform is sinusoidal. However, due to the shape of the magnets in the rotor and the stator winding distributions, the actual back-EMF is not ideal sinusoidal waveform. The distorted permanent magnet flux linkage is one of the major causes of torque ripples in IPM motors. This will be reflected to phase back-EMF waveforms with harmonic components. Figure 4.4 shows the back-EMF waveforms of Motor II in the *abc* reference frame and Figure 4.5 shows the frequency spectrum. As is discussed in [84], the permanent magnet flux in the *d*-*q* reference frame is not constant but with pulsations. The *d*-*q* model for IPM motor torque is expressed as in (4.1). The pulsations of λ_m result in output torque ripple.

The IPM motors feature hybrid torque producing mechanism. The total torque consists of both reluctance torque and magnetic torque. As is discussed in the introduction section, they also have various sources of torque ripple. Different IPM motors may have different dominant source of torque ripple. In the following, Motor II is taken as an example to illustrate the effects of L_d, L_q variations and the cogging effect.

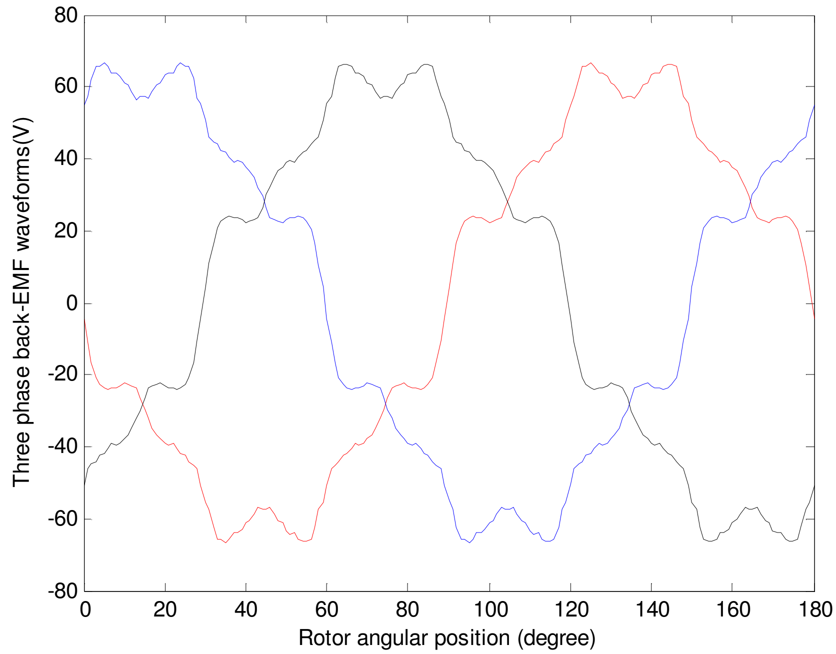

Figure 4.4: Three phase back-EMF waveforms of Motor II.

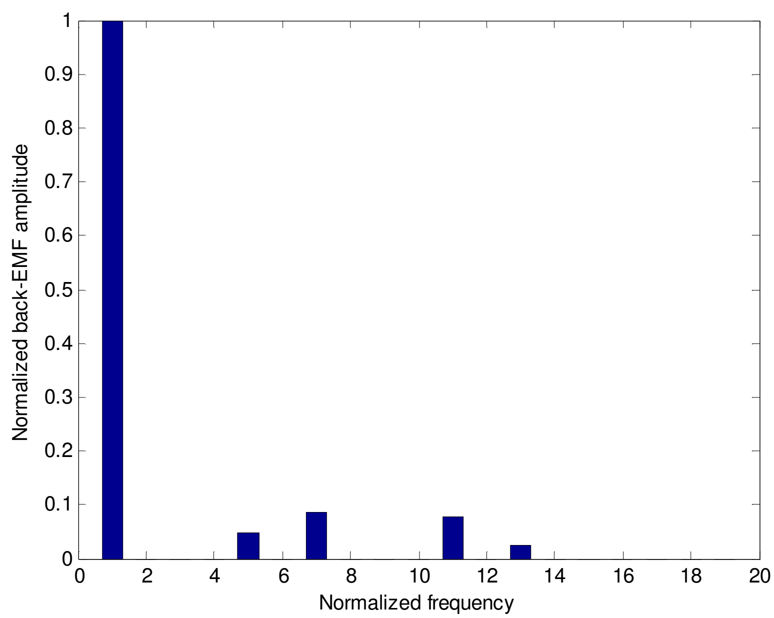

Figure 4.5: Frequency spectrum of the phase back-EMF waveforms of Motor II.

4.3.2 Saturation and variation of L_d and L_q

It is well known that the inductances of permanent magnet motors will reduce as a result of saturation [89]. Figure 4.6 shows the simulated *d* and *q*-axis inductances of

Motor II. The L_d saturation effect is analyzed by setting the q-axis current to be zero. The d-axis current is increased step by step, and the flux linkages can be obtained by the FEA. In the same way, the L_q saturation effect can be analyzed by stepping i_q while keeping i_d to be zero. Equation (4.2) and (4.3) are used to estimate the L_d and L_q, where λ_d and λ_q are the d and q-axis total flux linkages, respectively. It can be seen from Figure 4.6 that the iron saturation reduces the airgap flux density, causing the reduction of inductances.

$$\lambda_d = \lambda_m + L_d i_d \tag{4.2}$$

$$\lambda_q = L_q i_q \tag{4.3}$$

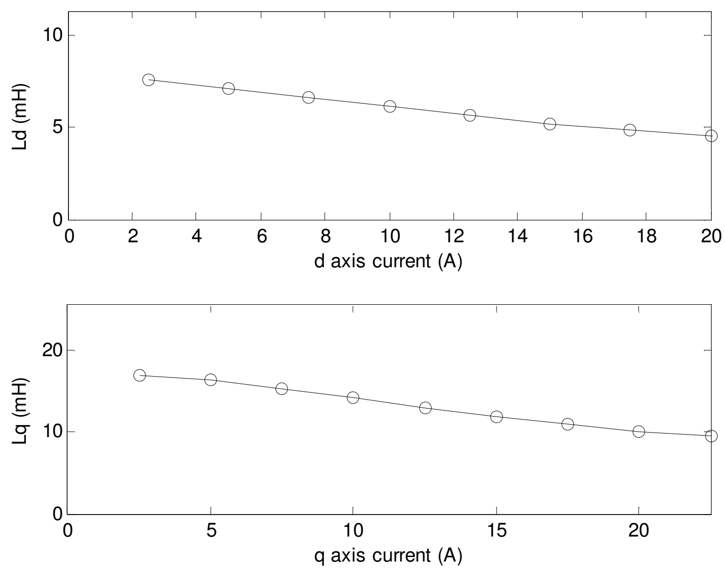

Figure 4.6: Saturation effects of both L_d and L_q in Motor II.

The modular IPM motor has a simple structure. There are only six slots in this design. The path for magnetic fluxes may change significantly when the d-axis rotates from facing stator teeth to facing slot openings. Therefore, the inductances vary a lot when the rotor is at different angular positions. Figure 4.7 shows the variations of the inductances with respect to rotor position. It can be seen that the pulsating of L_d and L_q will result in pulsating L_d-L_q. From the d-q reference frame torque equation as in (4.1), the reluctance torque will contain a pulsating component.

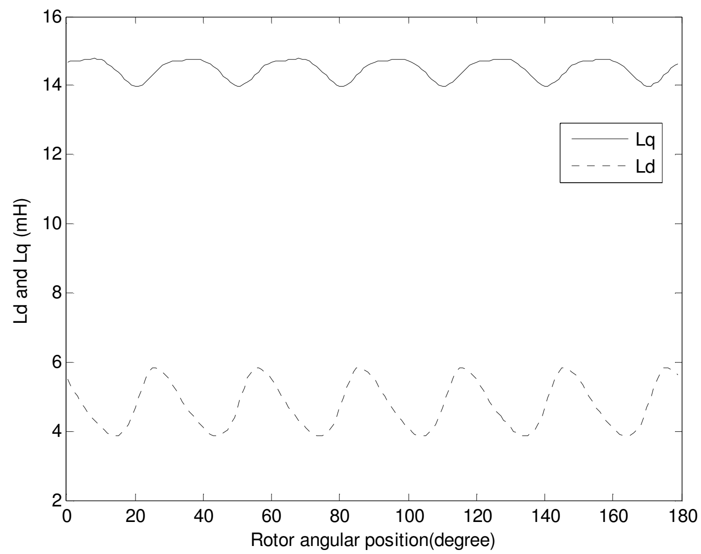

Figure 4.7: Inductance variation with respect to rotor position in Motor II.

4.3.3 The cogging torque

The cogging effect is another important source of torque ripple in IPM motors [90]. It comes from the interaction between the permanent magnets in the rotor and the stator slots. This is caused by uneven airgap reluctance resulting in the magnets constantly seeking a position of minimum reluctance. Figure 4.8 shows the cogging torque of Motor I and Motor II. Cogging torque of Motor II is much higher than that of Motor I.

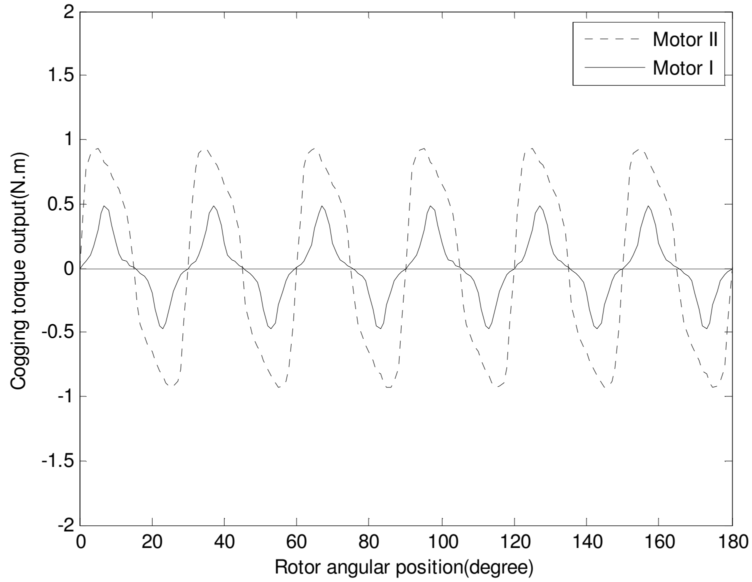

Figure 4.8: Cogging torque waveforms of the IPM motors.

4.4 The universal current profiling technique

There are several sources of torque ripple in IPM motors. In Motor I, the distorted back-EMF waveform is the major cause of torque ripple, and in Motor II, the cogging torque consists of the most part of torque ripple. To minimize the torque ripple, an optimum current profiling technique is introduced in [91], but this technique only considers the back-EMF distortions in the calculation. It only works well on those IPM motors whose torque ripples mainly come from distorted permanent magnet flux linkages. Based on the classical mathematical model in *d-q* reference frame, a universal current profiling technique is derived which include the effect of not only the back-EMF harmonics but inductance variations and cogging torque into calculation. The permanent magnet flux linkage data can be obtained by either FEA or measurements. Inductance variations and cogging effect can be obtained by FEA.

By measurement, the three-phase permanent magnet flux linkage information can be calculated from the back-EMF waveforms. The back-EMF is the derivative of flux linkage [92]:

$$e = \frac{d\lambda}{dt} = \frac{d\lambda}{d\theta}\frac{d\theta}{dt} = \frac{d\lambda}{d\theta}\omega \tag{4.4}$$

where e is the instantaneous back-EMF per phase, λ is the flux linkage per phase, θ is the mechanical angular position of the rotor and ω is the angular speed. The flux linkage can be calculated by integrating the back-EMF if the motor speed is known.

In the d-q reference frame, the universal current profiling technique is derived directly from the torque equation (4.1). In order to compensate the effect of cogging torque, T_{cog} is included and (4.1) is rewritten as:

$$T = \frac{3}{2}P_n\lambda_m(t)i_q(t) + \frac{3}{2}P_n(L_d(t) - L_q(t))i_d(t)i_q(t) + T_{cog} \tag{4.5}$$

To minimize the torque ripple, the instantaneous torque T_e should be equal to the reference torque T^*:

$$T^* - T_e = T^* - \frac{3}{2}P_n\lambda_m i_q^* - \frac{3}{2}P_n(L_d - L_q)i_q^* i_d^* - T_{cog} = 0 \tag{4.6}$$

A unique solution for (4.6) can be obtained by minimizing the stator copper loss, which is:

$$P_r = (i_q^2 + i_d^2)R \tag{4.7}$$

i_d^* can be obtained from (4.7) as:

$$i_d^* = \frac{T^* - T_{cog} - \frac{3}{2}P_n\lambda_m i_q^*}{\frac{3}{2}P_n(L_d - L_q)i_q^*} \tag{4.8}$$

From (4.7) and (4.8), the copper loss P_r can be expressed in terms of q-axis current reference i_q^*:

$$P_r = \{i_q^{*2} + [\frac{T^* - T_{cog} - \frac{3}{2}P_n\lambda_m i_q^*}{\frac{3}{2}P_n(L_d - L_q)i_q^*}]^2\}R \tag{4.9}$$

To minimize the copper loss, the following should hold:

$$\frac{\partial P_r}{\partial i_q^*} = 0 \tag{4.10}$$

Equation (4.10) can be rewritten in terms of i_q^*:

$$i_q^{*4} + c i_q^* + d = 0 \tag{4.11}$$

where,

$$c = \frac{\lambda_m (T^* - T_{cog})}{\frac{3}{2} P_n (L_d - L_q)^2}, \qquad d = \frac{-(T^* - T_{cog})^2}{P_n^{\,2} (\frac{3}{2})^2 (L_d - L_q)^2} \tag{4.12}$$

The four solutions i^*_{q1}, i^*_{q2}, i^*_{q3} and i^*_{q4} for (4.11) can be derived as follows [91]:

$$i_{q1}^* = \frac{\sqrt{3G}}{12} + \frac{\sqrt{6}}{12}\sqrt{[\frac{(-F^{2/3} - 48d)\sqrt{G} - 24\sqrt{3}cF^{1/3}}{F^{1/3}\sqrt{G}}]} \tag{4.13}$$

$$i_{q2}^* = \frac{\sqrt{3G}}{12} - \frac{\sqrt{6}}{12}\sqrt{[\frac{(-F^{2/3} - 48d)\sqrt{G} - 24\sqrt{3}cF^{1/3}}{F^{1/3}\sqrt{G}}]} \tag{4.14}$$

$$i_{q3}^* = -\frac{\sqrt{3G}}{12} + \frac{\sqrt{6}}{12}\sqrt{[\frac{(-F^{2/3} - 48d)\sqrt{G} + 24\sqrt{3}cF^{1/3}}{F^{1/3}\sqrt{G}}]} \tag{4.15}$$

$$i_{q4}^* = -\frac{\sqrt{3G}}{12} - \frac{\sqrt{6}}{12}\sqrt{[\frac{(-F^{2/3} - 48d)\sqrt{G} + 24\sqrt{3}cF^{1/3}}{F^{1/3}\sqrt{G}}]} \tag{4.16}$$

where,

$$F = 108c^2 + 12(-768d^3 + 81^4)^{1/2} \tag{4.17}$$

$$G = \frac{2F^{2/3} + 96d}{F^{1/3}} \tag{4.18}$$

Among the four solutions, i^*_{q1}, i^*_{q2} are complex numbers. i^*_{q3} and i^*_{q4} are real numbers where one of them is positive and the other one is negative. Therefore, based on the machine mode of operation, the right value can be selected. Once the *q*-axis current reference i_q^* is set, the *d*-axis current reference i_d^* can be easily decided by (4.8).

General steps to conduct the universal current profiling technique are outlined below:

1) Find out the torque ripple sources and evaluate the importance of each source;
2) Select one or some of the major sources to be included in the optimum current calculation;
3) Apply the current profiling technique and calculate for the optimum current profile.

4.5 FEA verification of the current profiling technique

The finite element simulations are presented to evaluate the effectiveness of the universal current profiling technique. Motor II is taken as an example. The first set of optimum currents are calculated when the cogging torque is not included. The effects of back-EMF and inductance variation will be compensated. Figure 4.9 shows the optimum current waveforms and Figure 4.10 compares the instantaneous torque waveforms under sinusoidal currents and the optimum currents. The torque ripple reduces from 42% to 34%. It can be seen that there is little improvement in the torque ripple. This is because the major source of torque ripple is cogging torque for Motor II.

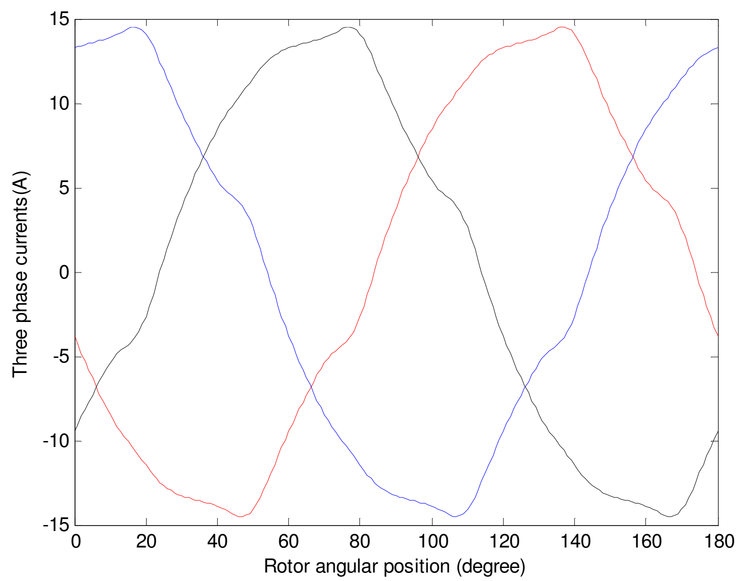

Figure 4.9: The optimum three phase currents.

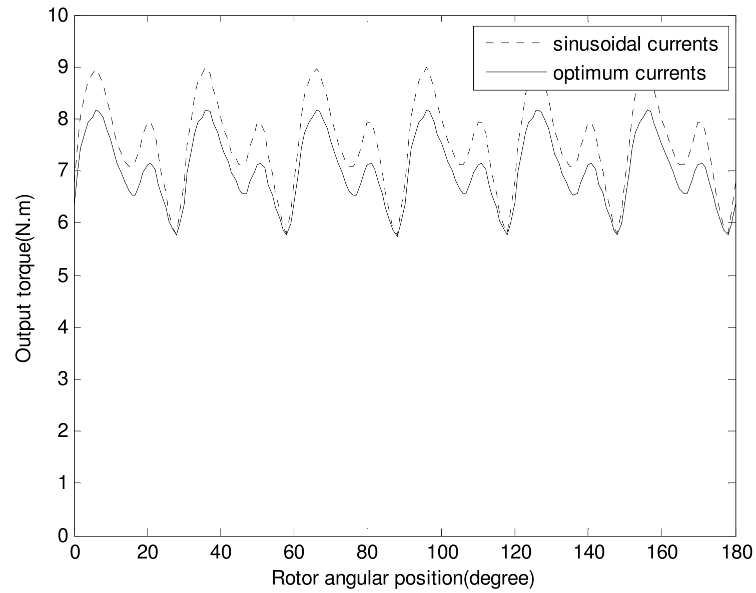

Figure 4.10: Instantaneous torque waveforms comparison.

After the cogging torque is included in the calculation, the optimum currents are shown in Figure 4.11. The instantaneous torque waveforms are compared in Figure 4.12. The torque ripple reduces from 42% to 18%.

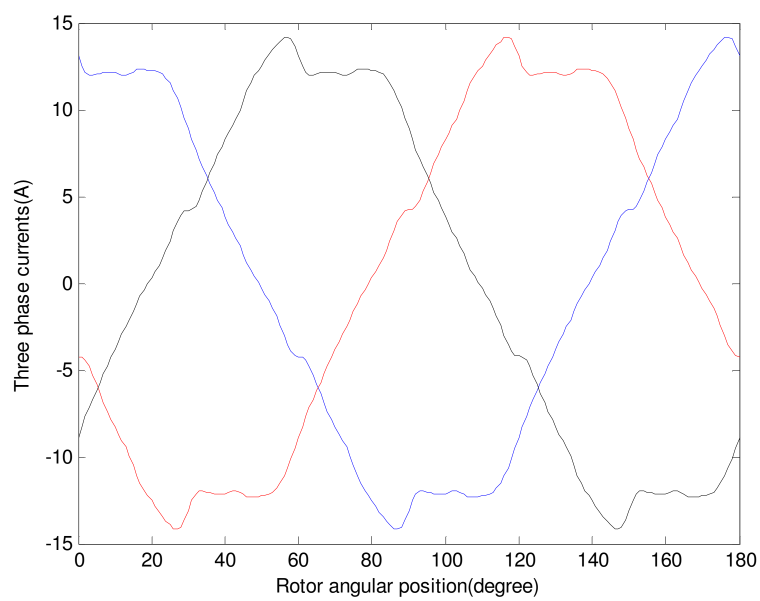

Figure 4.11: The optimum three phase currents.

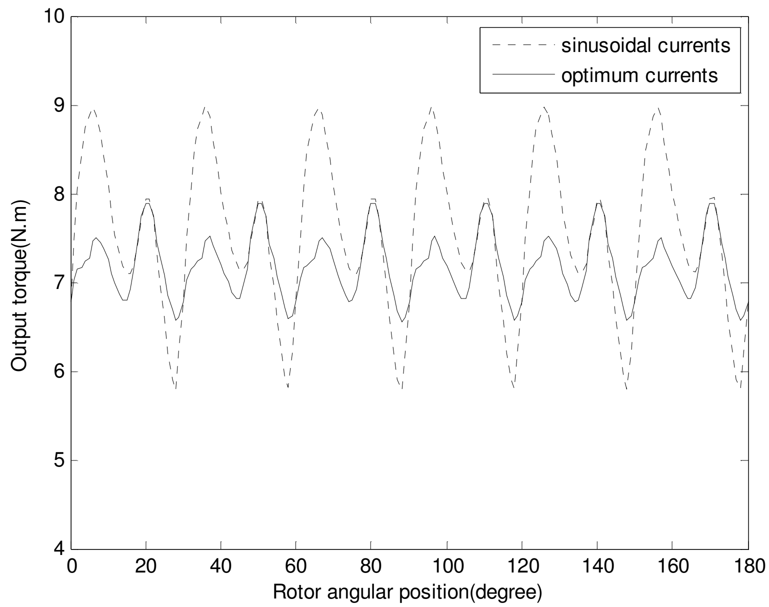

Figure 4.12: Instantaneous torque waveforms comparison.

4.6 Conclusion

In this chapter, a universal current profiling technique to reduce the torque ripple in the modular IPM motors through applying the optimum current profiles instead of three phase sinusoidal currents are presented. This technique calculates the optimum current profiles based on the torque equation in the *d-q* reference frame. Effects of not only the distorted permanent magnet flux linkages but the inductance variation and cogging torque can be included. The proposed technique was applied to a “V”-shape magnet IPM motor and the torque ripple was significantly reduced if the optimum currents were supplied.

5. MODEL REFERENCE ADAPTIVE CONTROL OF PERMANENT MAGNET MOTOR BASED ON NEURAL NETWORK

5.1 Introduction

Interior permanent magnet (IPM) motors are widely used in various applications due to many advantages such as high power density, high efficiency and low operating noise. The overall cost keeps dropping as a result of advances in permanent magnet manufacturing and technology. Much more attention has been paid to permanent magnet motors as the improvement of power electronics devices and variable speed motor controls. The output torque of IPM motors consists of both magnetic torque produced by permanent magnets and reluctance torque due to unequal reluctances between d and q axes. IPM motors can also operate at an extended speed range (flux weakening region) because of the presence of reluctance torque. At the same time, the ruggedness of the rotor also helps high speed operation mechanically, which may be a critical factor in some extremely high speed applications [93].

Multiple-phase motors have been studied for years [94]-[97]. By dividing the required power between more than three phases, the power load for a single phase becomes less. As a result, the current or voltage requirement for the converter semiconductor devices will be reduced. The total power rating of multiple-phase motor and converter can be increased significantly even though the power rating of available semiconductor devices remains unchanged. There are also other advantages of multiple-phase motors over the traditional three phase ones. Normally the torque ripple frequency is increased and the amplitude of torque ripple will be reduced, resulting in lower operating noise and mechanical vibration. By proper design, increased number of phases means better fault tolerant capability, which is important in some reliability and safety crucial applications [98]. Additional degrees of freedom also enable us to drive the motor with better performance [94], [99], which will be discussed in detail in this chapter.

This chapter previously appeared as: L. Guo and L. Parsa, "Model reference adaptive control of five-phase IPM motors based on neural network," *IEEE Trans. Ind. Electron.,* vol. 59, no. 3, pp. 1500-1508, Aug. 2012.

The relatively complex torque producing mechanism and higher possibility of saturation in the rotor iron will affect the performance of IPM motors. Therefore, high performance motor drives are needed, especially when variable speed control is applied or the load condition changes regularly.

In designing a high performance motor drive for IPM machines, a fast and stable speed controller is required, which can maintain the motor speed under various load disturbances or parameter uncertainties. Design of traditional proportional-integral (PI) or proportional-integral-derivative (PID) speed controller needs knowledge of motor models and accurate motor parameters. Moreover, fixed parameter PI or PID controllers are usually optimized to regulate the motor operating under the rated speed. The dynamic performance cannot be guaranteed in all possible speeds when the motor is required to operate in a wide speed range [100].

Various intelligent motor drive systems have been proposed and analyzed in the recent literature. In [101], The PI speed controller is tuned by a hybrid neuro-fuzzy scheme. The PI controller parameters are not fixed but optimized by a genetic algorithm at different operating conditions or system uncertainties. In order to compensate the parameter variation and external load disturbances, authors in [102] proposed to improve the conventional PI position or speed controller by adding a fuzzy neural network controller. The combined and more complex control system was said to have better performance with parameter variation. In [103], the speed controller was designed based on differential-geometric approach and linear quadratic regulator techniques. The performance has been compared with the conventional PID controllers. Similar research work such as motor drives using neural network controller or compensator [68]-[70], fuzzy logic controller [70], [71], and sliding mode controller [71], [104]-[106] have been reported.

On the other hand, the model reference adaptive system (MRAS) has received spread interests and discussion in recent years. The authors in [107] used the MRAS to estimate the speed and position of the permanent magnet motor. The neural network adaptation mechanism is used in estimating various parameters at different operating conditions. In [108], MRAS is used to estimate rotor flux, rotor and stator resistances and load torque for improving the speed control performance of an induction motor drive. In [109], both motor speed and rotor resistance are estimated by means of MRAS. Most papers are discussing the use of MRAS as estimators for various motor parameters and most of all, the motor speed [110]-[114]. At the same time, model reference adaptive scheme can also work as the controller in the closed-loop motor drive system [115]-[119]. The advantages include explicit dynamic performances and additional parameter adaptation capabilities. The novel motor drive system proposed in this work will be based on model reference adaptive control structure and a neural network primary controller will be designed as a replacement of conventional PI controllers.

In this chapter, the model reference adaptive system is introduced in section 2. The mathematical model of five-phase IPM motors is analyzed in section 3. A simple analysis of the advantages of using multiple-phase system in current control is also conducted. In section 4, necessary parameters of the custom made five-phase IPM motor are measured and evaluated. The experimental setup to verify the proposed motor drive system is also introduced. Then, in section 5, a simple MRAC design without the assistance of neural network is derived based on the mechanical equation of the IPM motor. Advantages and disadvantages of this motor drive structure are analyzed. After that, the proposed model reference adaptive control structure is designed for the speed control of the permanent magnet motor. The theoretical proof of the motor drive system is provided by analyzing the closed-loop dynamic performance. The primary controller is based on artificial neural network and used to compensate the nonlinearity of the system. The online training mechanism without knowledge of the exact nonlinear model is also introduced. Finally, computer simulations by Matlab/Simulink software package and experimental results are provided to show the advantages of the proposed motor drive.

5.2 Model reference adaptive system

In this section, model reference adaptive system is first introduced. As it is mentioned in the previous section, MRAS can be used either in system parameter identification or directly in system adaptive control [120]. In this section, system parameter identification based on model reference adaptive approach is first introduced. Then, a system control method with model reference adaptive structure is discussed.

5.2.1 Parameter identification based on model reference adaptive system

The objective of this subsection is to introduce the application of model reference adaptive system in parameter identification. Some assumptions have been made to make the analysis clear and simple. Assume the plant is a first order linear time-invariant system, which can be described by the following transfer function:

$$P(s)=\frac{Y_p(s)}{R(s)}=\frac{k_p}{s+a_p} \tag{5.1}$$

where $Y_p(s)$ and $R(s)$ are system outputs and inputs, a_p and k_p are unknown system parameters which need to be identified, and $a_p > 0$.

Choose a reference model, whose transfer function is:

$$M(s)=\frac{Y_m(s)}{U(s)}=\frac{k_m}{s+a_m} \tag{5.2}$$

where $Y_m(s)$ and $U(s)$ are reference model outputs and inputs, a_m and k_m are selected parameters which decide system dynamic performance. Normally, a_m and k_m are greater than zero.

Re-write (5.1) and (5.2) in the form of differential equations:

$$\dot{y}_p(t)=-a_p y_p(t)+k_p r(t) \tag{5.3}$$

$$\dot{y}_m(t)=-a_m y_m(t)+k_m u(t) \tag{5.4}$$

where $r(t)$ is the reference input. The objective is to identify the plant model parameters a_p and k_p. The control signal $u(t)$ will be generated by measuring plant input $r(t)$ and output $y_p(t)$ such that reference model output $y_m(t)$ will track the plant output $y_p(t)$ closely. Figure 5.1 shows a model reference adaptive parameter identification system. The reference model input $u(t)$ is:

$$u(t)=a_0(t)r(t)+b_0(t)y_p(t) \tag{5.5}$$

where $a_0(t)$ and $b_0(t)$ are adjustable parameters. Substitute (5.5) into (5.4),

$$\dot{y}_m(t)=-a_m y_m(t)+k_m a_0(t)r(t)+k_m b_0(t)y_p(t) \tag{5.6}$$

Define

$$e_1(t)=y_m(t)-y_p(t) \tag{5.7}$$

and take the first derivative of both sides of (5.7):

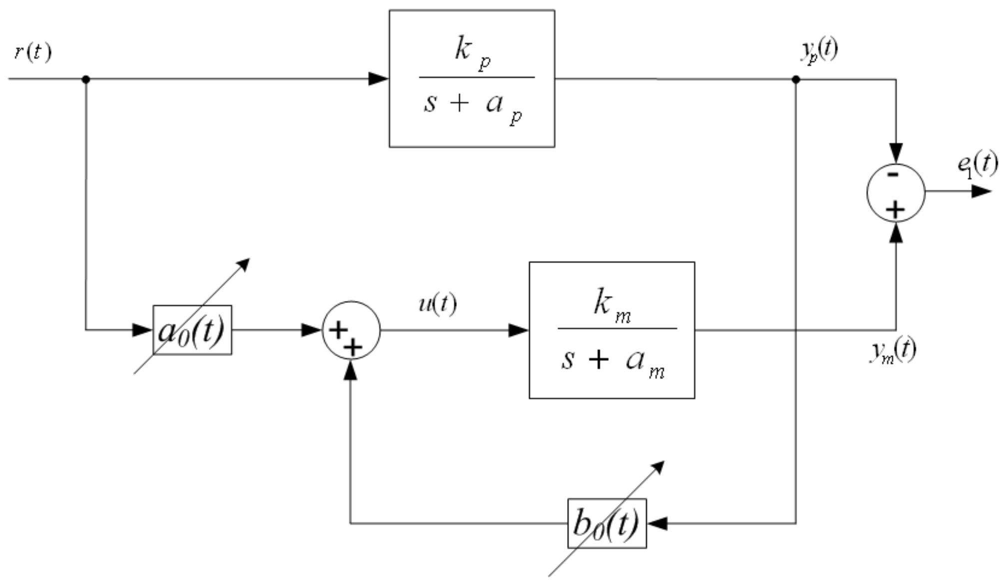

Figure 5.1: Structure of a model reference adaptive parameter identification system.

$$\begin{aligned}\dot{e}_1(t) &= \dot{y}_m(t) - \dot{y}_p(t)\\ &= -a_m y_m(t) + k_m a_0(t) r(t) + k_m b_0(t) y_p(t) + a_p y_p(t) - k_p r(t) + a_m y_p(t) - a_m y_p(t)\\ &= -a_m e_1(t) + k_m\{[a_0(t) - \frac{k_p}{k_m}]r(t) + [b_0(t) - \frac{a_m - a_p}{k_m}]y_p(t)\}\end{aligned} \tag{5.8}$$

If define

$$a_0^* = \frac{k_p}{k_m}, \qquad b_0^* = \frac{a_m - a_p}{k_m} \tag{5.9}$$

the error signal $e_1(t)$ can be expressed as:

$$\begin{aligned}\dot{e}_1(t) &= -a_m e_1(t) + k_m\{[a_0(t) - a_0^*]r(t) + [b_0(t) - b_0^*]y_p(t)\}\\ &= -a_m e_1(t) + k_m[\theta(t) - \theta^*]^T \xi(t)\end{aligned} \tag{5.10}$$

where

$$\theta(t) = \begin{bmatrix} a_0(t) \\ b_0(t) \end{bmatrix} \quad \theta^* = \begin{bmatrix} a_0^* \\ b_0^* \end{bmatrix} \quad \xi(t) = \begin{bmatrix} r(t) \\ y_p(t) \end{bmatrix} \tag{5.11}$$

Define parameter error as:

$$\phi(t) = \theta(t) - \theta^* = \begin{bmatrix} a_0(t) - a_0^* \\ b_0(t) - b_0^* \end{bmatrix} \tag{5.12}$$

The system error can be expressed as:

$$\dot{e}_1(t) = -a_m e_1(t) + k_m \phi(t)^T \xi(t) \tag{5.13}$$

This is a nonlinear differential equation, whose stability can be analyzed by Lyapunov theory. Choose a positive definite Lyapunov function as:

$$V(e_1, \phi) = \frac{1}{2} e_1^2(t) + \frac{k_m}{2} \phi^T(t)\phi(t) > 0 \tag{5.14}$$

Take the first derivative of V over time:

$$\begin{aligned} \dot{V}(e_1, \phi) &= e_1(t)\dot{e}_1(t) + k_m \phi(t)^T \dot{\theta}(t) \\ &= -a_m e_1^2(t) + k_m e_1(t)\phi(t)^T \xi(t) + k_m \phi(t)^T \dot{\theta}(t) \end{aligned} \tag{5.15}$$

If select the adaptation law of θ as:

$$\dot{\theta}(t) = -e_1(t)\xi(t) \tag{5.16}$$

and substitute (5.16) into (5.15),

$$\dot{V}(e_1, \phi) = -a_m e_1^2(t) \tag{5.17}$$

which is negative semi-definite. According to Lyapunov theory, the original system is stable in the sense of Lyapunov at the equilibrium point of $e_1(t) = 0$. In terms of $a_0(t)$ and $b_0(t)$, the adaptation law can be summarized as:

$$\begin{aligned} \dot{a}_0(t) &= -e_1(t)r(t) \\ \dot{b}_0(t) &= -e_1(t)y_p(t) \end{aligned} \tag{5.18}$$

Including the adaptation law, the structure of this model reference adaptive parameter identification is shown in Figure 5.2. γ_1 and γ_2 are gains in the adaptive loop. Sometimes, a proportional gain is added before the integrator to accelerate the adaptation process. The parameters of proportional gain and integrator can be obtained by experiments.

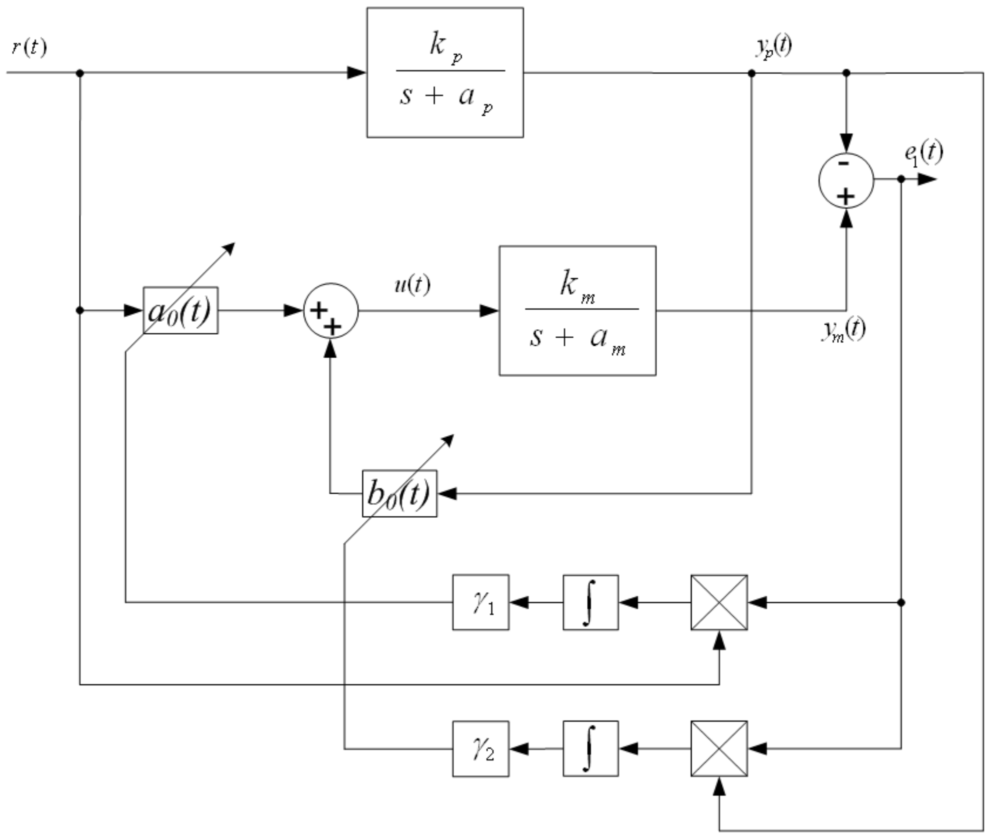

Figure 5.2: Structure of the model reference adaptive parameter identification with the adaptation law.

If it is difficult to adjust parameters a_0 and b_0, an alternative way to conduct this adaptive law is to generate additional control signals, as shown in Figure 5.3. a_0^* and b_0^* are feedforward and feedback loops. In normal operating conditions, plant output and reference model output are the same due to the presence of these two loops, which means $y_p(t) = y_m(t)$ and $e_1(t) = 0$. If the plant parameters change, the adaptation loop will work to generate appropriate control signals to adjust $u(t)$, such that the reference model output $y_m(t)$ goes back to the plant output $y_p(t)$.

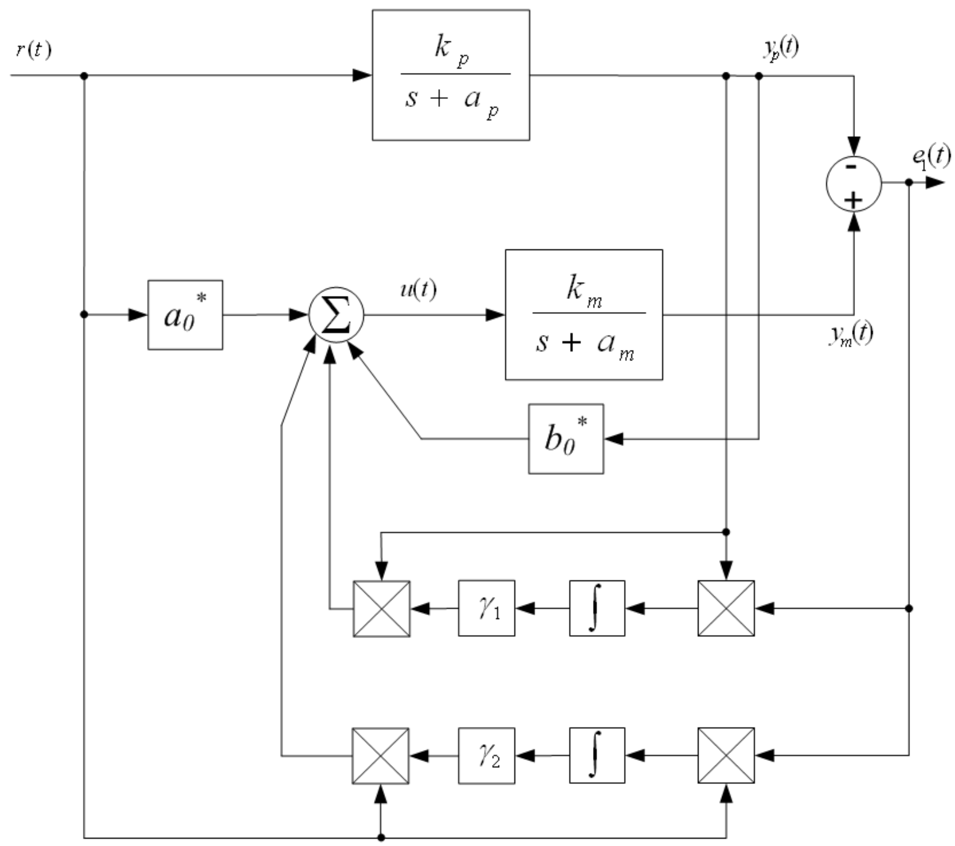

Figure 5.3: An equivalent structure of the model reference adaptive parameter identification with the adaptation law.

5.2.2 Model reference adaptive control

Based on the analysis in the previous section, model reference adaptive control will be discussed. Assume the plant under control is a first order linear time-invariant system, whose transfer function is:

$$P(s) = \frac{Y_p(s)}{U(s)} = \frac{k_p}{s + a_p} \tag{5.19}$$

where $Y_p(s)$ and $U(s)$ are system outputs and control signals, a_p and k_p are unknown system parameters.

The reference model is selected to be a stable single input single output linear time-invariant system with the following transfer function:

$$M(s) = \frac{Y_m(s)}{R(s)} = \frac{k_m}{s + a_m} \tag{5.20}$$

where a_m and k_m are greater than zero. Designers need to choose proper a_m and k_m parameters according to the desired control response.

The control objective is to design proper control signal $u(t)$, such that the plant output $y_p(t)$ is asymptotically tracking the output of the reference model $y_m(t)$. In time domain, the plant model and the reference model can be expressed in the following form, respectively.

$$\dot{y}_p(t) = -a_p y_p(t) + k_p u(t) \tag{5.21}$$

$$\dot{y}_m(t) = -a_m y_m(t) + k_m r(t) \tag{5.22}$$

The control signal $u(t)$ is calculated based on the knowledge of reference model input $r(t)$ and plant output signal $y_p(t)$. Figure 5.4 shows the closed-loop structure of a first order model reference adaptive control system. The system has a feedforward loop parameter $c_0(t)$ and feedback loop parameter $d_0(t)$. The control signal $u(t)$ can be expressed as:

$$u(t) = c_0(t) r(t) + d_0(t) y_p(t) \tag{5.23}$$

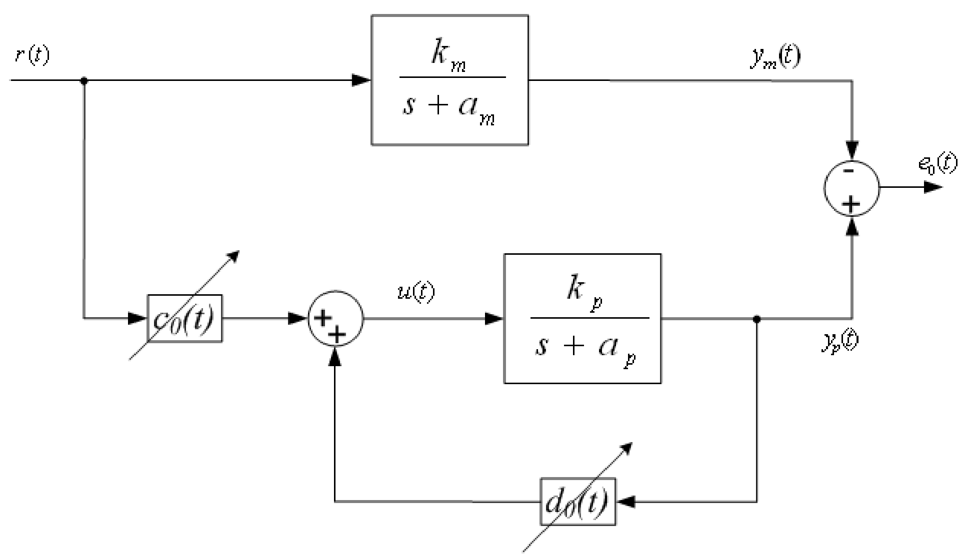

Figure 5.4: Structure of a first order model reference adaptive control system.

If considering,

$$c_0^* = \frac{k_m}{k_p}, \qquad d_0^* = \frac{a_p - a_m}{k_p} \tag{5.24}$$

the transfer function of the close system is the same as that of the reference model. Combine (5.21) and (5.23) and get:

$$\begin{aligned} \dot{y}_p(t) &= -a_p y_p(t) + k_p c_0(t) r(t) + k_p d_0(t) y_p(t) \\ &= -[a_p - k_p d_0(t)] y_p(t) + k_p c_0(t) r(t) \end{aligned} \tag{5.25}$$

When $c_0(t) = c_0^*$ and $d_0(t) = d_0^*$, (5.25) can be simplified as:

$$\dot{y}_p(t) = -a_m y_p(t) + k_m r(t) \tag{5.26}$$

which also represents the dynamic equation of the reference model.

Define the output error e_0 as:

$$e_0(t) = y_p(t) - y_m(t) \tag{5.27}$$

and define the parameter error as:

$$\phi(t) = \begin{bmatrix} \phi_r \\ \phi_y \end{bmatrix} = \begin{bmatrix} c_0(t) - c_0^* \\ d_0(t) - d_0^* \end{bmatrix} \tag{5.28}$$

Subtract (5.22) from (5.25), the derivative of the output error can be expressed as:

$$\begin{aligned} \dot{e}_0(t) &= -a_m(y_p - y_m) + (a_m - a_p + k_p d_0) y_p + k_p c_0 r - k_m(t) \\ &= -a_m e_0 + k_p[(c_0 - c_0^*) r + (d_0 - d_0^*) y_p] \\ &= -a_m e_0 + k_p(\phi_r r + \phi_y y_p) \end{aligned} \tag{5.29}$$

Alternatively, (5.29) can be re-written in the Laplace form:

$$\begin{aligned} e_0 &= \frac{k_p}{s + a_m}(\phi_r r + \phi_y y_p) \\ &= \frac{k_p}{k_m} M(\phi_r r + \phi_y y_p) \\ &= \frac{1}{c_0^*} M(\phi_r r + \phi_y y_p) \end{aligned} \tag{5.30}$$

Consider the following adaptation law:

$$\begin{aligned} \dot{c}_0 &= -g e_0 r \\ \dot{d}_0 &= -g e_0 y_p \end{aligned} \tag{5.31}$$

where g is the adaptation gain and $g > 0$. In the following, the stability of the model reference adaptive control system will be analyzed. The analysis is similar to that in the previous section. The error equations of the adaptive control system can be expressed as:

$$\begin{aligned} \dot{e}_0 &= -a_m e_0 + k_p(\phi_r r + \phi_y e_0 + \phi_y y_m) \\ \dot{\phi}_r &= -g e_0 r \\ \dot{\phi}_y &= -g e_0^2 - g e_0 y_m \end{aligned} \tag{5.32}$$

In the right hand side of (5.32), there are system states e_0, ϕ_r, ϕ_y and system inputs r, y_m. The positive definite Lyapunov function is selected as:

$$V(e_1, \phi_r, \phi_y) = \frac{1}{2}e_0^2 + \frac{k_p}{2g}(\phi_r^2 + \phi_y^2) > 0 \tag{5.33}$$

Take the first derivative of (5.33) over time,

$$\begin{aligned} \dot{V} &= -a_m e_0^2 + k_p\phi_r e_0 r + k_p\phi_y e_0^2 + k_p\phi_y e_0 y_m - k_p\phi_r e_0 r - k_p\phi_y e_0^2 - k_p\phi_y e_0 y_m \\ &= -a_m e_0^2 \end{aligned} \tag{5.34}$$

which is a negative semi-definite function. The original error equations are stable in the sense of Lyapunov at the equilibrium point of $e_0(t) = 0$.

The structure of the model reference control system is similar to that of model reference adaptive parameter identification system discussed in the previous section. The most significant difference is that the adaptation loop is connected to the plant instead of the reference model. The plant and the adaptive controller form the closed-loop control system. Similar to what was shown in Figure 5.2 and Figure 5.3, there are two methods of implementing model reference adaptive control: one is adjusting the parameters directly and the other one adjusts the input signal $u(t)$ directly. Figure 5.5 shows the structure of the model reference adaptive control system by adjusting the parameters directly.

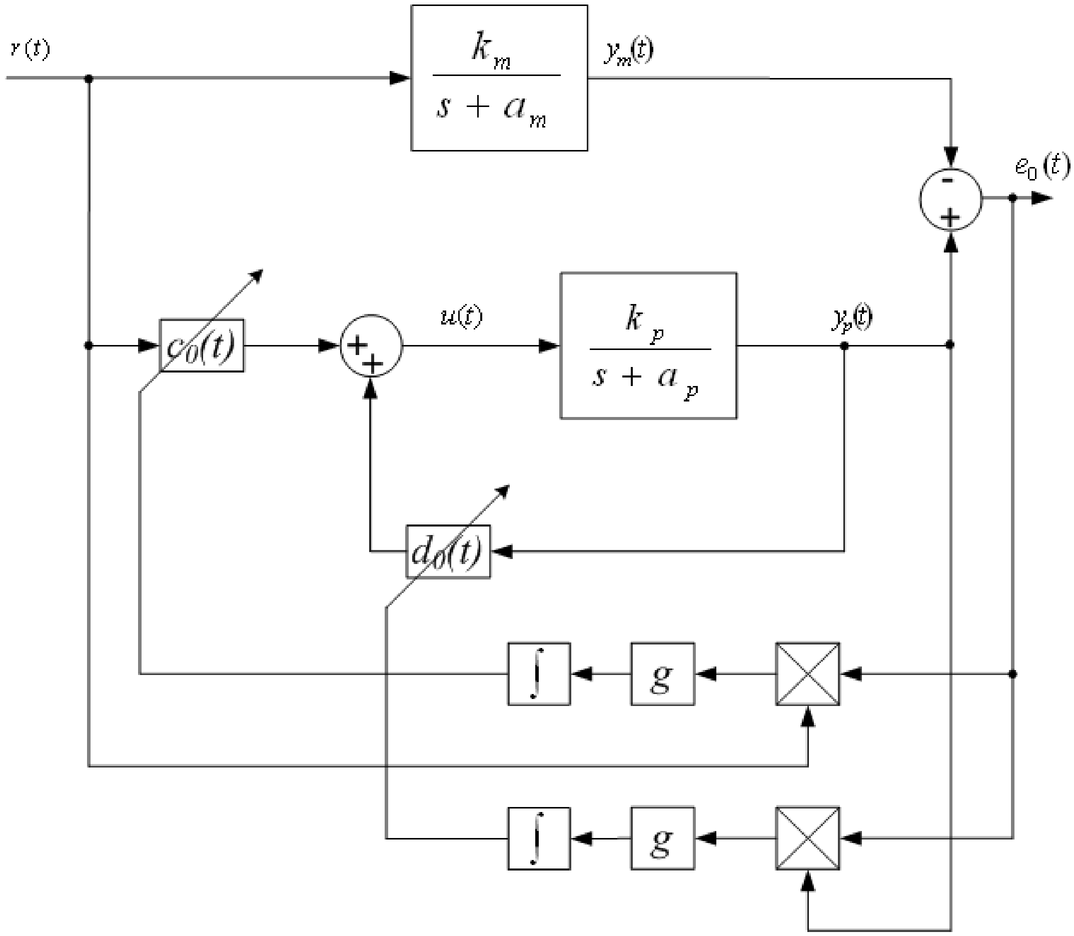

Figure 5.5: Structure of a first order model reference adaptive control system with adaptation law.

5.3 Mathematical model of five-phase IPM motors

5.3.1 Five-phase IPM motor equations

In this subsection, the mathematical model of five-phase IPM motors will be derived using the multiple reference frame transformation similar to the Park's transformation in three-phase motors.

The five-phase system provides additional degree of freedom by applying the following multiple reference frame transformation:

$$T(\theta)=\frac{2}{5}\begin{bmatrix} \cos(\theta) & \cos(\theta-\frac{2\pi}{5}) & \cos(\theta-\frac{4\pi}{5}) & \cos(\theta+\frac{4\pi}{5}) & \cos(\theta+\frac{2\pi}{5}) \\ -\sin(\theta) & -\sin(\theta-\frac{2\pi}{5}) & -\sin(\theta-\frac{4\pi}{5}) & -\sin(\theta+\frac{4\pi}{5}) & -\sin(\theta+\frac{2\pi}{5}) \\ \cos 3(\theta) & \cos 3(\theta-\frac{2\pi}{5}) & \cos 3(\theta-\frac{4\pi}{5}) & \cos 3(\theta+\frac{4\pi}{5}) & \cos 3(\theta+\frac{2\pi}{5}) \\ -\sin 3(\theta) & -\sin 3(\theta-\frac{2\pi}{5}) & -\sin 3(\theta-\frac{4\pi}{5}) & -\sin 3(\theta+\frac{4\pi}{5}) & -\sin 3(\theta+\frac{2\pi}{5}) \\ 1/2 & 1/2 & 1/2 & 1/2 & 1/2 \end{bmatrix} \tag{5.35}$$

where θ is the electrical rotor angle.

The voltage equations of a five-phase IPM motor can be described as [125]:

$$V_s = R_s I_s + \frac{d\Lambda_s}{dt} \tag{5.36}$$

where R_s is the matrix of stator resistances and V_s, I_s and Λ_s are stator voltages, currents and flux linkages,

$$V_s = [v_{as} \quad v_{bs} \quad v_{cs} \quad v_{ds} \quad v_{es}]^T$$

$$I_s = [i_{as} \quad i_{bs} \quad i_{cs} \quad i_{ds} \quad i_{es}]^T$$

$$\Lambda_s = [\lambda_{as} \quad \lambda_{bs} \quad \lambda_{cs} \quad \lambda_{ds} \quad \lambda_{es}]^T$$

Note that Λ_s include both flux linkages due to stator currents and rotor permanent magnets.

By applying the transformation matrix (5.35), five phase quantities in the stator reference frame will be transformed into two rotating frames: the *d*-*q* rotor reference frame which is rotating at synchronous speed and the d_3-q_3 frame which is rotating at three times the synchronous speed. These two reference frames are fully decoupled and the fundamental components of signals are reflected into the *d*-*q* frame with the 3rd order harmonics reflected into the d_3-q_3 frame.

The stator voltage equation can be obtained in this multiple reference frame:

$$v_d = r_s i_d - \omega_e L_q i_q + L_d \frac{di_d}{dt} \tag{5.37}$$

$$v_q = r_s i_q + \omega_e (L_d i_d + \lambda_m) + L_q \frac{di_q}{dt} \tag{5.38}$$

$$v_{d3} = r_s i_{d3} - 3\omega_e L_{q3} i_{q3} + L_{d3} \frac{di_{d3}}{dt} \tag{5.39}$$

$$v_{q3} = r_s i_{q3} + 3\omega_e (L_{d3} i_{d3} + \lambda_{m3}) + L_{q3} \frac{di_{q3}}{dt} \tag{5.40}$$

where v_d, v_q, v_{d3}, v_{q3} are the stator voltages in d, q, d_3, q_3 axes, respectively. i_d, i_q, i_{d3} and i_{q3} are the stator currents in corresponding rotating frames. λ_m and λ_{m3} are fundamental and third harmonic components of the transformed magnet flux linkages. ω_e is the electrical speed of the rotor. L_d, L_q, L_{d3} and L_{q3} are inductances in the rotating frames.

The electromagnetic torque equation can be derived by applying the co-energy method. When there is no saliency on the rotor, the electromagnetic torque is expressed as [94]:

$$T_e = \frac{5}{2} P_n (\lambda_m i_q + \lambda_{m3} i_{q3}) \tag{5.41}$$

If the rotor structure is salient with different L_d and L_q, the electromagnetic torque equation changes to:

$$T_e = \frac{5}{2} P_n \begin{bmatrix} (L_d - L_q) i_d i_q + 2L_{m13} (i_d i_{q3} - i_{d3} i_q) \\ + (L_{d3} - L_{q3}) i_{d3} i_{q3} + \lambda_m i_q + \lambda_{m3} i_{q3} \end{bmatrix} \tag{5.42}$$

where L_{ml3} is the mutual inductance in the rotating reference frame describing the voltage induced in d-axis by the change of current i_{q3}, or vice versa.

For most of the IPM motors manufactured, the back-EMFs are not perfect sinusoidal waveforms without any harmonic components. The 3rd order harmonic component in five-phase IPM motor back-EMF is usually the most dominant. Therefore, λ_{m3} is not usually zero for most of the five-phase IPM motors and the torque performance will be improved with certain 3rd order currents injected.

5.3.2 The optimum 3rd order current harmonics

The optimum 3rd order current harmonic will be derived based on the torque equation (5.41). The reluctance part in the torque equation is ignored at this time to provide simplicity in the analysis. In steady state, the electromagnetic torque is equal to the load torque, and is also the objective torque to be produced:

$$T_e = T^* \tag{5.43}$$

With the torque equation in (5.41), the q-axis current can be derived using the torque reference:

$$i_q^* = \frac{T^* - \frac{5}{2}P_n\lambda_{m3}i_{q3}^*}{\frac{5}{2}P_n\lambda_m} \tag{5.44}$$

One of the design criteria of motor drive is minimizing RMS phase currents, which is:

$$MIN(I_s) = MIN(\sqrt{i_q^{*2} + i_{q3}^{*2}}) \tag{5.45}$$

Substituting (5.44) into (5.45):

$$MIN(\sqrt{(\frac{T^* - \frac{5}{2}P_n\lambda_{m3}i_{q3}^*}{\frac{5}{2}P_n\lambda_m})^2 + i_{q3}^{*2}}) \tag{5.46}$$

The only variable is i_{q3} and the solution to minimize the equation is easy to find:

$$i_{q3}^* = \frac{\lambda_{m3}T^*}{\frac{5}{2}P_n(\lambda_m^2 + \lambda_{m3}^2)} \tag{5.47}$$

Substituting (5.47) back into (5.44) , the fundamental current component can be derived as:

$$i_q^* = \frac{\lambda_m T^*}{\frac{5}{2}P_n(\lambda_m^2 + \lambda_{m3}^2)} \tag{5.48}$$

Comparing (5.47) and (5.48), it is obvious that:

$$i_{q3}^* = \frac{\lambda_{m3}}{\lambda_m}i_q^* \tag{5.49}$$

So far, the optimum 3rd current equation has been derived to produce the same electromagnetic torque with the minimum RMS phase current. This can easily be used in any IPM motor drive and the only information needed is the motor no load back-EMFs. Furthermore, with the optimum 3rd current injected, the torque ripple will be minimized and the motor will run smoother. The detailed analysis is available in **Error! Reference source not found.**].

5.3.3 The proposed dynamic model of five-phase IPM motor

In this subsection, the IPM motor is modeled as a first-order continuous-time nonlinear dynamic equation to simplify the analysis of the proposed motor drive system. The mechanical dynamic of the motor can be modeled as:

$$J\frac{d\omega}{dt} + B\omega + T_L = T_e \tag{5.50}$$

where J is the moment of inertia of rotating parts. ω is the rotor mechanical speed. B is the damping constant. T_l is the mechanical load and T_e is the electromagnetic torque. If the motor 3rd order harmonic component in back-EMF is ignored and no 3rd order current is injected, the electromagnetic torque equation (5.42) can be simplified to be:

$$T_e = \frac{5}{2}P_n\left\{\lambda_m i_q + (L_d - L_q)i_d i_q\right\} \tag{5.51}$$

which is similar to that in a normal three phase IPM motor. In order to utilize the reluctance torque in IPM motors, the d-axis current should be injected for MTPA control. The equation to calculate i_d under MTPA operation is [121]:

$$i_d = \frac{\lambda_m}{2(L_q - L_d)} - \sqrt{\frac{\lambda_m^2}{4(L_q - L_d)^2} + i_q^2} \tag{5.52}$$

Substituting (5.51) and (5.52) into (5.50), the motor model can be expressed by the following first-order dynamic equation:

$$\frac{d\omega}{dt} + f(\omega, i_q) = i_q \tag{5.53}$$

where $f(\omega, i_q)$ is a non-linear function of the speed ω and the q-axis current i_q,

$$f(\omega, i_q) = \frac{B}{J}\omega + \frac{T_L}{J} - \frac{\frac{5}{4}P_n i_q}{J}\left(\sqrt{\lambda_m^2 + 4(L_d - L_q)^2 i_q^2} - \lambda_m\right) + \left(1 - \frac{\frac{5}{2}P_n\lambda_m}{J}\right)i_q \tag{5.54}$$

The detailed model of $f(\omega, i_q)$ is unknown because the parameters are not always available and the i_d equation (5.52) may change to (5.55) as the motor runs to high speed range and the flux weakening control is necessary [122].

$$i_d = -\frac{\lambda_m}{L_d} + \frac{1}{L_d}\sqrt{\frac{V_{\max}^2}{P_n^2\omega^2} - L_q^2 i_q^2} \tag{5.55}$$

Furthermore, in the five-phase IPM motor, electromagnetic torque equation (5.42) should be used instead of the simplified one (5.51), which will increase the complexity of the function f. The following analysis is only based on the assumption that function f is a highly non-linear function of ω and i_q. The detailed model of f is not needed in either designing or implementing the motor drive.

5.4 Experimental setup and parameter measurement of the five-phase IPM motor

A custom made five-phase IPM motor is used as an example to implement the proposed motor drive system. In this section, the experimental setup will be introduced. Motor parameters are required for accurate computer simulations and some control algorithm development. Parameter measurement process of this five-phase motor is also included in this section.

5.4.1 Experimental setup of the five-phase IPM motor

The experimental setup of this research is similar to that used in chapter 2. Figure 5.6 shows the configuration of the experimental setup. The motor under test is a custom made five-phase IPM motor. A five-leg IGBT-based VSI is connected to the DC bus to drive the motor. Structure of the interface board, optical incremental encoder, hall-effect transducers and the programmable mechanical load is kept the same. Figure 5.7 shows the photo of the designed experimental setup.

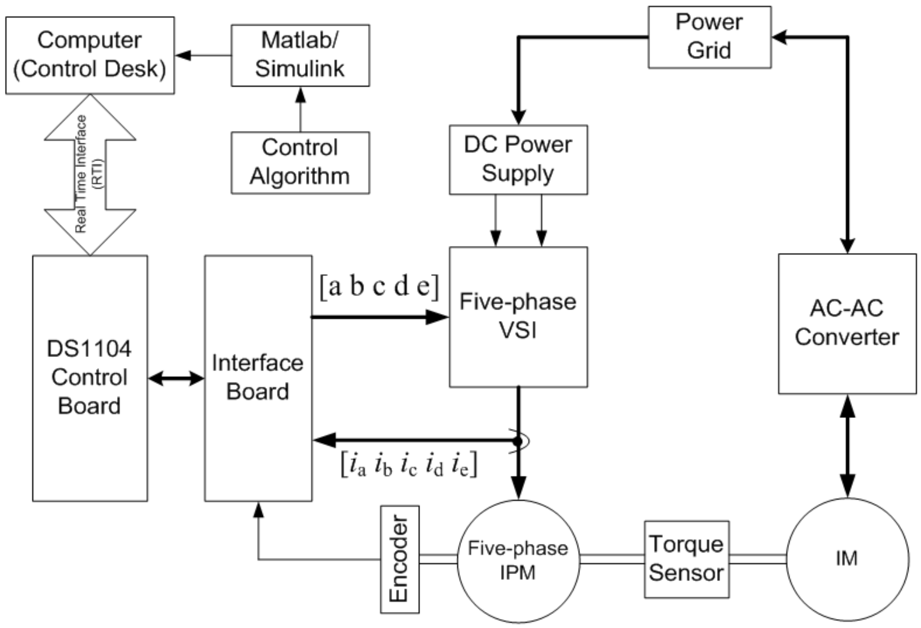

Figure 5.6: Experimental drive system configuration.

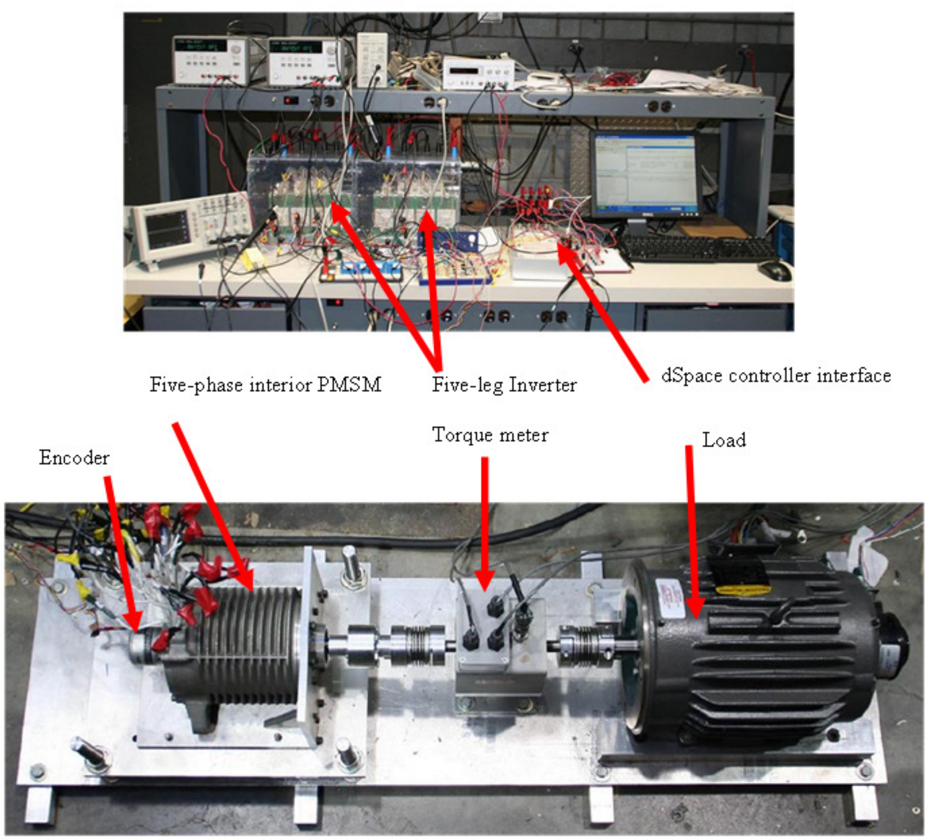

Figure 5.7: Experimental setup.

5.4.2 Parameter measurement of the five-phase IPM motor

(a) DC resistance

The electric circuit model of this five-phase Y-connected IPM motor is shown in Figure 5.8. A DC voltage is applied between any two of the phase terminals, i.e. A and B and the rest terminals are left open. By measuring the current flowing through terminal A and B, the total resistance $R_a + R_b$ can be estimated. Under this measurement, the motor is not running and the resistance measured is DC resistance at room temperature. Per phase resistance is:

$$r_s = 0.12 \quad \Omega \tag{5.56}$$

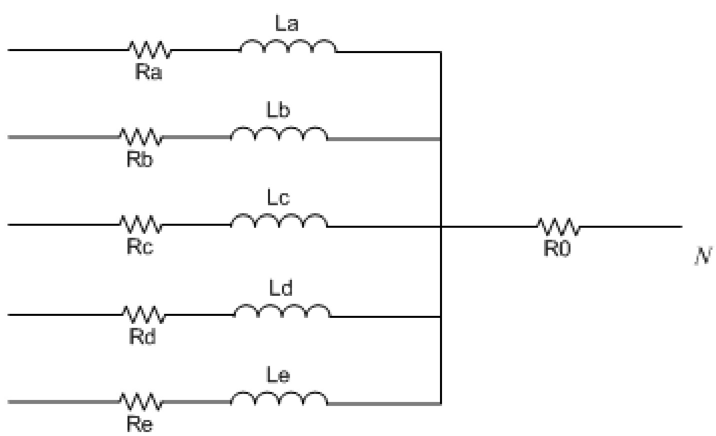

Figure 5.8: Electric circuit model of the five-phase IPM motor.

(b) Permanent magnet flux constant λ_m

No load test is first implemented to measure the permanent magnet flux constant λ_m. There is no current supplied on the IPM motor and the motor is set free. Using another motor to turn the five-phase IPM motor at different speed, phase A back-EMF is recorded, as shown in Table 5.1. The permanent magnet flux constant is calculated to be:

$$\lambda_m = 0.0402 \quad Wb \tag{5.57}$$

Table 5.1: No load back-EMF test data of the five-phase IPM motor.

Speed (rpm)	Back-EMF (phase A peak-peak /V)
300	5.12
450	7.68
600	10.2
750	12.6
900	15.1
1050	17.8
1200	20.4
1350	22.8
1500	25.2
1650	27.6
1800	30.4

Loaded test is also conducted to measure the permanent magnet flux constant. The steady state *q*-axis voltage equation is:

$$v_q = r_s i_q + \omega_e (L_d i_d + \lambda_m) \tag{5.58}$$

If controlling the *d*-axis current i_d to be zero, (5.58) reduces to:

$$v_q = r_s i_q + \omega_e \lambda_m \tag{5.59}$$

By keeping the mechanical load of the IPM motor to be constant, the *q*-axis current i_q will not change. At different speed, the *q*-axis voltage v_q will be recorded. Plot v_q with respect to speed ω_e, the slope of the v_q - ω_e curve will be the permanent magnet flux constant λ_m. Table 5.2 shows the data of loaded test of the five-phase IPM motor. Figure 5.9 shows the curve fitting of *q*-axis voltage v_q with respect to motor speed ω_e. The calculated slope which is also the permanent magnet flux constant λ_m is:

$$\lambda_m = 0.043 \quad Wb \tag{5.60}$$

Table 5.2: Loaded test of the five-phase IPM motor.

Speed (rpm)	q-axis voltage v_q
500	10.14
600	10.98
750	12.19
900	13.68
1050	15.08
1200	16.38

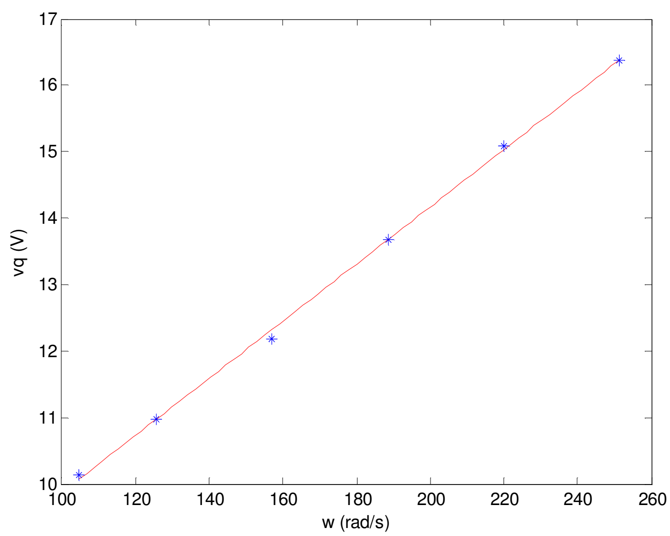

Figure 5.9: Curve fitting of the *q*-axis voltage with respect to speed.

(c) Five phase self-inductances

The motor has a relatively big magnetic core which might need high magnetizing current. Square wave pulses are applied from a high current power supply onto the inductor under measurement. Then, the current flowing through the inductor is recorded. The definition of inductance is:

$$v = L\frac{di}{dt} \tag{5.61}$$

In a small time instant, the equation can be written as:

$$\Delta v = L\frac{\Delta i}{\Delta t} \tag{5.62}$$

Or,

$$L = \Delta v \frac{\Delta t}{\Delta i} \tag{5.63}$$

As a result, the inductance can be calculated by taking a certain time instant and measure the voltage and current changes. With the presence of resistance in the circuit, the current waveform of an inductor under square wave voltage excitation will be an exponential function. In order to eliminate the effect of resistance, the linear part of the current waveform is preferred to make the inductance measurement, as shown in Figure 5.10.

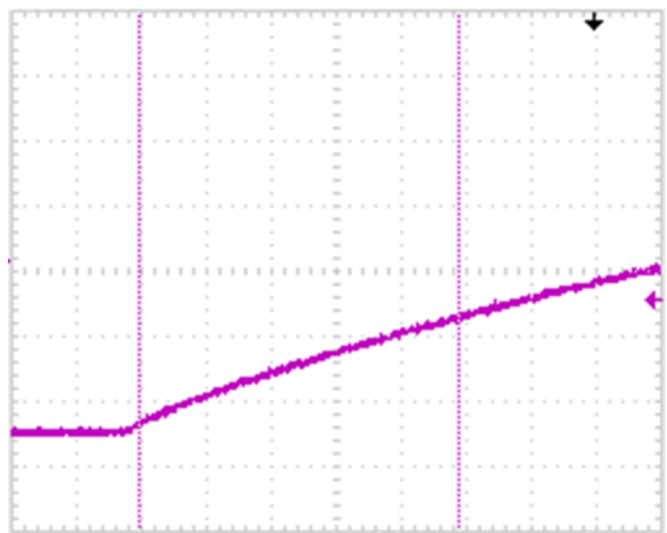

Figure 5.10: Current waveform of an inductor under square wave voltage excitation.

As the neutral point of the five-phase IPM motor is available, the individual phase inductance can be measured directly. The rotor is locked at different position when the inductance is measured. Figure 5.11 shows the measured inductance waveform of phase A. Neglecting the leakage inductances, the self-inductances of the five-phase IPM motor can be modeled as following:

$$\begin{aligned}
L_{aa} &= L_{aa0} + L_{g2}\cos(2\theta_e) \\
L_{bb} &= L_{aa0} + L_{g2}\cos(2(\theta_e - 72^o)) \\
L_{cc} &= L_{aa0} + L_{g2}\cos(2(\theta_e - 144^o)) \\
L_{dd} &= L_{aa0} + L_{g2}\cos(2(\theta_e + 144^o)) \\
L_{ee} &= L_{aa0} + L_{g2}\cos(2(\theta_e + 72^o))
\end{aligned} \tag{5.64}$$

where θ_e is the electrical angle of the rotor. Figure 5.12 shows the five-phase measured inductance values and the reconstructed values.

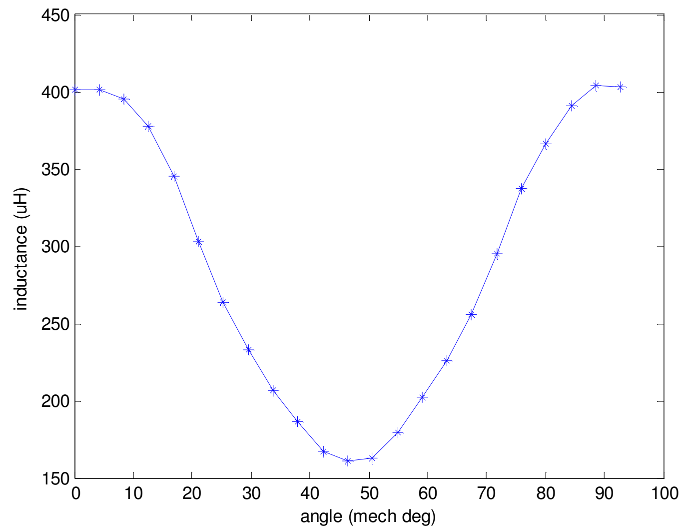

Figure 5.11: Measured phase A inductance waveform of the five-phase IPM motor.

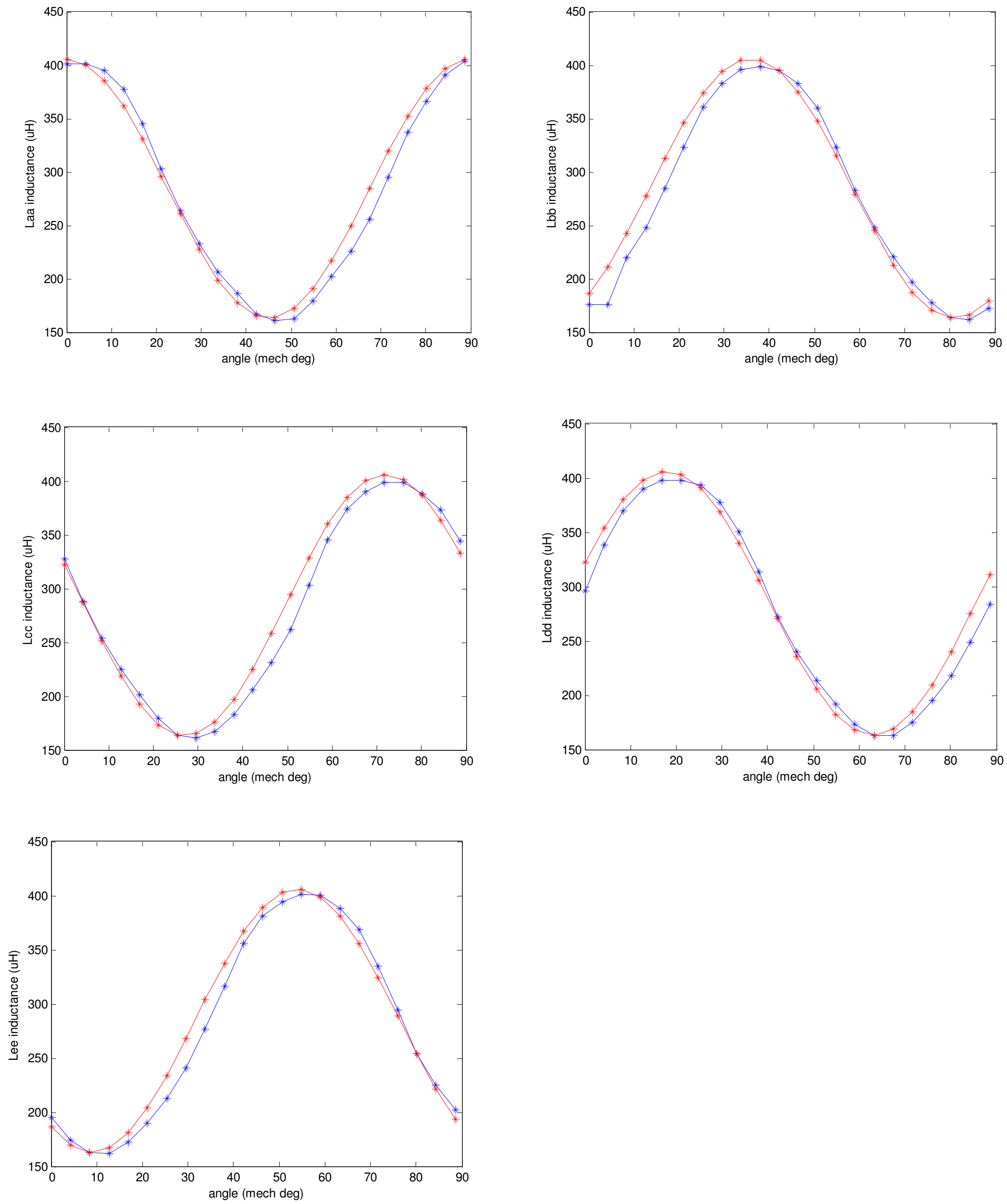

Figure 5.12: Five phase self-inductances: blue: measured; red: reconstructed by the model in (5.64).

(d) Mutual inductances

Mutual inductance is measured by exciting one phase, i.e. phase A. The induced voltages on phase B through phase E are recorded. Similar to the method applied on the self-inductance measurement, mutual inductances are also reconstructed as following:

$$
\begin{aligned}
M_{ab} &= M_{ab0} + M_{ab\_g2}\cos(2\theta_e - 72^o) \\
M_{ac} &= M_{ac0} + M_{ac\_g2}\cos(2\theta_e - 144^o) \\
M_{ad} &= M_{ad0} + M_{ad\_g2}\cos(2\theta_e + 144^o) \\
M_{ae} &= M_{ae0} + M_{ae\_g2}\cos(2\theta_e + 72^o)
\end{aligned}
\tag{5.65}
$$

By substituting θ_e by (θ_e - 72^0), phase B mutual inductances can be modeled. Mutual inductances of the rest phases can be modeled in a similar way. Figure 5.13 shows the measured and reconstructed mutual inductances of phase A.

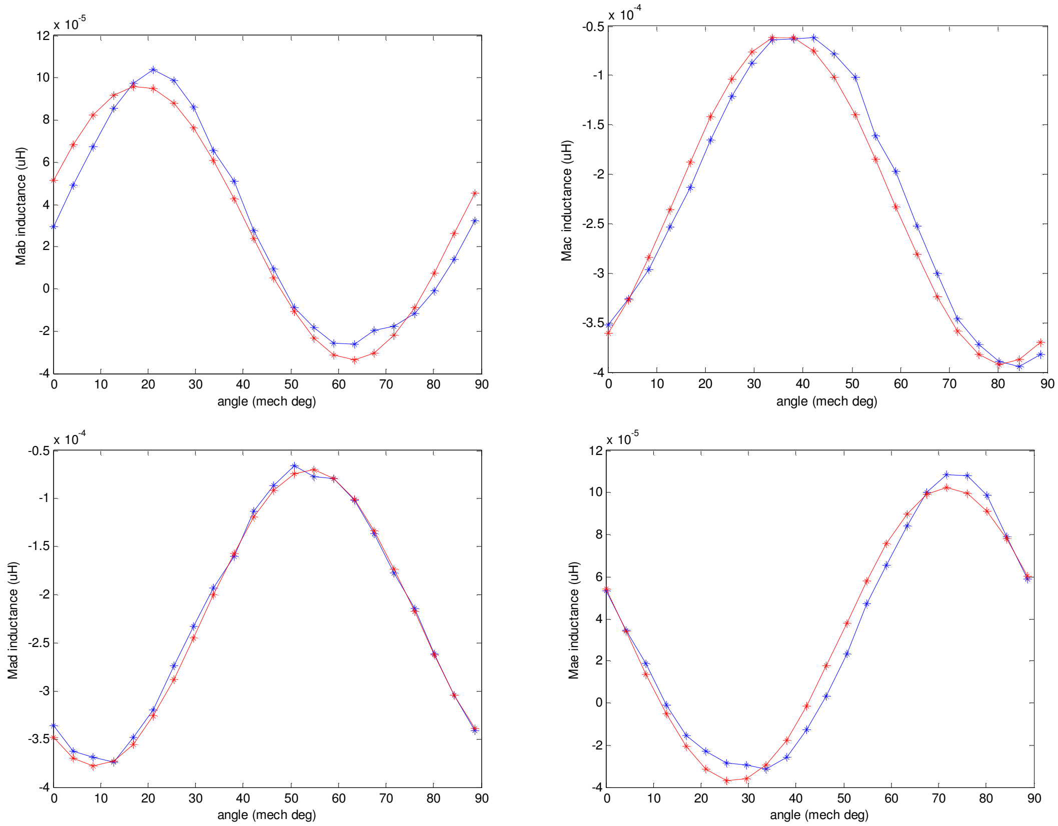

Figure 5.13: Mutual inductances of Phase A: blue: measured; red: reconstructed by the model in (5.69).

Inductances in the *d-q* rotor reference frame can be calculated from inductances in *a-b-c-d-e* reference frame by:

$$L_{dq} = TL_{abcde}T^{-1} \tag{5.66}$$

where the transformation matrix is as shown in (5.35). The *d-q* reference frame inductances are calculated as:

$$L_q = 956 \quad uH$$
$$L_d = 381 \quad uH \tag{5.67}$$

5.5 Model reference adaptive control without assistance of neural network model

5.5.1 Development of model reference adaptive control without neural network model

After examining the IPM motor model in (5.53), it can be seen that a first-order speed derivative is dominating the mechanical dynamic of the motor. Therefore, the reference model is selected to be a stable first-order linear model and expressed by the following differential equation:

$$\frac{d\hat{\omega}(t)}{dt} = -a\hat{\omega}(t) + b\omega^*(t) \tag{5.68}$$

where $\hat{\omega}$ is the state of the reference model and represents the desired state response of the closed-loop system. ω^* is an arbitrary speed reference signal as long as it is bounded and piecewise continuous. a and b are constants, which are both greater than zero and designed to represent the desired dynamic performance of the closed-loop system. In frequency domain, the transfer function of the reference model is:

$$\frac{\hat{\omega}(s)}{\omega^*(s)} = \frac{b}{s+a} \tag{5.69}$$

The control objective is to design a control law which generates the control signal i_q such that actual speed ω tracks the state of the reference model $\hat{\omega}$ for any speed reference input ω^*. In frequency domain, the closed-loop system transfer function from the input ω^* to speed output ω should be equal to that of the reference model given in (5.68). Figure 5.14 shows the IPM motor control block diagram with model reference adaptive control method.

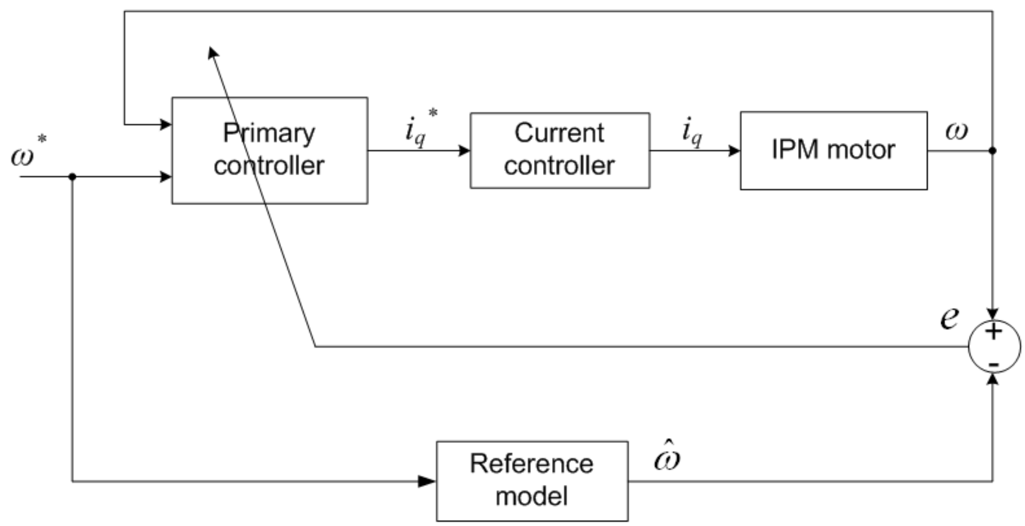

Figure 5.14: Structure of model reference adaptive control to control an IPM motor.

The primary controller is designed in the following form:

$$i_q = -k_1^*\omega + k_2^*\omega^* \tag{5.70}$$

Substitute (5.70) into the system dynamic equation (5.53):

$$\frac{d\omega}{dt} = h(\omega, i_q)\omega - k_1^*\omega + k_2^*\omega^* \tag{5.71}$$

and rewrite (5.71) in transfer function form as following:

$$\frac{\omega(s)}{\omega^*(s)} = \frac{k_2^*}{s - h(\omega, i_q) + k_1^*} \tag{5.72}$$

For the speed output ω to track the reference model state $\hat{\omega}$, the transfer function in (5.72) should be equal to that in (5.69). The following design criteria are obvious:

$$\begin{aligned} k_2^* &= b \\ k_1^* &= a + h(\omega, i_q) \end{aligned} \tag{5.73}$$

The system is controllable with such control parameters and the closed-loop transfer function is equal to that of the reference model. The designed control law will guarantee the system output speed ω will converge to reference model state $\hat{\omega}$ exponentially. However, the control law in (5.70) cannot be implemented as parameters k_1^* cannot be explicitly calculated with unknown function h. Therefore, an updating algorithm is needed to calculate parameters k_1^* and k_2^* online without the knowledge of the function h.

Instead of (5.70), the q-axis current i_q is designed using adaptively updated parameters

$$i_q = -k_1(t)\omega + k_2(t)\omega^* \tag{5.74}$$

where $k_1(t)$ and $k_2(t)$ will estimate parameters k_1^* and k_2^* online. With appropriately designed adaptive algorithm, $k_1(t)$ and $k_2(t)$ will tend to k_1^* and k_2^* with satisfactory accuracy, respectively.

Design of the adaptive algorithm starts from adding and subtracting the q-axis current i_q in the system dynamic equation (5.53):

$$\frac{d\omega}{dt} = h(\omega, i_q)\omega - k_1^*\omega + k_2^*\omega^* + (k_1^*\omega - k_2^*\omega^* + i_q) \tag{5.75}$$

Substitute (5.73) into (5.75) to obtain:

$$\frac{d\omega}{dt} = -a\omega + b\omega^* + (k_1^*\omega - k_2^*\omega^* + i_q) \tag{5.76}$$

Rewrite (5.76) in frequency domain to obtain:

$$\omega = \frac{b}{s+a}\omega^* + \frac{1}{s+a}(k_1^*\omega - k_2^*\omega^* + i_q) \tag{5.77}$$

From (5.69), it can be seen that the first term in the right hand side of (5.77) is simply the reference model state $\hat{\omega}$. As a result, if defining the state tracking error e to be the difference between system output ω and reference model state $\hat{\omega}$, it can be expressed as:

$$e \stackrel{\Delta}{=} \omega - \hat{\omega} = \frac{1}{s+a}(k_1^*\omega - k_2^*\omega^* + i_q) \tag{5.78}$$

The final control objective is to eliminate this state tracking error. If the actual control parameter i_q as in (5.74) is applied, the state tracking error becomes:

$$e = \frac{1}{s+a}\{k_1^*\omega - k_2^*\omega^* - k_1(t)\omega + k_2(t)\omega^*\} \tag{5.79}$$

If defining the parameter adaptation errors to be:

$$\tilde{k}_1 \overset{\Delta}{=} k_1(t) - k_1^*$$
$$\tilde{k}_2 \overset{\Delta}{=} k_2(t) - k_2^* \qquad (5.80)$$

The state tracking error e can be expressed using these adaptation errors,

$$e = \frac{1}{s+a}(-\tilde{k}_1\omega + \tilde{k}_2\omega^*) \qquad (5.81)$$

In the differential equation form, the state tracking error is:

$$\frac{de}{dt} = -ae + (-\tilde{k}_1\omega + \tilde{k}_2\omega^*) \qquad (5.82)$$

By examining (5.82), it is clear that if the parameter errors $\tilde{k}_1$ and $\tilde{k}_2$ are zero, the state tracking error e tends to zero exponentially. The origin of this 3rd order differential equation is the equilibrium point:

$$e = 0; \quad \tilde{k}_1 = 0; \quad \tilde{k}_2 = 0 \qquad (5.83)$$

According to Lyapunov stability theory, if a positive definite function V can be found, and its first order derivative $\dot{V}$ is a negative definite function or negative semi-definite function, the original system is stable around the origin. Consider the following quadratic function of ω, $\tilde{k}_1$ and $\tilde{k}_2$:

$$V(e, \tilde{k}_1, \tilde{k}_2) = \frac{e^2}{2} + \frac{\tilde{k}_1^{\,2}}{2q_1} + \frac{\tilde{k}_2^{\,2}}{2q_2} \qquad (5.84)$$

This function is positive definite if q_1 and q_2 are positive constants. Take the derivative of function V and obtain:

$$\dot{V}(e, \tilde{k}_1, \tilde{k}_2) = -ae^2 - \tilde{k}_1 e\omega + \tilde{k}_2 e\omega^* + \frac{\tilde{k}_1}{q_1}\frac{dk_1}{dt} + \frac{\tilde{k}_2}{q_2}\frac{dk_2}{dt} \qquad (5.85)$$

If the following criteria are met:

$$\frac{dk_1}{dt} = eq_1\omega$$
$$\frac{dk_2}{dt} = -eq_2\omega^* \qquad (5.86)$$

derivative of function V reduces to:

$$\dot{V}(e, \tilde{k}_1, \tilde{k}_2) = -ae^2 \qquad (5.87)$$

which is a negative semi-definite function, and the original system is stable in the sense of Lyapunov. Equation (5.86) is able to work as the adaptive algorithm for updating the control parameters online. According to the previous analysis, the structure of primary controller used in this model reference adaptive control is shown in Figure 5.15.

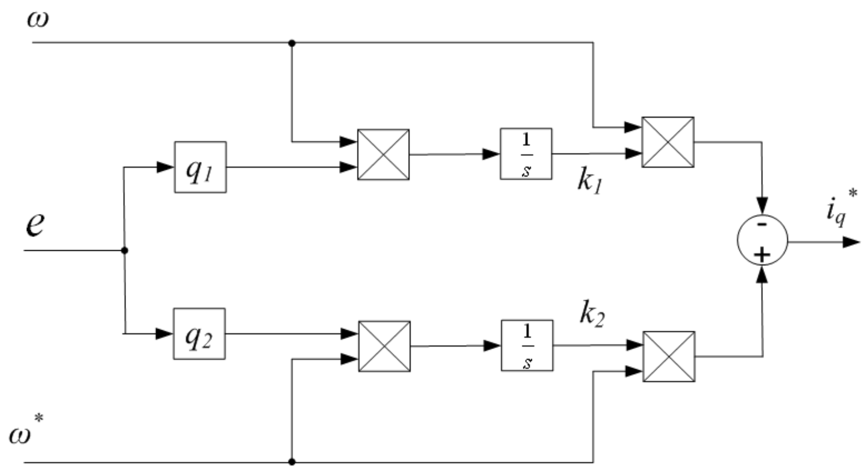

Figure 5.15: Structure of the primary controller.

5.5.2 Simulation and experimental results

This section presents some simulation and experimental results of this IPM motor drive under model reference adaptive control. Simulation has been done in Matlab/Simulink environment. The IPM motor parameters used in this simulation are as follows:

d axis inductance $L_d = 381\mu H$;

q axis inductance $L_q = 956\mu H$;

Mutual inductance: $L_{m13} = 0$ H;

Stator phase resistance: $r_s = 0.21$ ohm;

Rotational moment of inertia: $J = 0.015$ kg.m^2;

Friction constant: $B = 0.001$ Nm/rad/s;

Permanent magnet flux linkage $\lambda_m = 0.043$ Wb;

Figure 5.16 shows the simulated speed responses of the IPM motor under model reference adaptive control. It can be seen that the motor dynamic is following exactly the reference model both accelerating and decelerating.

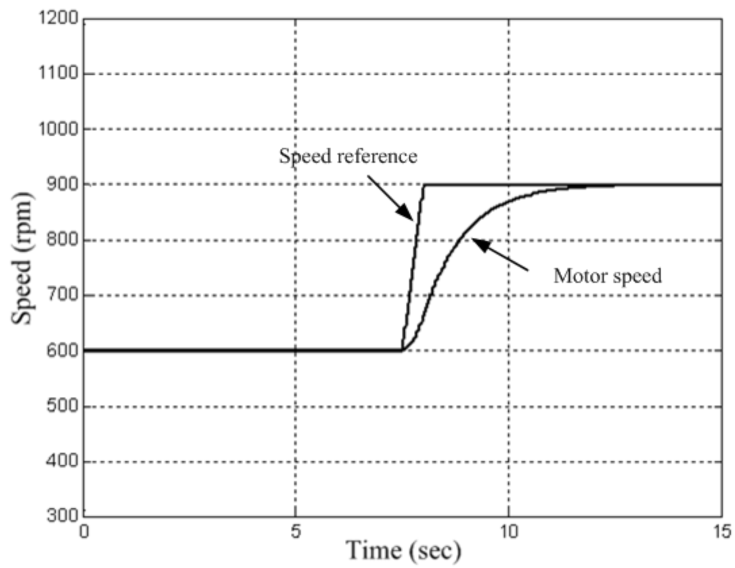

(a)

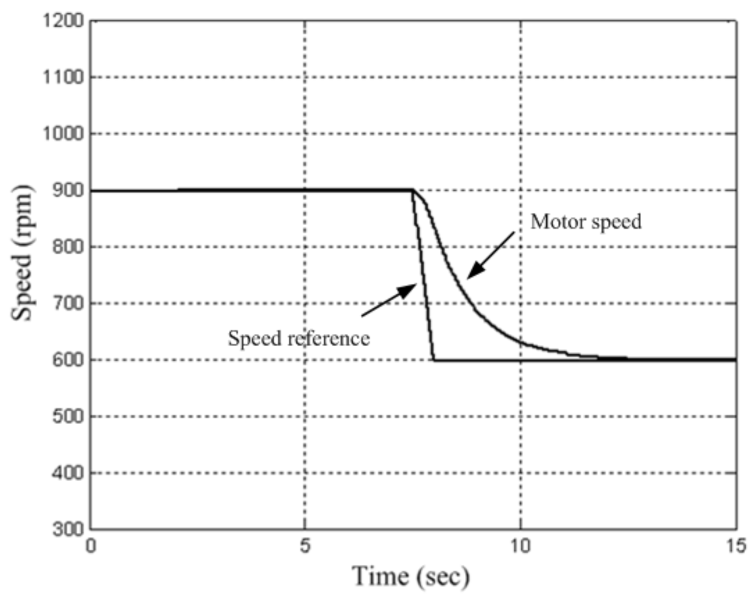

(b)

Figure 5.16: Simulated IPM motor speed dynamic responses: (a) accelerating; (b) decelerating.

This model reference adaptive control method is also tested in lab. The control algorithm is designed in Matlab/Simulink environment, and downloaded into the dSPACE controller board using the “Real Time Interface” (RTI). The reference model shares the same parameters as in the computer simulation section, and is solved in real time on the controller board. The digital control of the motor is also implemented on the dSPACE controller board. The sampling frequency for the model reference adaptive speed control is 1 kHz.

Figure 5.17 shows the experimented IPM motor speed responses. It can be seen that the speed dynamic matches with simulation results. Both the accelerating and decelerating dynamic follows pre-set model reference very well. However, the motor currents are switching between the saturated value and a low value, which is low enough to guarantee the decelerating dynamic, as shown in Figure 5.18. Even though the speed control is perfect for this model reference adaptive control method, the lack of stability in current control makes this method less practical in many industrial applications. In the following section, an improved IPM motor drive system will be developed with the assistance of a neural network model.

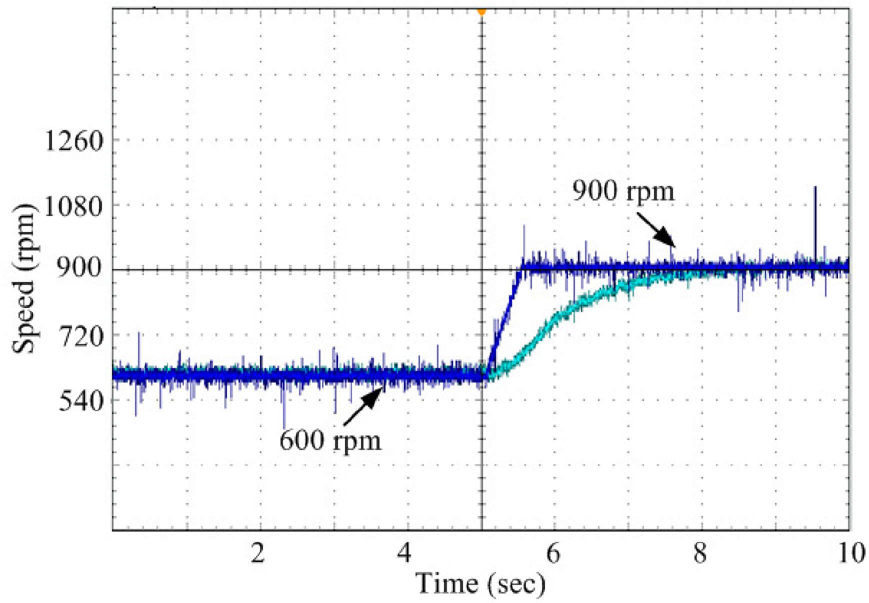

(a)

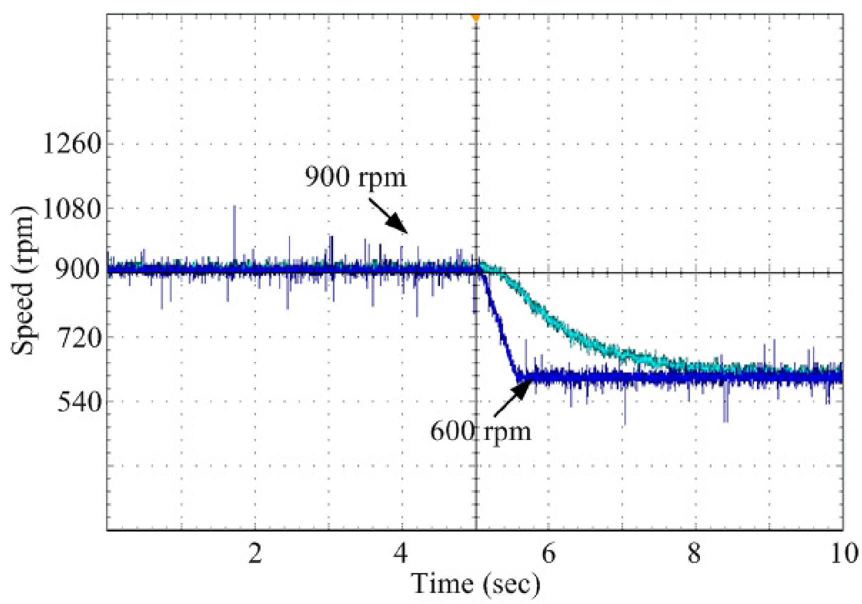

(b)

Figure 5.17: Experimental result of IPM motor speed dynamic responses: (a) accelerating; (b) decelerating.

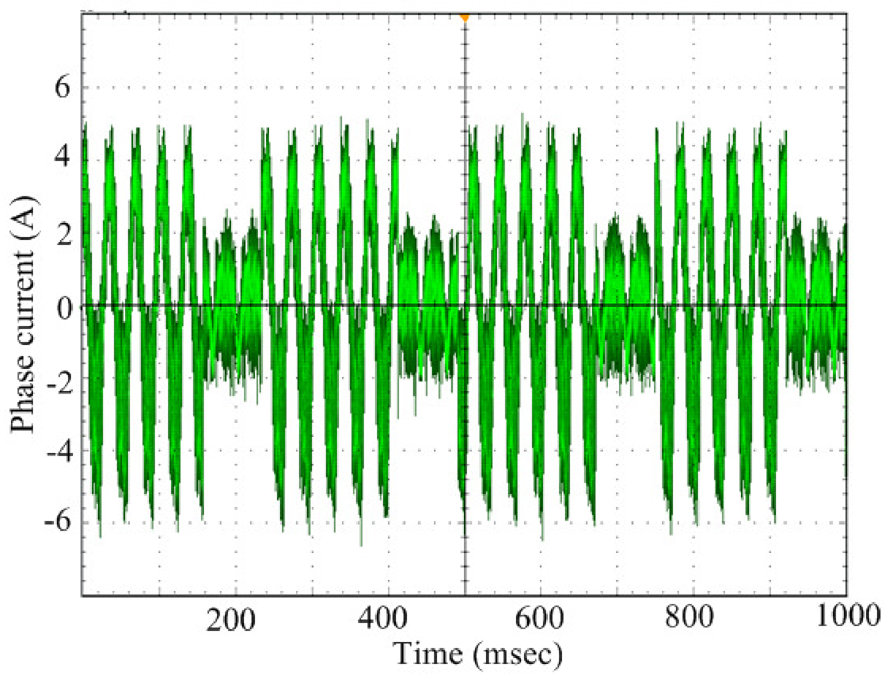

Figure 5.18: IPM motor current waveform (Phase A).

5.6 Design of model reference adaptive control based on neural network

5.6.1 MRAC scheme

The objective of MRAC is to design a control law which generates the q-axis current reference i_q^* and an updating law for the primary controller parameters, such that the system output ω is following the reference signal and the closed-loop dynamic performance of the system is following the linear reference model [123]. The interior characteristic of model reference adaptive control guarantees the dynamic performance of the closed-loop system as long as the controller is properly designed.

After examining the IPM motor model in (5.53), it can be seen that a first-order speed derivative is dominating the mechanical dynamic of the motor. Therefore, the reference model is selected to be a stable first-order linear model and expressed by the following differential equation:

$$\dot{\hat{\omega}}(t) + a\hat{\omega}(t) = k\omega^*(t) \tag{5.88}$$

where a and k are constant, which are both greater than zero and decide the objective dynamic performance of the closed-loop system. Figure 5.19 shows the neural network assisted MRAC structure which will be used in the proposed motor drive, which has better performance than that introduced in the previous section. The reference model is represented by (5.88). The primary controller is a novel ANN type controller. The current controller is hysteresis type controller with adjustable band. Figure 5.20 shows the complete block diagram of the proposed motor drive system. The speed error between reference and the measured signal is fed into the proposed model reference adaptive controller. The output of the neutral network primary controller works as the *q*-axis current reference signal. The i_q^* passes through a full current generator where both the torque current i_q and the flux current i_d can be controlled. If the motor drive decides to inject some 3rd order currents, the current references will also be generated in this block. The outputs of the hysteresis current controller are five phase switching signals which drive the inverter connected directly to the IPM motor.

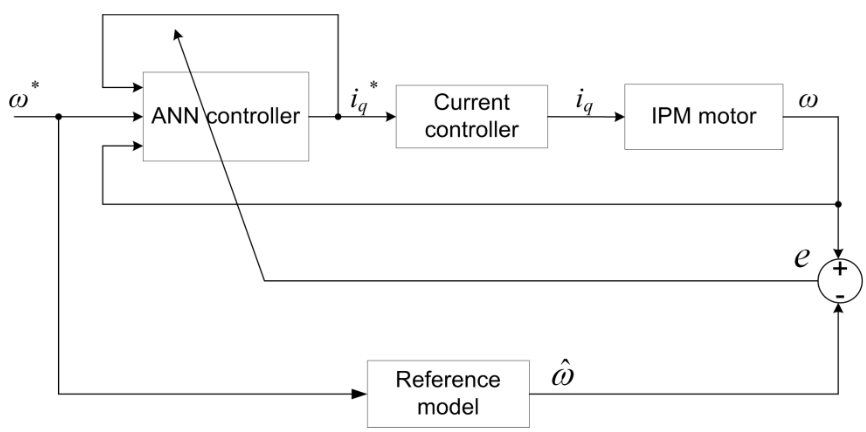

Figure 5.19: MRAC structure by neural network.

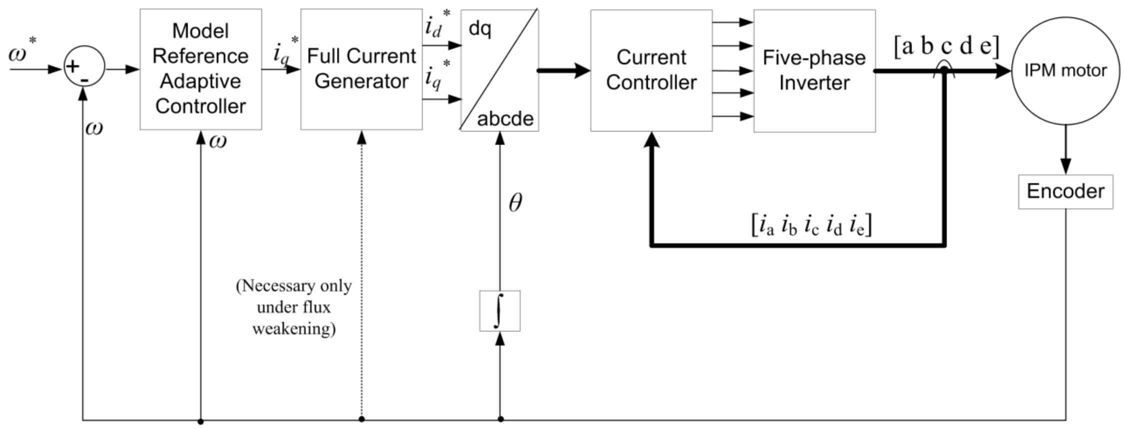

Figure 5.20: Complete block diagram of the proposed motor drive.

5.6.2 ANN primary controller design

The primary ANN controller in Figure 5.19 is designed in the following form:

$$i_q^* = -a\omega + k\omega^* + N_f(\omega, i_q, w) \tag{5.89}$$

where N_f works as a substitution of nonlinear function f and is implemented using a radial basis function (RBF) neural network. w is the parameter vector of N_f and will be updated on-line to minimize the error between the neural network simulator N_f and the unknown nonlinear function f. Substituting (5.89) and (5.88) into (5.53):

$$\dot{\omega}(t) + f(\omega, i_q) = -a\omega(t) + \dot{\hat{\omega}}(t) + a\hat{\omega}(t) + N_f(\omega, i_q, w) \tag{5.90}$$

Define the error signal as:

$$e(t) = \omega(t) - \hat{\omega}(t) \tag{5.91}$$

and express the result in terms of error signal $e(t)$:

$$\dot{e}(t) + ae(t) = N_f(\omega, i_q, w) - f(\omega, i_q) \tag{5.92}$$

After proper training of the neural network function N_f, which is designed to represent the nonlinear function f, the difference between N_f and f tends to zero. Hence, (5.92) is asymptotically stable around the equilibrium point at the origin as long as $a > 0$. Figure 5.21 shows the structure of the proposed ANN controller.

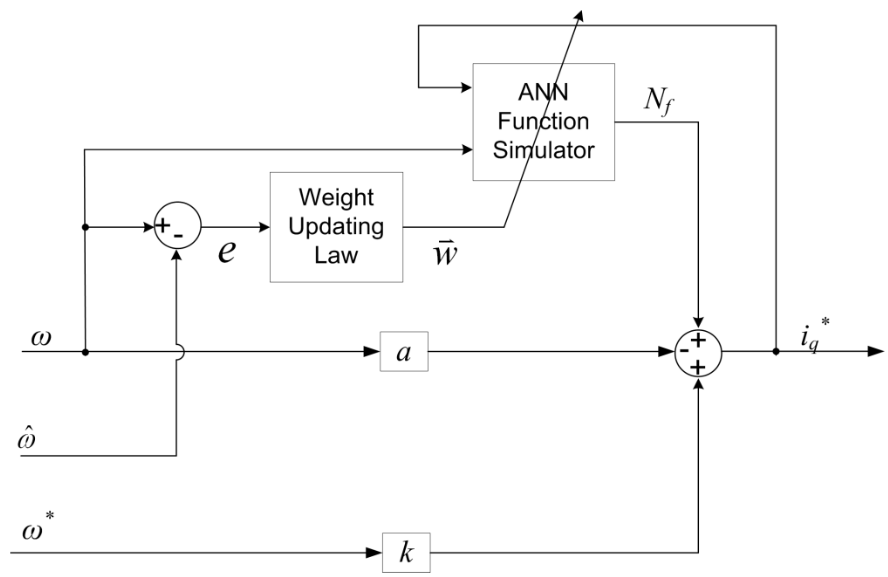

Figure 5.21: ANN controller structure.

The neural network used to simulate the nonlinear function *f* is a Gaussian type RBF network. Figure 5.22 illustrates the basic structure of a RBF network. It features a three layer structure. The first layer is the input layer with nominal gains. The middle layer consists of several nonlinear transfer functions to simulate the nonlinear characteristics. *n* is the number of hidden neurons used in the network. Usually, the more neurons in the middle layer, the easier the network can be trained, but the calculation load will become more intensive. The selection of the number of hidden neurons is on a trial and error basis and it is more important in this work as the neural network will train itself online as the system is running. The output layer of the network applies different weighting factor to each nonlinear transfer function and sums them up.

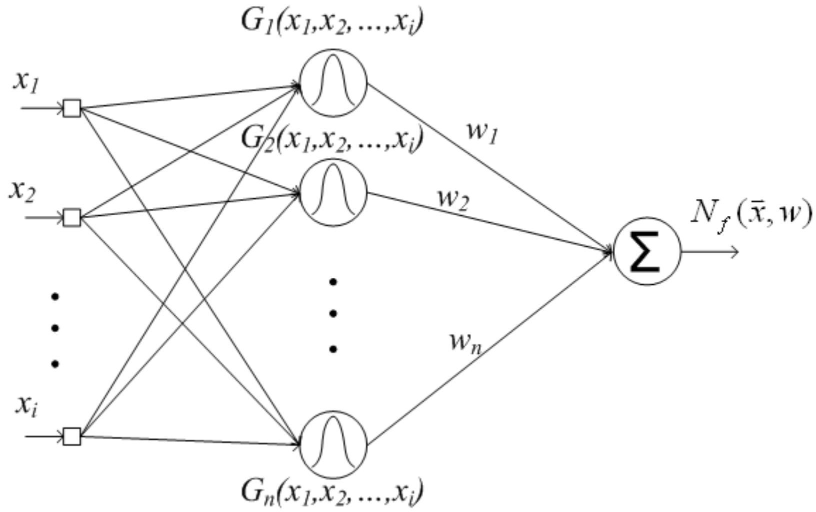

Figure 5.22: Gaussian type RBF network.

There are various nonlinear functions which can be used as the transfer function. In this work, the one selected in the RBF network is Gaussian function, which is the most commonly used basis function:

$$G(\bar{x}) = \exp(-\frac{\|\bar{x}-\bar{c}\|^2}{2\delta^2}) \tag{5.93}$$

where x is the input vector, c is the center vector of corresponding Gaussian function, and δ is called the "radius" of the function. The input vector includes the normalized speed ω and i_q.

Before the designed model reference adaptive control can work properly, the neural network function simulator should be first well trained. Not like some other neural network applications when training data are easy to obtain, it is impossible to gather adequate experimental speed ω and i_q data for offline training in this work. Online parameter updating is then required. In addition, online training also enables the ANN primary controller to continuously minimize the simulation error of the actual nonlinear function f.

The weight vector updating law is based on the speed error and the previous time weight vector. In continuous-time format, the weight updating law is expressed as:

$$\dot{w}(t) = -\Lambda Q(t)e(t) - \Omega w(t) \tag{5.94}$$

where Λ and Ω are diagonal matrices with all diagonal elements greater than zero. $e(t)$ is the speed error signal, and $Q(t)$ is the output vector in terms of the weights:

$$Q(t) = [G_1 \quad G_2 \quad \cdots \quad G_n]^T \tag{5.95}$$

and

$$N_f = Q^T(t)w(t) \tag{5.96}$$

Details of the stability analysis can be found in [123].

5.6.3 Simulation and experimental results

In this section, the proposed neural network assisted model reference adaptive control method is simulated in Matlab/Simulink environment. The motor parameters are the same as described in the previous section. The five-phase permanent magnet motor is modeled with the torque equation in (5.42). The measured speed signal ω and q axis current i_q are first normalized to be a value between 0 and 1 before being fed into the RBF network. There are 50 neurons used in the hidden layer. The center vector c is evenly distributed between -2 and 2 and the radius δ is 0.5 for each Gaussian function. During this simulation, the parameters for the reference model in MRAC scheme are a = 1 and k = 1. Therefore, the transfer function for the reference model is:

$$H(s) = \frac{1}{s+1} \tag{5.97}$$

The weight vector updating constants for the RBF network are selected as follows:

$$\Lambda = diag(3250, \cdots, 3250) \tag{5.98}$$

$$\Omega = diag(40, \cdots, 40) \tag{5.99}$$

Figure 5.23 shows the simulated speed response of the proposed motor drive at full load. It can be seen that the proposed speed controller has fast and accurate response. The reference speed is switching between 600 rpm and 900 rpm. The motor speed follows the reference signal in less than 5 seconds and there is no overshoot. During the simulation, the parameters for the reference model in MRAC scheme are $a = 1$ and $k = 1$.

It is also shown that the closed-loop system performance is following the reference model well.

Figure 5.24 presents the simulated phase A and phase B currents when there are only fundamental currents while Figure 5.25 show that when the 3rd order harmonic components are also injected. Under the same load condition, less current is needed when proper 3rd order harmonics are injected.

High speed performance in the flux weakening region is also simulated. Figure 5.26 shows the speed response from 1500rpm to 1800rpm. It can be seen that at different operating point, the proposed control method guarantees an identical dynamic performance.

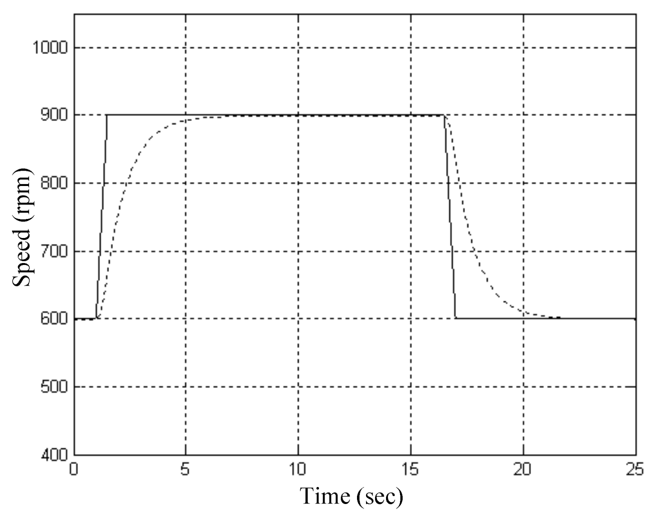

Figure 5.23: Simulated speed response of the five phase motor with the proposed motor drive (600rpm-900rpm).

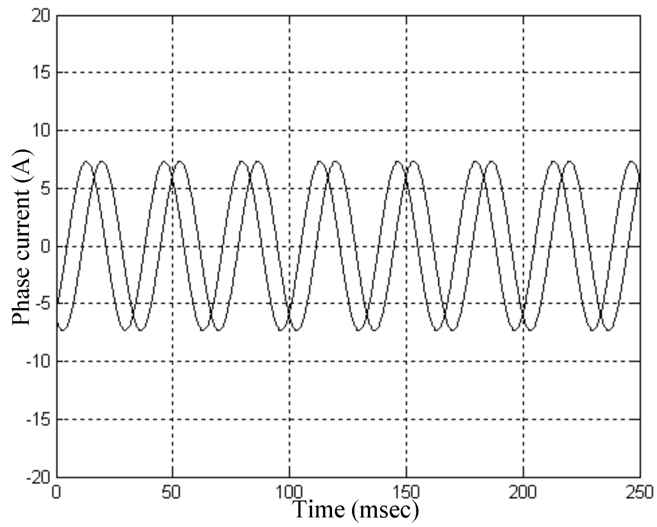

Figure 5.24: Simulated phase A and phase B currents without 3rd harmonic components injected (@ 900rpm).

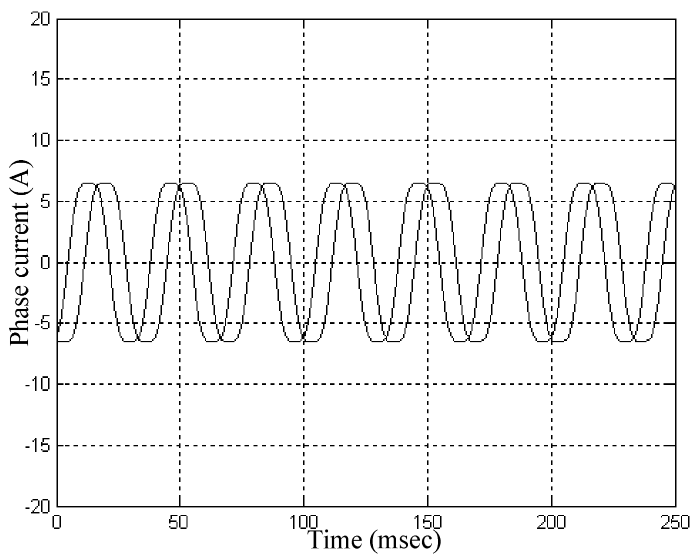

Figure 5.25: Simulated phase A and phase B currents with 3rd order harmonic components injected (@ 900rpm).

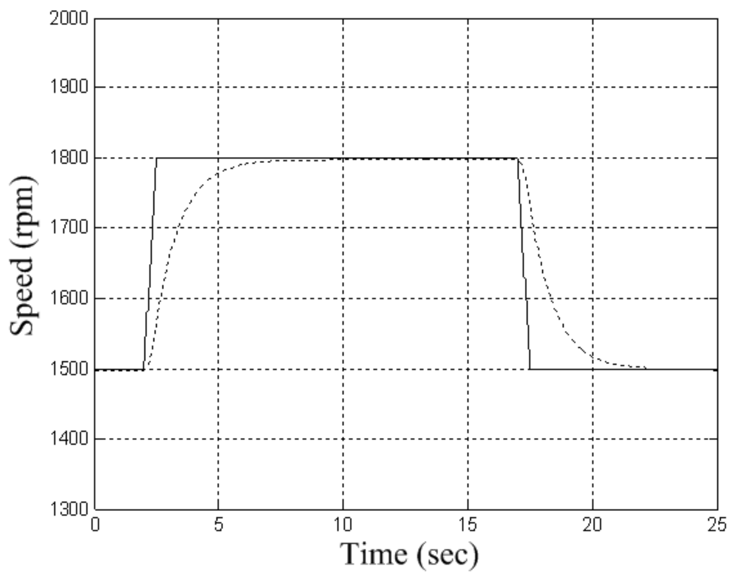

Figure 5.26: Simulated speed response of the five phase motor with the proposed motor drive (1500rpm-1800rpm).

The proposed motor drive system is also tested in lab. The number of neurons in the neural network is limited by the calculation speed of processor and the sampling time. The training is easier and faster with more neurons in the neural network, but the controller board may not work in real time. By trial and error method, the number of neurons in this design has to be below 150; otherwise the control algorithm cannot run in real time. The neuron number is selected to be 50 to allow a fast convergence.

To compare the performance of conventional PI speed controller with the proposed MRAC controller, a well-tuned PI controller is needed. The five-phase IPM motor model in (5.42) is first simplified to conduct theoretical analysis and parameter design for its PI controller. The electrical system is considered to be much faster than mechanical system. In this PI parameter design process, the switching is also neglected. All parameter variations, saturation and other nonlinear properties are also ignored. Consider the electromagnetic torque equation without reluctance:

$$T_e = \frac{5}{2} P_n \lambda_m i_q \tag{5.100}$$

Define the torque constant to be:

$$K_t = \frac{5}{2} P_n \lambda_m \tag{5.101}$$

Therefore, the electromagnetic torque is:

$$T_e = K_t i_q \tag{5.102}$$

Using the mechanical dynamic equation described in (5.50), the speed control is simplified as in Figure 5.27 after all the assumptions.

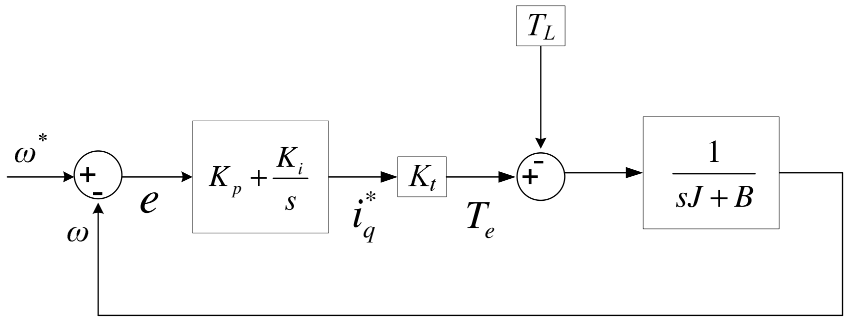

Figure 5.27: Simplified speed control loop of the five-phase IPM machine.

Under no load, the closed-loop transfer function of this speed control is expressed as:

$$\frac{\omega}{\omega^*} = \frac{K_t}{s\dfrac{Js+B}{K_p s + K_i} + K_t} \tag{5.103}$$

With the following selection of the PI controller parameters, the closed-loop performance can be controlled to be a first-order system with the bandwidth of ω_s.

$$K_p = \frac{\omega_s J}{K_t} \tag{5.104}$$

$$K_i = \frac{\omega_s B}{K_t} \tag{5.105}$$

In the MRAC motor drive design, the motor is controlled to follow the first-order reference model as in (5.97). The closed-loop bandwidth of this reference model is 1 rad/s. Here, the PI controller is also designed to have similar dynamic performance with the same bandwidth. After substituting all the motor parameters, the PI controller parameters are calculated to be: $K_p = 0.069$ and $K_i = 0.005$. Experiments have shown that the integral gain K_i is not big enough to eliminate the steady state error. This is mostly because of inaccurate measurement of the friction constant B. K_i is increased to be 0.035 by manual tuning. Figure 5.28 shows the speed response of the five-phase motor with this fixed parameter PI speed controller. The speed command is changed between 600rpm and 900rpm, and the measured speed is recorded. In order to reduce the overshoot, the proportional gain K_p is adjusted to 0.13. Figure 5.29 shows the speed response with the improved PI controller. The tradeoff is increased settling time.

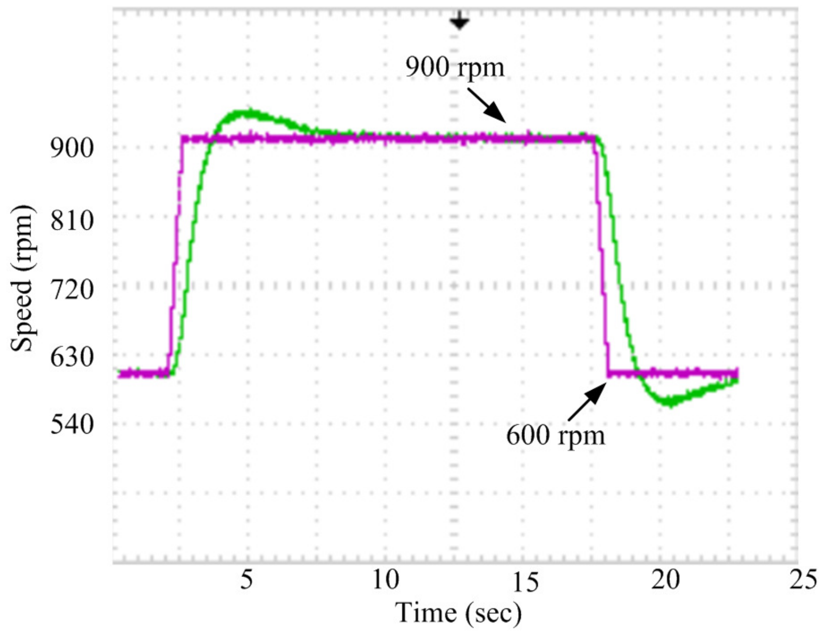

Figure 5.28: Experimental speed response of the five phase motor with a PI speed controller (Initial design: Kp = 0.069).

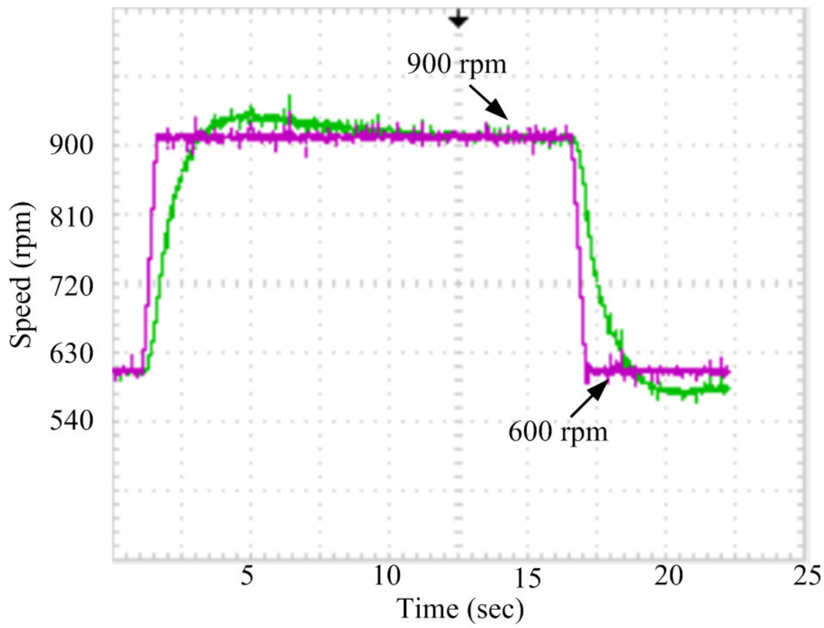

Figure 5.29: Experimental speed response of the five phase motor with a PI speed controller (Improved design: Kp = 0.13).

The performance of the proposed MRAC controller is compared with the conventional PI controller. In Figure 5.30, the speed response of the five-phase motor with the proposed MRAC controller is presented. It is shown that the motor speed follows the reference speed signal faster and there is no overshoot present. The dynamic performance is following the reference model accurately. Figure 5.31 shows two phase currents when there are no high order current harmonics injected and Figure 5.32 shows that when the 3rd order harmonic current is injected. The load condition is the same for both experiments.

High speed experiment in the flux weakening region has also been carried out. Figure 5.33 shows the speed response between 1500rpm and 1800rpm. It can be seen that the speed dynamic agrees with simulation result. Compared to low speed test, the speed dynamic performance is not changed even though the operating point has changed.

The capability to recover from load disturbance is also tested. A load change (0 Nm to 1.1 Nm) is applied on the motor with both the PI controller and the proposed model reference adaptive control. The speed responses are shown in Figure 5.34 and Figure 5.35. It can be seen from Figure 5.34 that with the conventional PI speed controller, motor speed drops much more than that in Figure 5.35, when the proposed MRAC is applied. Moreover, it is also clear that motor speed recovers faster with MRAC than PI speed controller.

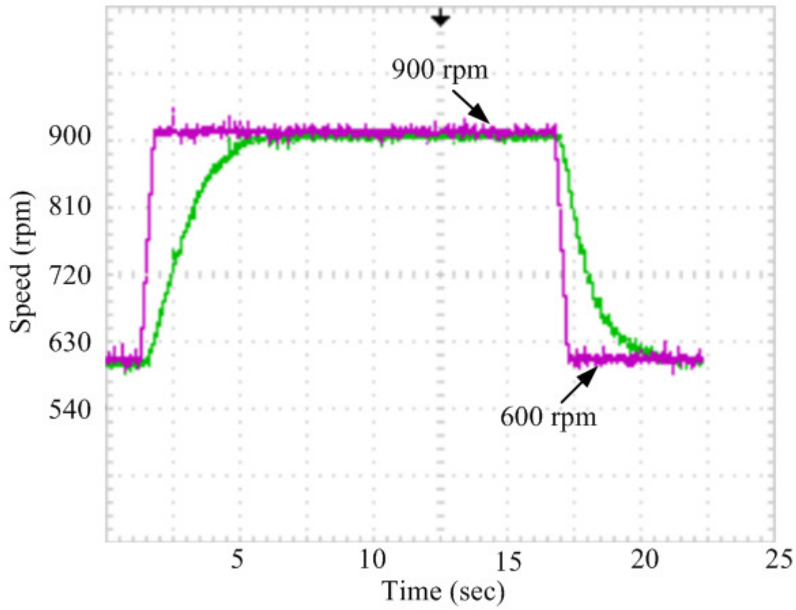

Figure 5.30: Experimental speed response of the five phase motor with the proposed MRAC motor drive.

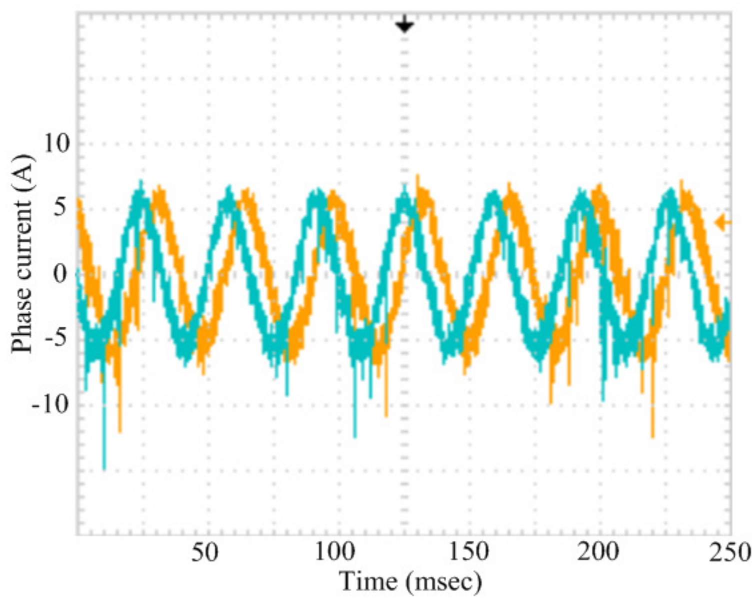

Figure 5.31: Experimental phase A and phase B currents without 3rd harmonic components injected (@ 900rpm).

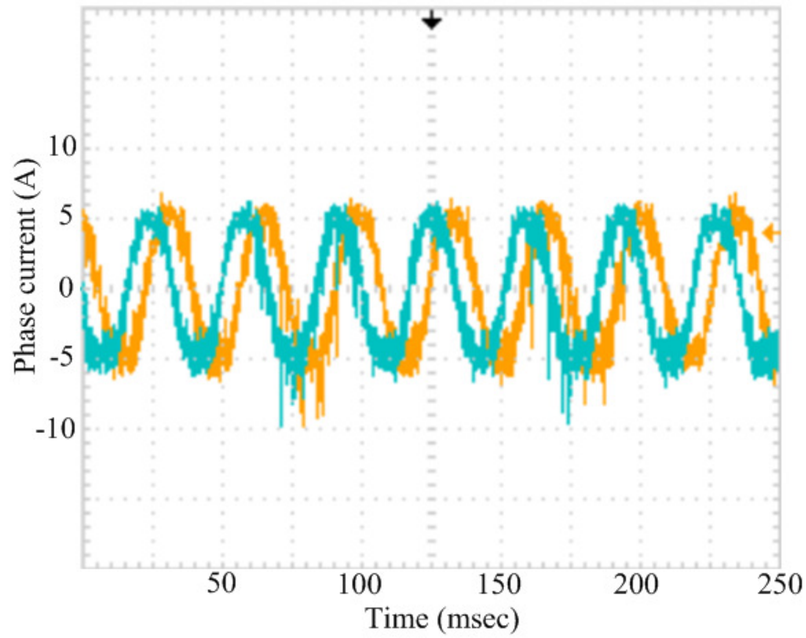

Figure 5.32: Experimental phase A and phase B currents with 3rd order harmonic components injected (@ 900rpm).

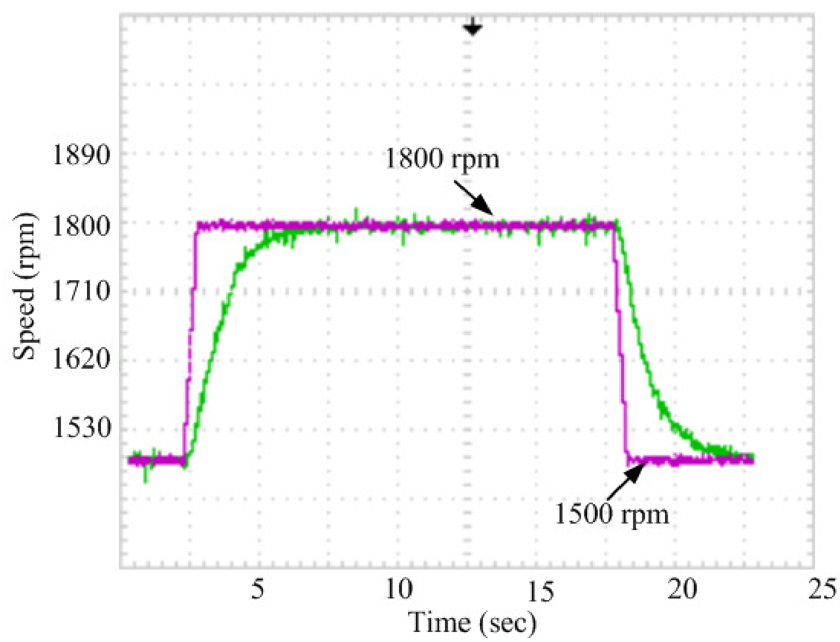

Figure 5.33: Experimental speed response of the five phase motor with the proposed MRAC motor drive at high speed (1500rpm-1800rpm).

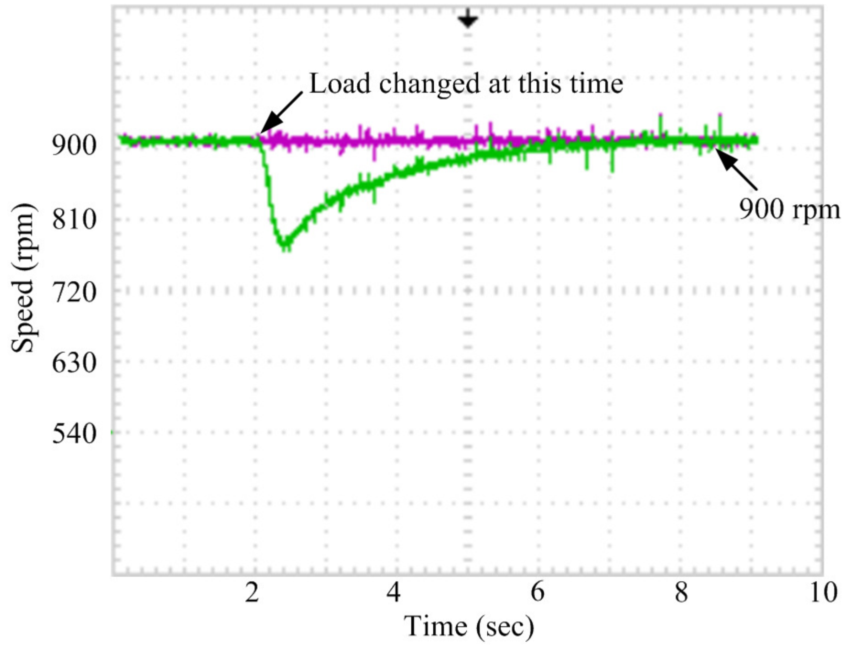

Figure 5.34: Experimental speed response of the five phase motor under sudden load change (with PI speed controller).

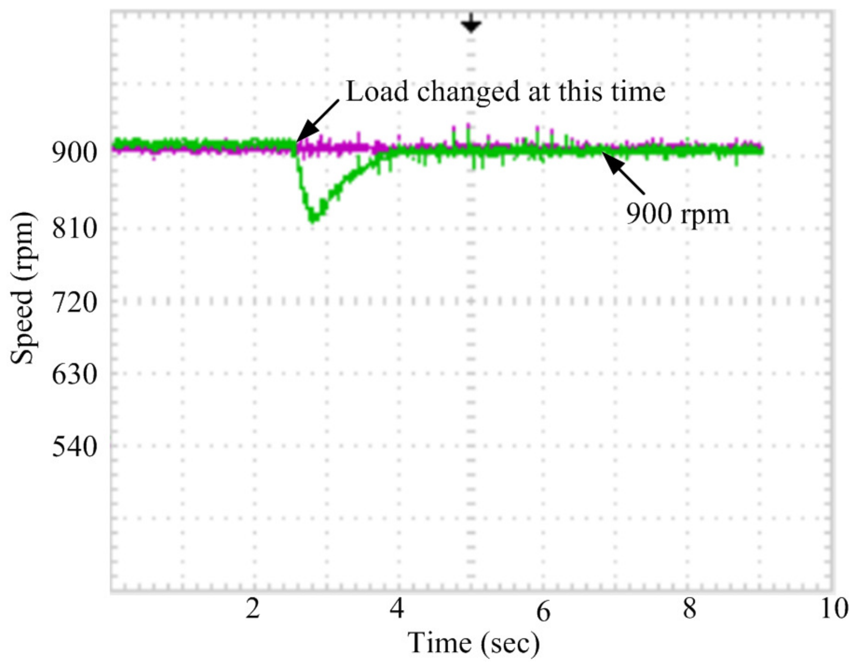

Figure 5.35: Experimental speed response of the five phase motor under sudden load change (with the proposed motor drive).

5.6.4 Application on the common stator SynRM and IPM machine

The proposed neural network based model reference adaptive control has been applied on the common stator SynRM and IPM machine. The first order linear reference model is selected to be with $a=k=4$. As a result, the closed loop bandwidth is 4 rad/s.

Figure 5.36 and Figure 5.37 provide the comparison results. The reference speed is switched from 600rpm to 900rpm. To conduct fair comparison between the MRAC controller and conventional PI regulators, a well-tuned PI controller is needed. Linearization method similar to that introduced in the previous section is applied to the prototype IPMSM, and the PI regulator parameters are designed to be with the same closed-loop bandwidth: 4 rad/s. Figure 5.36(a) shows the speed response with MRAC controller. Figure 5.36(b) records the speed response with PI regulator, whose parameters are tuned such that the closed-loop system bandwidth is also 4 rad/s. Figure 5.36(c) illustrates the speed response when the PI regulator parameters are manually tuned to suppress the overshoot. The tradeoff is increased settling time. It can be concluded that the motor speed follows the reference speed signal fast and there is no overshoot present. Similar conclusion can be drawn for prototype SynRM from Figure 5.37.

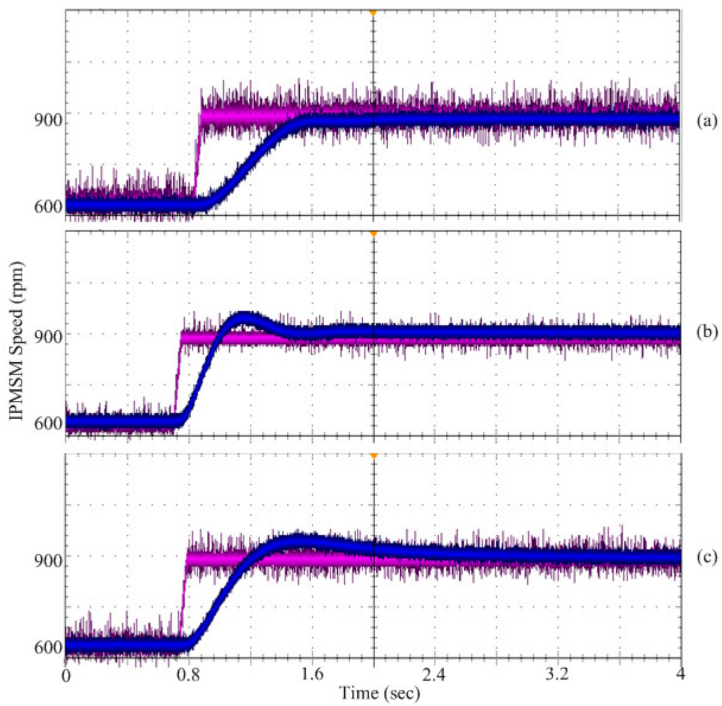

Figure 5.36: Speed responses of the IPMSM: (a) Neural network MRAC; (b) PI speed regulator, parameters tuned to get the same bandwidth as that in MRAC; (c) PI speed regulator, parameters manually tuned to minimize overshoot.

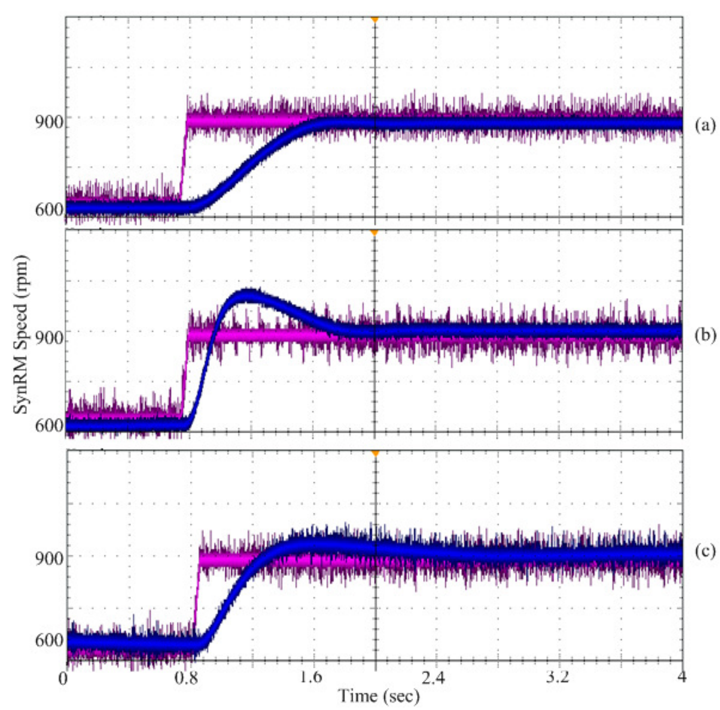

Figure 5.37: Speed responses of the SynRM: (a) Neural network MRAC; (b) PI speed regulator, parameters tuned to get the same bandwidth as that in MRAC; (c) PI speed regulator, parameters manually tuned to minimize overshoot.

5.7 Conclusion

A successful implementation of a novel neural network based model reference adaptive control for a five-phase permanent magnet motor has been presented in this chapter. MRAC structure is used to guarantee the dynamic performance of the motor drive system under parameter variations or load changes. The primary controller is designed as a neural network based controller which can adaptively change its parameters by online training. It is shown from theoretical analysis, computer simulations and laboratory experiments that the motor speed follows the reference speed signal well. Fair comparison has also been conducted between the proposed speed controller and the conventional fixed parameter PI controllers. It is shown that the proposed speed controller has faster and more accurate transient responses and almost no overshoots, which cannot be entirely eliminated in PI controllers.

The proposed permanent magnet motor drive has been introduced on a five-phase permanent magnet motor, but it can be easily implemented on a normal three-phase permanent magnet motor. Moreover, it can be extended to any vector controlled motors by simple modification. It has been successfully applied on the common stator SynRM and IPM machine.

6. SUMMARY AND FUTURE WORK

6.1 Summary of this research

The objective of this research arose from the increasing demand on electric motors in various industrial applications, such as all types of electric vehicles or electric hybrid vehicles. With the development of modern power electronics devices, synchronous type electric motors are more and more used in modern industrial applications as self start capability is not a major concern for electric machines any more. Among all synchronous type motors, synchronous reluctance machine and permanent magnet machines are both recognized as good candidates for future variable speed applications. Synchronous reluctance machine has a rather simple structure. There are only steel laminations in the rotor. It is a low cost and inherent fault tolerant solution for electric driving applications. The most significant advantage of permanent magnet synchronous motor is high power density. With the absence of permanent magnets in the rotor, the stator currents can be only focusing on generating torque instead of being wasted on generating necessary flux to transfer energy. One of the main objectives of this research is to design a common stator structure which can be used in either SynRMs or IPM motors. Both are synchronous type motors and they can easily share the same power electronics converter. In this way, the manufacturing cost and maintenance cost will be greatly reduced. SynRM can be used as a low cost solution for normal electric driving applications and IPM machines can be used in power density crucial circumstances or work as generators to satisfy the increasing demand for electrical power on board.

In chapter 2, various stator-rotor structures have been studied for SynRMs and IPM motors, with the aid of finite element analysis. It is found that 18-slot and 4-pole structure is a good design for both SynRM and IPM motor. As the operating mechanism of SynRM and IPM motor is different: The major source of magnetic flux of IPM motor is from rotor permanent magnets and the stator currents can be controlled not to carry such parts to generate magnetic flux. But in SynRM, all the magnetic flux is generated by stator currents. In the design stage, the conflict is SynRM needs much larger stator slot area to carry enough currents, but IPM motor needs larger stator teeth area to prevent it from going into deep saturation. Some optimization has been done to avoid the conflict.

In chapter 3, a torque pulsation minimization method of IPM motor in the design stage was proposed. There are mainly three sources of torque pulsations. One is the nonideal magnetic field distribution in the air gap, which will generate harmonic components in each phase flux linkage. This will induce a phase back-EMF with harmonics. When the IPM machine is supplied with sinusoidal currents, torque with significant pulsations is produced. Another source of torque pulsation arises from reluctance variation in the magnetic circuit when the rotor is rotating. Besides, cogging effect is also an origin of torque pulsation in IPM machines. There are mainly two methods of reducing torque ripple in IPM motors. One is from the motor design consideration. By designing IPM motors in a proper way, torque pulsation can be minimized. Finite element analysis is capable of calculating electromagnetic field accurately and it is widely used in designing proper electric machine structure. However, the compromise is that it usually costs much time in calculation. An optimization method to conduct finite element analysis was proposed in this chapter. This technique is based on orthogonal experimental design and the computer calculation time can be significantly reduced.

In chapter 4, another method of minimizing permanent magnet motor torque ripple was proposed, in motor control stage. All the sources of torque ripple in permanent magnet machines were analyzed first by finite element analysis. A current profiling technique was developed by calculating the optimum current profiles based on the torque equation in the *d*-*q* reference frame. Effects of not only the distorted permanent magnet flux linkages but the inductance variation and cogging torque can be included. The proposed technique was applied to a “V”-shape magnet IPM motor and the torque ripple was significantly reduced if the optimum currents were supplied.

In chapter 5, a novel neural network based model reference adaptive control for a five-phase permanent magnet motor was proposed. This technique is proposed based on the fact that with the growing needs for variable speed electric driving system, normal constant speed and constant load motor drive system may not suitable for some applications where the speed and load change frequently. The proposed technique uses

MRAC structure to guarantee the dynamic performance of the motor drive system under parameter variations or load changes. Theoretical analysis, computer simulations and laboratory experiments were provided to verify the proposed motor drive system. In addition, Comparison between the proposed motor drive system and PI controller based motor drive system was conducted to demonstrate the advantage of this technique.

To conclude, a common stator design of SynRM and IPM motor was conducted in this dissertation. The advantages include lower manufacturing and maintenance cost, shared power electronics devices and etc. Several efforts to improve the performance of permanent magnet synchronous motors were made. Torque ripple minimization methods were analyzed both in the motor design stage and motor control stage. A novel motor drive system was proposed suitable for future variable speed high load turbulence applications, such as electric vehicle drive system.

6.2 Future work

In this dissertation, a motor structure optimization method based on orthogonal experimental design has been introduced. An IPM motor with straight type magnet in the rotor was taken as an example to demonstrate this optimal design method. Optimization results have shown that this optimal design method is capable of minimizing torque pulsation in the motor design stage. The optimized motor has a relatively simple structure: rotor with straight-type magnets. Usually, optimized rotor with V-shape magnets has better performance, but the rotor structure will become more complex. With more geometric parameters, rotor with V-shape magnets will be analyzed and optimized using the proposed orthogonal experimental design method.

The current profiling technique introduced in this dissertation managed to reduce torque pulsation in a significant degree. From Figure 4.12, it is clear that there is still torque pulsation existing even when the optimum currents are supplied. One of the reasons is this current profiling technique is derived based on the *d-q* reference frame transformation, which neglects magnetic flux saturation, *d-q* axis inductance saturation and etc. More accurate models taking these effects into account can be used to replace the simple *d-q* reference frame model to develop an improved current profiling technique. Nonlinearity of magnetic field such as saturation and cross effects of d-q axis inductances has to be modeled first.

REFERENCES

[1] U.S. Department of Energy. (December, 2002). United States Industrial Electric Motor Systems Market Opportunities Assessment [Online]. Available: http://www.energy.gov/sites/prod/files/2014/04/f15/mtrmkt.pdf (Date Last Accessed, April 10, 2016).

[2] U.S. Environmental Protection Agency. (April 12, 2013). Inventory of U.S. Greenhouse Gas Emissions and Sinks: 1990-2011 [Online]. Available: http://www3.epa.gov/climatechange/Downloads/ghgemissions/US-GHG-Inventory-2013-Main-Text.pdf (Date Last Accessed, April 10, 2016).

[3] U.S. Environmental Protection Agency. (April 15, 2014). Inventory of U.S. Greenhouse Gas Emissions and Sinks: 1990-2012 [Online]. Available: http://www3.epa.gov/climatechange/Downloads/ghgemissions/US-GHG-Inventory-2014-Main-Text.pdf (Date Last Accessed, April 10, 2016).

[4] S. A. Nasar, I. Boldea and L. E. Unnewehr, *Permanent Magnet, Reluctance, and Self-Synchronous Motors*. Boca Raton, FL: CRC Press, 1993.

[5] P. P. Acarnley, J. F. Watson, "Review of position-sensorless operation of brushless permanent-magnet machines," *IEEE Trans. Ind. Electron.,* vol. 53, no. 2, pp. 352-362, Apr. 2006.

[6] I. Egana *et al.*, "Flat magnets in surface-mounted permanent magnet machines: Influence and design," *Int. Symp. Power Electronics, Electrical Drives, Automation and Motion*, pp. 697-701, Jun. 2008.

[7] K. Boughrara *et al.*, "Analytical model of slotted air-gap surface mounted permanent-magnet synchronous motor with magnet bars magnetized in the shifting direction," *IEEE Trans. Magn.*, vol. 45, no. 2, pp. 747-758, Feb. 2009.

[8] M. F. Hsieh, Y. C. Hsu, D. G. Dorrell, "Design of large power Surface-Mounted Permanent-Magnet Motors using post-assembly magnetization," *33rd Annu. Conf. IEEE Industrial Electronics Society*, pp. 204-209, Nov. 2007.

[9] Y. Kano, T. Kosaka, N. Matsui, "Simple nonlinear magnetic analysis for permanent-magnet motors," *IEEE Trans. Ind. Appl.*, vol. 41, no. 5, pp. 1205-1214, Sept.-Oct. 2005.

[10] J. Wang, X. Yuan and K. Atallah, "Design optimization of a Surface-Mounted Permanent-Magnet motor with concentrated windings for electric vehicle applications," *IEEE Trans. Veh. Technol.*, vol. 62, no. 3, pp. 1053-1064, Mar. 2013.

[11] D. Wu and Z. Q. Zhu, "Design tradeoff between cogging torque and torque ripple in fractional slot Surface-Mounted Permanent Magnet machines," *IEEE Trans. Magn.*, vol. 51, no. 11, pp. 1-4, Nov. 2015.

[12] J. M. Kim *et al.*, "Design and analysis of Surface-Mounted-Type variable flux permanent magnet motor for wide-speed range applications," *IEEE Trans. Magn.*, vol. 51, no. 11, pp. 1-4, Nov. 2015.

[13] J. S. Hsu *et al.*, "Effect of side permanent magnets for reluctance interior permanent magnet machines," *IEEE Power Electronics Specialists Conf.*, pp. 2267-2272, Jun. 2007.

[14] K. C Kim *et al.*, "Multiobjective optimal design for interior permanent magnet synchronous motor," *IEEE Trans. Magn.*, vol. 45, no. 3, pp. 1780-1783, Mar. 2009.

[15] F. Hetemi, G. Dajaku and D. Gerling, "Influence of magnet thickness and magnet orientation on the performance of IPMSM," *19th Int. Conf. Electrical Machines,* pp. 1-4, Sept. 2010.

[16] S. Y. Lee *et al.*, "Development of multi-layer interior permanent magnet synchronous machine for vehicle," *Int. Conf. Electrical Machines and Systems*, pp. 935-938, 8-11 Oct. 2007.

[17] Q. Chen *et al.*, "Design and comparison of two Fault-Tolerant Interior-Permanent-Magnet motors," *IEEE Trans. Ind. Electron.*, vol. 61, no. 12, pp. 6615-6623, Dec. 2014.

[18] W. Zhao *et al.*, "Optimal design of a novel V-Type interior permanent magnet motor with assisted barriers for the improvement of torque characteristics," *IEEE Trans. Magn.*, vol. 50, no. 11, pp. 1-4, Nov. 2014.

[19] D. K. Lim *et al.*, "Optimal design of an interior permanent magnet synchronous motor by using a new surrogate-assisted multi-objective optimization," *IEEE Trans. Magn.*, vol. 51, no. 11, pp. 1-4, Nov. 2015.

[20] W. L. Soong and N. Ertugrul, "Field-weakening performance of interior permanent magnet motors," *IEEE Industry Applications Conf.*, pp. 416-423, 2000.

[21] B. Stumberger *et al.*, "Analysis of interior permanent magnet synchronous motor designed for flux weakening operation," *IEEE Trans. Magn.*, vol. 37, no. 5, pp. 3644-3647, Sept. 2001.

[22] A. Pouramin and S. M. Madani, "New interior PM rotor design with high flux-weakening capability," *IEEE Int. Electric Machines and Drives Conf.*, pp. 958-963, May 2009.

[23] S. Duan, L. Zhou and J. Wang, "Flux weakening mechanism of interior permanent magnet synchronous machines with segmented permanent magnets," *IEEE Trans. Appl. Supercond.*, vol. 24, no. 3, pp. 1-5, Jun. 2014.

[24] R. E. Hanitsch, M. S. Widyan and R. Grune, "Cogging torque reduction of a novel low-speed high-energy permanent-magnet electrical machine," *Int. Symp. Power Electronics, Electrical Drives, Automation and Motion,* pp. 97-102, May 2006.

[25] H. Li *et al.*, "Analytical calculation of inductance parameter of tangentially magnetized PM motor based on basic air-gap magnetic field," *2nd Int. Conf. Artificial Intelligence, Management Science and Electronic Commerce*, pp. 3776-3781, Aug. 2011.

[26] P. Zheng *et al.*, "Research on the magnetization of a tangentially magnetized brushless DC motor," *Dig. IEEE Int. Magnetics Conf.,* pp. 1951-1952, Apr. 2005.

[27] M. S. Widyan and R. E. Hanitsch, "Directly driven rare-earth permanent-magnet electrical-machine prototype for wind energy applications," *42nd Int. Universities Power Engineering Conf.,* pp. 786-790, Sept. 2007.

[28] P. Zhang *et al.*, "Establishing the relative merits of interior and Spoke-Type Permanent-Magnet machines with ferrite or NdFeB through systematic design optimization," *IEEE Trans. Ind. Appl.*, vol. 51, no. 4, pp. 2940-2948, Jul.-Aug. 2015.

[29] S. M. Hosseini, M. Agha-Mirsalim and M. Mirzaei, "Design, prototyping, and analysis of a low cost Axial-Flux coreless Permanent-Magnet generator," *IEEE Trans. Magn.,* vol. 44, no. 1, pp. 75-80, Jan. 2008.

[30] P. R. Upadhyay and K. R. Rajagopal, "FE analysis and Computer-Aided design of a sandwiched Axial-Flux permanent magnet brushless DC motor," *IEEE Trans. Magn.*, vol. 42, no. 10, pp. 3401-3403, Oct. 2006.

[31] H. Jussila *et al.*, "Concentrated winding axial flux permanent magnet motor for industrial use," *19th Int. Conf. Electrical Machines,* pp. 1-5, Sept. 2010.

[32] S. Mohammadi *et al.*, "Analytical modeling and analysis of Axial-Flux interior Permanent-Magnet couplers," *IEEE Trans. Ind. Electron.*, vol. 61, no. 11, pp. 5940-5947, Nov. 2014.

[33] Y. P. Yang, Y. P. Luh and C. H. Cheung, "Design and control of axial-flux brushless DC wheel motors for electric Vehicles-part I: multiobjective optimal design and analysis," *IEEE Trans. Magn.*, vol. 40, no. 4, pp. 1873-1882, Jul. 2004.

[34] Y. P. Yang, J. Y. Liang and X. Y. Xing, "Design and application of axial-flux permanent magnet wheel motors for an electric vehicle," *IEEE AFRICON Conf.*, pp. 1-5, Sept. 2009.

[35] K. M. Rahman *et al.*, "Application of Direct-Drive wheel motor for fuel cell electric and hybrid electric vehicle propulsion system," *IEEE Trans. Ind. Appl.*, vol. 42, no. 5, pp. 1185-1192, Sept.-Oct. 2006.

[36] M. Polikarpova *et al*., "Hybrid cooling method of Axial-Flux Permanent-Magnet machines for vehicle applications," *IEEE Trans. Ind. Electron.*, vol. 62, no. 12, pp. 7382-7390, Dec. 2015.

[37] O. Maloberti *et al*., "3-D–2-D dynamic magnetic modeling of an axial flux permanent magnet motor with soft magnetic composites for hybrid electric vehicles," *IEEE Trans. Magn.*, vol. 50, no. 6, pp. 1-11, Jun. 2014.

[38] Q. F. Lu and Y. Y. Ye; "Design and analysis of large capacity Line-Start Permanent-Magnet motor," *IEEE Trans. Magn.,* vol. 44, no. 11, pp. 4417-4420, Nov. 2008.

[39] P. W. Huang *et al.*, "Investigation of line start permanent magnet synchronous motors with interior-magnet rotors and surface-magnet rotors," *Int. Conf. Electrical Machines and System*, pp. 2888-2893, Oct. 2008.

[40] J. Li, J. Song and Y. Cho, "High performance line start permanent magnet synchronous motor for pumping system," *IEEE Int. Symp. Industrial Electronics*, pp. 1308-1313, Jul. 2010.

[41] S. Shamlou and M. Mirsalim, “Design, optimisation, analysis and experimental verification of a new line-start permanent magnet synchronous shaded-pole motor,” *IET Electric Power Applications*, vol. 7, no. 1, pp. 16-26, Jan. 2013.

[42] T. J. E. Miller, M. I. McGilp and M. Olaru, “Finite elements applied to synchronous and switched reluctance motors,” *IEE Seminar on Current Trends in the Use of Finite Elements (FE) in Electromechanical Design and Analysis*, pp. 3/1-3/4, Mar. 2000.

[43] B. Ahn *et al.*, “A study on the optimal barrier design for high efficiency of LSPM,” *Int. Conf. Electrical Machines and Systems*, pp. 3427-3429, Oct. 2008.

[44] E. Schmidt, W. Brandl and C. Grabner, “Design improvement of synchronous reluctance machines with internal rotor flux barriers for high-speed drives,” *IEEE 33rd Annu. Power Electronics Specialists Conf.,* pp. 1949-1954, Jun. 2002.

[45] A. Vagati *et al.*, “Design refinement of synchronous reluctance motors through finite-element analysis,” *IEEE Trans. Ind. Appl.*, vol. 36, no. 4, pp. 1094-1102, Jul.-Aug. 2000.

[46] X. B. Bomela and M. J. Kamper, “Effect of machine design on performance of reluctance synchronous machine,” *IEEE Industry Applications Conf.,* vol. 1, pp. 515-522, Oct. 2000.

[47] E. Howard, M. J. Kamper and S. Gerber, “Asymmetric flux barrier and skew design optimization of reluctance synchronous machines,” *IEEE Trans. Ind. Appl.*, vol. 51, no. 5, pp. 3751-3760, Sept.-Oct. 2015.

[48] F. N. Isaac, A. A. Arkadan and A. El-Antably, “Characterization of axially laminated anisotropic-rotor synchronous reluctance motors,” *IEEE Trans. Energy Convers.*, vol. 14, no. 3, pp.506-511, Sept. 1999.

[49] I. Boldea, Z. X. Fu and S. A. Nasar, “Performance evaluation of axially-laminated anisotropic (ALA) rotor reluctance synchronous motors,” *IEEE Trans. Ind. Appl.*, vol. 30, no. 4, pp.977-985, Jul.-Aug. 1994.

[50] B. J. Chalmers and L. Musaba, “Design and field-weakening performance of a synchronous reluctance motor with axially-laminated rotor,” *IEEE Industry Applications Conf.*, pp. 271-278, Oct. 1997.

[51] A. Vagati *et al.*, "Design of low-torque-ripple synchronous reluctance motors," *IEEE Trans. Ind. Appl.*, vol. 34, no. 4, pp.758-765, Jul.-Aug. 1998.

[52] L. Xu *et al.*, "Vector control of a synchronous reluctance motor including saturation and iron loss," *IEEE Trans. Ind. Appl.*, vol. 27, no. 5, pp.977-985, Sept.-Oct. 1991.

[53] E. Daryabeigi *et al.*, "Online MTPA control approach for synchronous reluctance motor drives based on emotional controller," *IEEE Trans. Power Electron.*, vol. 30, no. 4, pp. 2157-2166, Apr. 2015.

[54] I. Boldea, Z. X. Fu, and S. A Nasar, "Digital simulation of a vector current controlled axially-laminated anisotropic rotors synchronous motor servo-drive," *Elec. Machi. Pow. Syst.*, pp. 415-424, Jul.-Aug. 1991.

[55] M. Hortman and D. G. Taylor, "Nonlinear observer-based speed control of a synchronous reluctance motor," *29th Annu. Conf. IEEE Industrial Electronics Society*, vol. 2, pp. 1038-1043, Nov. 2003.

[56] S. Zhang, L. Norum and R. Nilssen, "Variable voltage variable frequency control of tubular linear permanent magnet synchronous machine for drilling applications," *19th Int. Conf. Electrical Machines*, pp. 1-5, Sept. 2010.

[57] R. Molavi, K. Shojaee and D. A. Khaburi, "Optimal vector control of permanent magnet synchronous motor," *IEEE Int. Power and Energy Conf.,* pp. 249-253, Dec. 2008.

[58] Y. Liu, S. Liu and H. Wang, "DSP control implement of Permanent Magnet Synchronous AC servo motor based on vector control," *Int. Conf. Mechatronics and Automation,* pp. 866-870, Aug. 2009.

[59] J. Kim, S. Kang and S. Sul, "Vector control of interior permanent magnet synchronous motor without a shaft sensor," *12th Annu. Applied Power Electronics Conf. and Expo.,* pp. 743-748, Feb. 1997.

[60] P. Brandstetter, T. Krecek and P. Korbel, "Non-model based sensorless vector control of permanent magnet synchronous motor," *IEEE Int. Symp. Industrial Electronics,* pp. 618-623, Jun.-Jul. 2008.

[61] M. Sreejeth, M. Singh and P. Kumar, “Particle swarm optimisation in efficiency improvement of vector controlled surface mounted permanent magnet synchronous motor drive,” *IET Power Electronics*, vol. 8, no. 5, pp. 760-769, Apr. 2015.

[62] C. French and P. Acarnley, “Direct torque control of permanent magnet drives,” *IEEE Trans. Ind. Appl.*, vol. 32, no. 5, pp.1080-1088, Sept.-Oct. 1996.

[63] L. Zhong *et al.*, “Analysis of direct torque control in permanent magnet synchronous motor drives,” *IEEE Trans. Power Electron.*, vol. 12, no. 3, pp. 528-536, May 1997.

[64] J. Cui, Y. Fu and X. Yang, “Improved direct torque control of permanent magnet synchronous motor,” *IEEE Conf. Industrial Electronics and Applications,* pp. 2363-2366, May 2009.

[65] Y. Inoue, S. Morimoto and M. Sanada, “Examination and Linearization of Torque Control System for Direct Torque Controlled IPMSM,” *IEEE Trans. Ind. Appl.*, vol. 46, no. 1, pp. 159-166, Jan.-Feb. 2010.

[66] Y. Yan *et al.*, “Direct torque control of matrix converter-fed permanent magnet synchronous motor drives based on master and slave vectors,” *IET Power Electronics*, vol. 8, no. 2, pp. 288-296, Feb. 2015.

[67] Y. Ren, Z. Q. Zhu and J. Liu, “Direct torque control of Permanent-Magnet Synchronous Machine drives with a simple duty ratio regulator,” *IEEE Trans. Ind. Electron.*, vol. 61, no. 10, pp. 5249-5258, Oct. 2014.

[68] T. C. Chen and T. T. Sheu, “Model reference neural network controller for induction motor speed control,” *IEEE Trans. Energy Convers.*, vol. 17, no. 2, pp. 157-163, Jun. 2002.

[69] M. A. S. K. Khan and M. A. Rahman, “A novel neuro-wavelet-based self-tuned wavelet controller for IPM motor drives,” *IEEE Trans. Ind. Appl.*, vol. 46, no. 3, pp. 1194-1203, May-Jun. 2010.

[70] M. N. Uddin and H. Wen, “Development of a self-tuned neuro-fuzzy controller for induction motor drives,” *IEEE Trans. Ind. Appl.*, vol. 43, no. 4, pp. 1108-1116, Jul.-Aug. 2007.

[71] S. M. Gadoue, D. Giaouris and J. W. Finch, "MRAS sensorless vector control of an induction motor using new sliding-mode and fuzzy-logic adaptation mechanisms," *IEEE Trans. Energy Convers.*, vol. 25, no. 2, pp. 394-402, Jun. 2010.

[72] J. Yu *et al.*, "Neural Network-Based adaptive dynamic surface control for Permanent Magnet Synchronous Motors," *IEEE Trans. Neural Netw.*, vol. 26, no. 3, pp. 640-645, Mar. 2015.

[73] F. J. Lin *et al.*, "Intelligent position control of permanent magnet synchronous motor using recurrent fuzzy neural cerebellar model articulation network," *IET Electric Power Applications*, vol. 9, no. 3, pp. 248-264, Mar. 2015.

[74] K. J. Binns and D. W. Shimmin, "Relationship between rated torque and size of permanent magnet machines," *IEE Proc. Electric Power Applications*, vol. 143, no. 6, pp. 417-422, Nov. 1996.

[75] Y. Pang, Z.Q. Zhu and D. Howe, "Optimal split ratio for permanent magnet brushless motors," *6th Int. Conf. Electrical Machines and Systems,* pp. 128-131, Nov. 2003.

[76] C. Chen *et al.*, "Maximum torque control of synchronous reluctance motor speed drive based on the Lyapunov function stability theorem," *IEEE Conf. Industrial Electronics and Applications*, pp. 2103-2108, May 2007.

[77] S. Dwari, L. Parsa and T. A. Lipo, "Optimum control of a Five-phase integrated modular permanent magnet motor under normal and Open-Circuit fault conditions," *IEEE. Power Electronics Specialists Conf.,* pp. 1639-1644, Jun. 2007.

[78] J. D. Ede *et al.*, "Modular Fault-tolerant permanent magnet brushless machines," *Proc. Power Electronics, Machines, and Drives,* pp. 415-420, Jun. 2002.

[79] G. H. Lee *et al.*, "Torque ripple reduction of interior permanent magnet synchronous motor using harmonic injected current," *IEEE. Trans. Magn.,* vol. 44, no. 6, pp. 1582-1585, May 2008.

[80] L. Parsa and L. Hao, "Interior permanent magnet motors with reduced torque pulsation," *IEEE Trans. Ind. Electron.,* vol. 55, no. 2, pp. 602-609, Jan. 2008.

[81] J. Wang *et al.*, "Comparative study of 3-phase permanent magnet brushless machines with concentrated, distributed and modular windings," *Int. Conf. Power Electronics, Machines and Drives*, pp. 489-493, Mar. 2006.

[82] L. Alberti, M. Barcaro and N. Bianchi, “Design of a Low-Torque-Ripple Fractional-Slot interior Permanent-Magnet motor,” *IEEE Trans. Ind. Appl.*, vol. 50, no. 3, pp. 1801-1808, May-Jun. 2014.

[83] A. Kioumarsi, M. Moallem and B. Fahimi, “Mitigation of torque ripple in interior permanent magnet motors by optimal shape design,” *IEEE Trans. Magn.*, vol. 42, no. 11, pp. 3706-3711, Nov. 2006.

[84] Z. Q. Zhu *et al.*, “Reduction of cogging torque in interior-magnet brushless machines,” *IEEE Trans. Magn.,* vol. 39, no. 5, pp. 3238-3240, Sept. 2003.

[85] P. Niazi *et al.*, “A low-cost and efficient permanent-magnet-assisted synchronous reluctance motor drive,” *IEEE Trans. Ind. Appl.*, vol. 43, no. 2, pp. 542-550, Mar.-Apr. 2007.

[86] N. Bianchi and A. Canova, “FEM analysis and optimisation design of an IPM synchronous motor,” *Int. Conf. Power Electronics, Machines and Drives,* pp. 49-54, Jun. 2002.

[87] D. J. Sim *et al.*, “Efficiency optimization of interior permanent magnet synchronous motor using genetic algorithms,” *IEEE Trans. Magn.*, vol. 33, no. 2, pp. 1880-1883, Mar. 1997.

[88] A. Consoil, and G. Renna, “Interior type permanent magnet synchronous motor analysis by equivalent circuits,” *IEEE Trans. Energy Convers.,* vol. 4, no. 4, pp. 681-689, Dec. 1989.

[89] Sneyers *et al.*, “Field weakening in buried permanent magnet ac motor drives,” *IEEE Trans. Ind. Appl.,* vol. 21, no. 2, pp. 398-407, Mar. 1985.

[90] T. Li *et al.*, “Reduction of cogging torque in permanent magnet motors,” *IEEE Trans. Magn.,* vol. 24, no. 6, pp. 2901-2903, Nov. 1988.

[91] L. Guo and L. Parsa, “Torque ripple reduction of the modular Interior Permanent Magnet machines using optimum current profiling technique,” *IEEE Int. Electric Machines and Drives Conf.,* pp. 1094-1099, May 2009.

[92] L. Guo and L. Parsa, “Geometry optimization of IPM machines using orthogonal experimental design method and artificial neural network,” *J. of Electromagn. Waves and Appl.*, vol. 25, pp. 901-912, Apr. 2012.

[93] L. Parsa and H.A. Toliyat, “Sensorless direct torque control of five-phase interior permanent-magnet motor drives,” *IEEE Trans. Ind. Appl.*, vol. 43, no. 4, pp. 952-959, Jul.-Aug. 2007.

[94] L. Parsa and H.A. Toliyat, “Five-phase permanent-magnet motor drives,” *IEEE Trans. Ind. Appl.*, vol. 41, no. 1, pp. 30-37, Jan.-Feb. 2005.

[95] T. Gopalarathnam *et al.*, “Development of low cost multi-phase brushless permanent magnet (BPM) motors with unipolar current excitations,” *IEEE Industry Applications Society Annu. Meeting,* pp. 173-179, Oct. 1999.

[96] C. C. Chan *et al.*, “A novel high power density permanent magnet variable-speed motor,” *IEEE Trans. Energy Convers.*, vol. 8, no. 2, pp. 297-303, Jun. 1993.

[97] L. Parsa and H.A. Toliyat, “Fault tolerant interior permanent magnet motors for hybrid electric vehicle applications,” *IEEE Trans. Veh. Technol.*, vol. 56, no. 4, pp. 1546-1552, Jul. 2007.

[98] S. Dwari and L. Parsa, “An optimal control technique for multiphase PM machines under open-circuit faults,” *IEEE Trans. Ind. Electron.*, vol. 55, no. 5, pp. 1988-1995, May 2008.

[99] L. Parsa, K. Namhun and H.A. Toliyat, “Field weakening operation of a high torque density five phase permanent magnet motor drive,” *Int. Conf. Electric Machines and Drives*, pp. 1507-1512, May 2005.

[100] M. Tursini, F. Parasiliti and D. Zhang, “Real-time gain tuning of PI controllers for high-performance PMSM drives,” *IEEE Trans. Ind. Appl.*, vol. 38, no. 4, pp. 1018-1026, Jul.-Aug. 2002.

[101] M. N. Uddin, M.A. Abido and M.A. Rahman, “Development and implementation of a hybrid intelligent controller for interior permanent-magnet synchronous motor drives,” *IEEE Trans. Ind. Appl.*, vol. 40, no. 1, pp. 68-76, Jan.-Feb. 2004.

[102] F. J. Lin, R. J. Wai and H.P. Chen, “A PM synchronous servo motor drive with an on-line trained fuzzy neural network controller,” *IEEE Trans. Energy Convers.*, vol. 13, no. 4, pp. 319-325, Dec. 1998.

[103] Q. Huang, Z. Huang and H. Zhou, “Nonlinear optimal and robust speed control for a light-weighted all-electric vehicle,” *IET Control Theory & Applications*, vol. 3, no. 4, pp. 437-444, Apr. 2009.

[104] T. Orlowska-Kowalska, M. Dybkowski and K. Szabat, "Adaptive sliding-mode neuro-fuzzy control of the two-mass induction motor drive without mechanical sensors," *IEEE Trans. Ind. Electron.*, vol. 57, no. 2, pp. 553-564, Feb. 2010.

[105] M. Ghanes and G. Zheng, "On sensorless induction motor drives: Sliding-mode observer and output feedback controller," *IEEE Trans. Ind. Electron.*, vol. 56, no. 9, pp. 3404-3413, Sept. 2009.

[106] M. Defoort *et al.*, "A third-order sliding-mode controller for a stepper motor," *IEEE Trans. Ind. Electron.*, vol. 56, no. 9, pp. 3337-3346, Sept. 2009.

[107] M. Elbuluk, T. Liu and I. Husain, "Neural-network-based model reference adaptive systems for high-performance motor drives and motor controls," *IEEE Trans. Ind. Appl.*, vol. 38, no. 3, pp. 879-886, May-Jun. 2002.

[108] M. Rashed, P. F. A. MacConnell and A. F. Stronach, "Nonlinear adaptive state-feedback speed control of a voltage-fed induction motor with varying parameters," *IEEE Trans. Ind. Appl.*, vol. 42, no. 3, pp. 723-732, May-Jun. 2006.

[109] S. Maiti *et al.*, "Model reference adaptive controller-based rotor resistance and speed estimation techniques for vector controlled induction motor drive utilizing reactive power," *IEEE Trans. Ind. Electron.*, vol. 55, no. 2, pp. 594-601, Feb. 2008.

[110] T. Orlowska-Kowalska and M. Dybkowski, "Stator-current-based MRAS estimator for a wide range speed-sensorless induction-motor drive," *IEEE Trans. Ind. Electron.*, vol. 57, no. 4, pp. 1296-1308, Apr. 2010.

[111] R. Pea *et al.*, "Sensorless control of doubly-fed induction generators using a rotor-current-based MRAS observer," *IEEE Trans. Ind. Electron.*, vol. 55, no. 1, pp. 330-339, Jan. 2008.

[112] R. Cardenas *et al.*, "MRAS observer for sensorless control of standalone doubly fed induction generators," *IEEE Trans. Energy Convers.*, vol. 20, no. 4, pp. 710-718, Dec. 2005.

[113] M. Cirrincione and M. Pucci, "An MRAS-based sensorless high-performance induction motor drive with a predictive adaptive model," *IEEE Trans. Ind. Electron.*, vol. 52, no. 2, pp. 532-551, Apr. 2005.

[114] M. Comanescu and L. Xu, "Sliding-mode MRAS speed estimators for sensorless vector control of induction Machine," *IEEE Trans. Ind. Electron.*, vol. 53, no. 1, pp. 146-153, Feb. 2006.

[115] A. F. A. Furtunato *et al.*, "A robust control for induction motor using a variable structure model reference adaptive control (VS-MRAC)," *IEEE Int. Power Electronics Congr.*, pp. 61-69, Oct. 1998.

[116] M. Koksal *et al.*, "Position control of a permanent magnet DC motor by model reference adaptive control," *Int. Symp. Industrial Electronics*, pp. 112-117, Jun. 2007.

[117] P. Crnosija *et al.*, "Application of model reference adaptive control with signal adaptation to PM brushless DC motor drives," *IEEE Int. Symp. Industrial Electronics*, pp. 689-694, Jul. 2002.

[118] M. Nour *et al.*, "Hybrid model reference adaptive speed control for vector controlled permanent magnet synchronous motor drive," *IEEE Int. Conf. Power Electronics and Drives Systems*, pp. 618-623, Nov. 2005.

[119] E. Cerruto *et al.*, "A robust adaptive controller for PM motor drives in robotic applications," *IEEE Trans. Power Electron.*, vol. 10, no. 1, pp. 62-71, Jan. 1995.

[120] Petros A. Ioannou and Jing Sun, *Robust Adaptive Control*. Upper Saddle River, NJ: Prentice Hall PTR, 1995.

[121] Y. A.-R. I. Mohamed and T. K. Lee, "Adaptive self-tuning MTPA vector controller for IPMSM drive system," *IEEE Trans. Energy Convers.*, vol. 21, no. 3, pp. 634-644, Sept. 2006.

[122] M. N. Uddin *et al.*, "Performance of interior permanent magnet motor drive over wide speed range," *IEEE Trans. Energy Convers.*, vol. 17, no. 1, pp. 79-84, Mar. 2002.

[123] H. D. Patino and D. Liu, "Neural network-based model reference adaptive control system," *IEEE Trans. Syst. Man Cybern. B, Cybern.*, vol. 30, no. 1, pp. 198-204, Feb. 2000.

[124] L. Guo and L. Parsa, "Effects of magnet shape on torque characteristics of Interior Permanent Magnet machines," *IEEE Electric Ship Technologies Symp., 2009. ESTS 2009*, pp. 93-97, Apr. 2009.

[125] L. Parsa, "Performance improvement of permanent magnet AC motors," Ph.D. dissertation, Dept. Elect. Eng., Texas A&M Univ., College Station, TX, 2005.

[126] L. Guo and L. Parsa, "Model reference adaptive control of five-phase IPM motors based on neural network," *IEEE Trans. Ind. Electron.,* vol. 59, no. 3, pp. 1500-1508, Aug. 2012.